Resource utilization of carbon dioxide and nitrate to produce value-added organonitrogen compounds through an electrochemical approach

Kailun Yu [a], Hui Wang [a,*], Wenchao Yu [a], Shunlin Li [a], Xinyu Zhang [a], Zhaoyong Bian [b,**]

[a] College of Environmental Science and Engineering, Beijing Forestry University, Beijing 100083, PR China
[b] College of Water Sciences, Beijing Normal University, Beijing 100875, PR China

ARTICLE INFO

ABSTRACT

Excess CO_2 and NO_3^- released by human industrial activities have contributed to the deterioration of the global environment. Simultaneous activation and reduction of CO_2 and NO_3^- to produce high-value chemical products is not only effective in solving environmental problems but can also recycle waste pollutants and is essential for the strategic realization of carbon neutrality. Compared with conventional artificial nitrogen and carbon fixation processes, electrochemical C-N coupling of CO_2 and NO_3^- under ambient conditions is an emerging approach. However, the understanding of C-N coupling is still in its infancy, as CO_2 and NO_3^- are first reduced individually to produce different C and N intermediates, which are further coupled to form different types of organic nitrogen compounds through a series of PCET processes. However, this process is often accompanied by the generation of many byproducts. To improve the selectivity of the target products, the design and modulation of catalyst active sites are important. In this paper, a detailed review of the different mechanisms of electrocatalytic coreduction of CO_2 and NO_3^- is presented. From the perspective of controlling competitive reactions, the elements that can achieve C-N coupling in electrocatalysis are divided into p-block elements and d-block elements. The regulatory methods are summarized, and the development potential of each block element is described in terms of the mechanism. Finally, suggestions and challenges for future electrocatalytic coreduction of CO_2 and NO_3^- research are presented.

1. Introduction

In recent centuries, industrial activity and the burning of fossil fuels have led to excessive emissions of CO_2 and nitrogen oxides (NO_x), severely exceeding the capacity of natural regulation and contributing to environmental degradation [1]. Excessive emissions of CO_2 can lead to the greenhouse effect, and the accumulation of NO_x can lead to water eutrophication, photochemical smog pollution, and ozone layer destruction. Recovering CO_2 and NO_x for the resourceful use of waste to produce more valuable products is a promising and sustainable strategy to mitigate these growing environmental problems, and it is also important for achieving carbon-neutral strategies and closing the NO_x cycle at this stage [2].

Electrochemical CO_2 reduction reactions (CO_2RR) driven by renewable electricity provide a way to reduce waste CO_2 emissions into the atmosphere by simultaneously converting intermittent renewable

energy sources into value-added and stable chemical commodities [3]. Electrocatalytic reduction of nitrogen (N_2RR) is an emerging technology for synthesizing NH_3 from N_2 and water under environmental conditions [4]. Inspired by the ability of the CO_2RR and N_2RR to synthesize NH_3 and carbon products, respectively, researchers have proposed an integrated carbon-nitrogen conversion pathway, namely, the direct production of organonitrogen compounds through C-N coupling under environmental conditions. Electrocatalytic coreduction of CO_2 and nitrogenous substances not only retains the advantages of the CO_2RR but also produces more valuable products than the CO_2RR [5]. Initially, the strategy of coupling NH_3 and CO_2 to prepare organonitrogen compounds was proposed. However, further synthesis of nitrogen-carbon compounds by the reaction of NH_3 with CO_2 depends on extreme industrial conditions, resulting in a complex and unfeasible process [4]. Therefore, researchers further proposed that N_2 and CO_2 could be used to generate organic nitrogen compounds directly by electrocatalysis under ambient

conditions [6]. Although the electrocatalyst used in this strategy achieves efficient C-N coupling, there are still problems in breaking the $N{\equiv}N$ bond of diazine. In recent years, nitrate (NO_3^-) electrocatalytic reduction reactions (NO_3RR) have been shown to avoid these problems while also providing a new approach to closing the NO_x cycle [7]. This method converts waste nitrate or NO_x into NH_4^+, which is further converted into ammonia as a carbon-free energy carrier for the production of chemical feedstocks [8]. Moreover, the dissociation energy of $N{\equiv}N$ (941 kJ mol^{-1}) is higher than that of the N $=$ O bond (204 kJ mol^{-1}), resulting in a low Faraday efficiency for the coupling of CO_2 and N_2 [9–12]. Thus, the coupling of NO_3^- and CO_2 may be the best strategy to drive electrochemical reduction for the preparation of organic nitrogen compounds at this stage.

Electrochemical catalytic CO_2 and NO_3^- coupling reactions have emerged in recent years to recover CO_2 and NO_3^- simultaneously through green electricity to produce valuable amines and their derivatives, such as urea ($CO(NH_2)_2$), methylamine (CH_3NH_2), ethylamine (C_2H_7N), etc. [9,13,14]. Urea, as a typical example, is an important raw material for the chemical industry and the most effective nitrogen source for fertilizers in agriculture. To date, the industrial production of urea has been achieved by the direct reaction of CO_2 with NH_3 under harsh conditions (150–200 °C, 150–200 bar), with an artificial N_2 fixation process consuming 80% of NH_3 production and 2% of global energy [15–17]. Compared to the very high energy consumption of industrial production processes, the electrochemical C-N coupling reaction for the synthesis of urea not only enables resource utilization of CO_2 and NO_x but also serves as a sustainable production route under environmentally friendly conditions using renewable energy sources [18]. Currently, many types of carbon and nitrogen compounds, in addition to urea, have been produced by this strategy [4,9,14,19]. However, due to the complexity of electrochemical C-N coupling, a consensus regarding the C-N coupling mechanism and key coupling intermediates has not been reached. For the same organic nitrogen product, the mechanism of electrocatalytic coreduction of CO_2 and NO_3^- is not unique. The C-N coupling process is often accompanied by the generation of many byproducts, which may be related to the performance of the catalyst or the reaction environment [20]. The prerequisite for achieving C-N coupling is the efficient catalysis of the respective CO_2RR and NO_3RR to form suitable C- and N-intermediates, and these two reduction processes can then generate a variety of byproducts. These intermediates then combine to form the key carbon and nitrogen intermediates, which often depend on the type of catalyst used [21]. Therefore, it is quite challenging to design new catalysts to further improve the coupling yield and efficiency to address the complexity of C-N coupling. As shown in Fig. 1, this paper reviews the

various products of the C-N coupling reaction under this process as a way to summarize the different complex mechanisms of the C-N coupling reaction and to understand the role of different types of intermediates in different C-N coupling reactions. From the perspective of reaction performance, different types of catalysts are summarized to understand the effect of active site modulation on selectivity, and a preliminary practical evaluation of the strategy (using NO_3^- emitted from actual water as the nitrogen source for the C-N coupling reaction) is carried out to provide a practical guide for subsequent studies on the preparation of organic nitrogen by electrochemical coreduction of CO_2 and NO_3^-.

2. Reaction mechanism for the preparation of organonitrogen compounds by electrochemical coupling of CO_2 and NO_3^- reduction

The coactivation of electrocatalytic carbon and nitrogen sources demonstrates the development direction in the synthesis of organic nitrogen compounds. The CO_2RR and NO_3RR processes include multistep proton-electron coupling (PECT) and chemical steps (C-N coupling). In this process, CO_2 and NO_3^- are first converted into various intermediates, such as $*CO_2$, $*CO$, $*COOH$, $NO_2 *$, $*NO$, $*H_2NOH$, $*NH$, and $*NH_2$, through PECT [11,22,23]. These different carbon and nitrogen intermediates are then converted into different C-N intermediates through C-N coupling, which is directly related to the formation of the target product. DFT theoretical calculations show that the important steps (rate-determining steps and potential rate-determining steps, RDS and PDS) in the formation of organic nitrogen compounds occur in the stages before and after carbon-nitrogen coupling [20]. Fig. 2 summarizes the synthesis pathways of different organic nitrogen compounds and the key intermediates of carbon and nitrogen coupling. The carbon and nitrogen organic compounds synthesized by electrocatalytic coreduction of CO_2 and NO_3^- can be classified into single-carbon (C_1) and multicarbon (C_2) products according to the amount of carbon contained in the synthesized products.

2.1. C-N coupling preparation of C_1 products

The C_1 products of C-N synthesized by electrochemical coupling of CO_2 and NO_3^- mainly include carbonic amide (urea) and methylamine. It can be seen from Fig. 2 that the C-based intermediates and N-based intermediates involved in these two products are different, but the most significant difference is observed for the C-based intermediates. The synthesis of urea generally uses $*CO$ as the carbon source, while that of
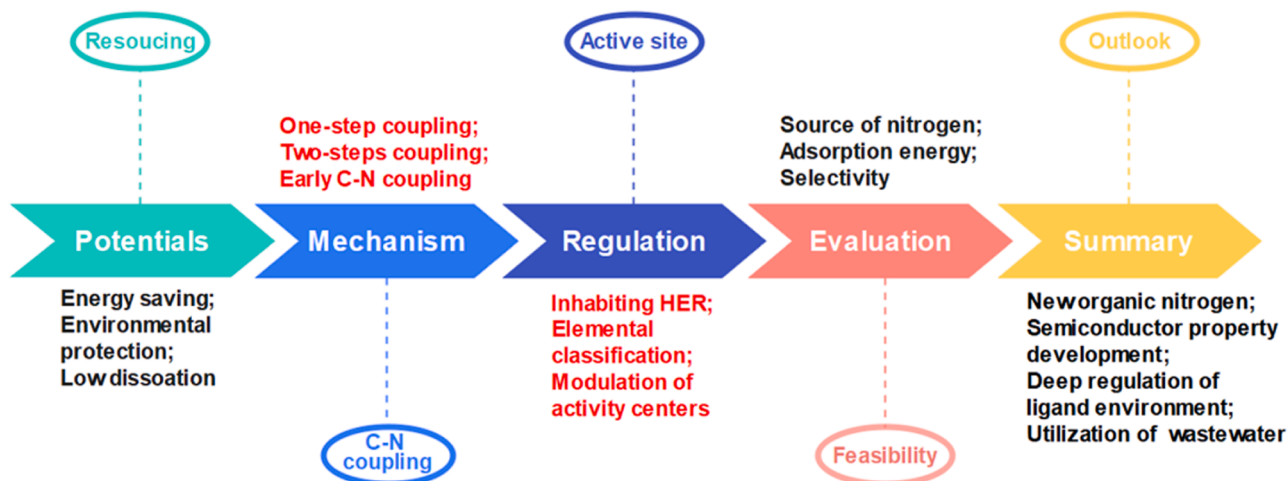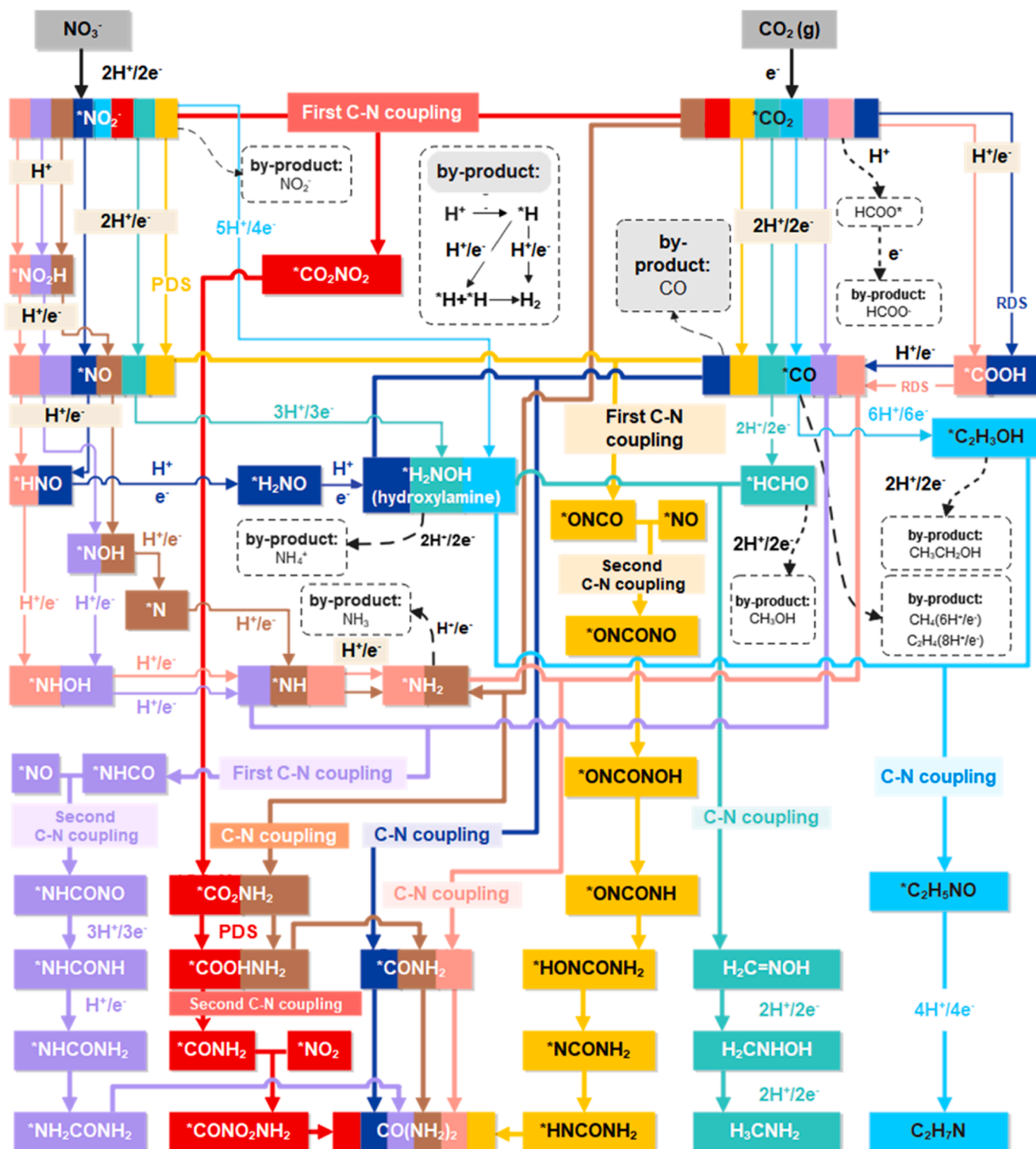

Fig. 1. Electrochemical coupling of CO_2RR and NO_3RR to synthesize carbon nitrogen organic compounds.

Fig. 2. The general mechanism of formation of organonitrogen compounds by electrochemical C-N coupling ($C_1 \sim C_2$ products).

methylamine uses *HCHO. These mechanisms can all occur under environmental conditions, providing greener processes for synthesizing organic nitrides.

2.1.1. C-N coupled synthesis of urea

At present, urea is the most common carbon, nitrogen, and organic matter regarding the electrochemical coupling of CO_2RR and NO_3RR, and C-N coupling is regarded as the key to urea synthesis [20]. C-N

coupling can be classified into two types: one-step coupling and two-step coupling approaches [9,23,24].

Urea synthesis is triggered by different kinds of intermediates [2,25]. The first mechanism for the one-step coupling synthesis of urea is the coupling reaction between the N-OH-based intermediates and *CO (Fig. 2) [20]. The general mechanism of the coupling of N-OH-based intermediates and *CO is $NO_3 \rightarrow *NO_2 \rightarrow *NO \rightarrow *NHO \rightarrow *H_2NO/*HNOH \rightarrow *H_2NOH \rightarrow *OCNH_2$, in which the NO_3RR is sometimes similar to the N_2RR, generally as

*NO→*NHO→*NHOH→*NH$_2$OH [26–30]. In terms of kinetics, studies show that the coupling reaction of *H$_2$NOH and *CO is a spontaneous one-step cooperative reaction, namely, *H$_2$NOH+ *CO→*OCNH$_2$, rather than a two-step reaction (*H$_2$NOH+*CO→*NH$_2$ + *CO→*OCNH$_2$) [20]. The second and third types of C-N coupling are processes in which *CO or *CO$_2$ combines with *NH$_2$, in which *NH$_2$ is also obtained by the reduction of *NO [31]. The main mechanism is shown in Fig. 2.

As shown in Fig. 2, in addition to *NO$_2$, *NO is another N-O-based intermediate obtained by the NO$_3$RR, which is involved in the first two-step C-N coupling mechanism, namely, *CO+ *NO→*ONCO and *ONCO+ *NO→*ONCONO(H) [22]. In some studies, the oxygen site of *NO can be attached to the oxygen vacancy, resulting in an exposed N site, which can promote the combination of the N site of *NO and the C site of *CO. In this way, the reaction energy barrier of the C-N coupling can be decreased to a certain extent, in which the PCET process of *NO does not occur [22]. In contrast, on the surface of catalysts with insufficient oxygen vacancies, the hydrogenation of *NO to obtain *NH occurs [23], which is involved in the second two-step coupling mechanism (Fig. 2). Notably, the C-N coupling reactions involving *NH or *NH$_2$ may contribute to excessive byproducts NH$_3$ or NH$_4^+$. In contrast, the Faraday efficiency of the corresponding nitrogen byproducts of *NO as a nitrogen source is relatively low, but the energy barrier overcome by the coupling of *CO and *NO is higher than that of the coupling of *CO and *NH [22]. The third two-step C-N coupling of urea synthesis is the coupling of *CO$_2$ and *NO$_2$ to form *CO$_2$NO$_2$ and then through the PCET process to generate *CO$_2$NH$_2$, in which the protonation of *CO$_2$NH$_2$ to form *COOHNH$_2$ is considered PDS [2,25]. The coupling of *CO$_2$ and *NO$_2$ is considered an early C-N coupling reaction, which can reduce the yield of byproducts (NH$_3$, N$_2$, CO, or HCOOH) to some extent. In this way, achieving early C-N coupling seems to be a promising mechanism for application, but the types of byproducts seem not to be affected by this mechanism.

From the above coupling mechanisms of urea synthesis, the carbon source for electrocatalytic coreduction of CO$_2$ and NO$_3^-$ is in most cases *CO, which inevitably generates CO and generally in higher yields than NH$_3$/NH$_4^+$ [24]. Therefore, although the prerequisite for C-N coupling is promoting the respective reduction reactions of the CO$_2$RR and NO$_3$RR to generate C-based intermediates and N-based intermediates, the products of these two reactions are competitive. Currently, the control of competitive products is inhibiting CO$_2$RR by promoting NO$_3$RR [25]. Previous studies suggested that the electron pair of N$_2$ could donate electrons and could be regarded as a Lewis base. In the N$_2$RR, a Lewis acid site can be created by constructing empty orbitals to accommodate electrons to activate N$_2$ [23]. Similarly, in the electrocatalytic coreduction of CO$_2$ and NO$_3^-$, it is feasible to construct artificial Lewis acid sites by modulating electron transfer to appropriately lower the energy barrier for C-N coupling or to enhance the adsorption of free radicals (e. g., *NO, *NH) on the active site to improve the performance of the catalyst.

2.1.2. C-N coupled synthesis of methylamine

The potential of electrocatalytic coreduction of CO$_2$ and NO$_3^-$ for the production of organic nitrogen compounds has been demonstrated in the synthesis of urea. However, more advanced catalytic processes are still needed to extend the reaction range to produce more valuable products, such as alkylamines [9]. The simplest of alkylamines is methylamine, which is generated from methanol (CH$_3$OH) and NH$_3$ derived from fossil fuels under high temperature and pressure under industrial conditions and is an important component of valuable chemicals, including pharmaceuticals and agricultural chemicals [9,32]. In this way, the electrochemical coreduction of CO$_2$ and NO$_3^-$ as carbon and nitrogen sources can provide a greener process for the generation of methylamine and other related organic nitrogen compounds [9]. CO$_2$ and NO$_3^-$ can be reduced to methylamine (FE=13%) in an aqueous medium under the catalysis of a multiphase molecular cobalt catalyst on carbon nanotubes. This process involves the transfer of 14 electrons and

15 protons per mole of product [9]. Methylamine is formed in an unprecedented eight-step cascade over a single electrocatalyst. The main C-N coupling step for the formation of methylamine is the spontaneous condensation of *NH$_2$OH and formaldehyde (HCHO) to form formaldoxime as the key intermediate [33,34]. This process can also be attributed to *NH$_2$OH easily forming oxime with aldehydes [35,36].

As shown in Fig. 3a, the whole reaction is an unprecedented eight-step electrocatalytic cascade. Electrochemical CO$_2$RR and NO$_3$RR occur until HCHO and *NH$_2$OH, respectively, are generated, which is divided into five steps. The formation of *NH$_2$OH is consistent with that of *NH$_2$OH in urea synthesis, namely NO$_3^-$→*NO$_2^-$→*NO→*H$_2$NOH (Fig. 3b). However, after CO$_2$ forms *CO through the PCET process, *CO is further reduced to HCHO* , accompanied by the formation of CH$_3$OH. CH$_3$OH is not an intermediate for producing methylamine. The adsorbent HCHO* is then rapidly attacked by the *NH$_2$OH nucleophile to produce methoxime, which is further electrochemically reduced to N-based methyl hydroxylamine and then to methylamine.
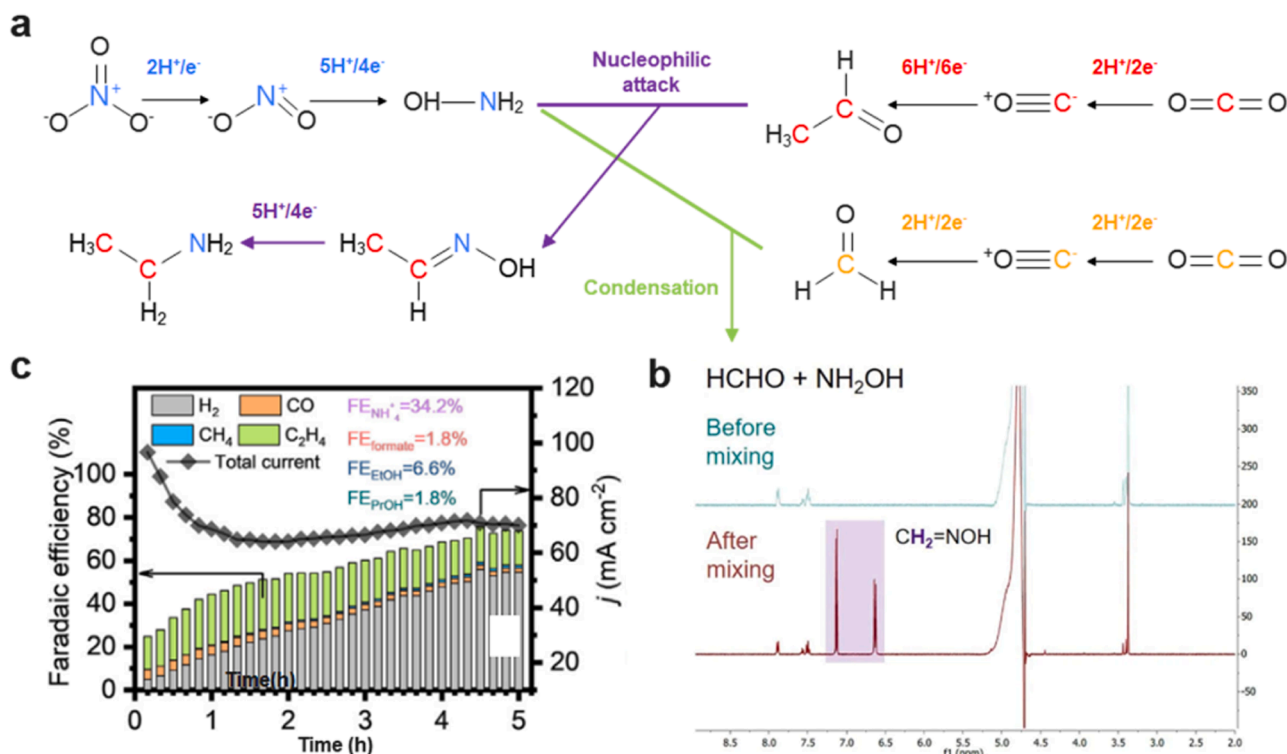
2.2. C-N coupling preparation of the C$_2$ product (ethylamine)

The mechanism of C-N coupling to generate ethylamine is shown in Fig. 3a. The key N-based intermediate (nitrogen source) is also *H$_2$NOH, but the carbon source is *C$_2$H$_3$OH produced by *CO through the reaction of 16 electrons and 17 protons, rather than HCHO [14]. Acetaldehyde is a crucial intermediate in this process. Acetaldehyde oxime (C$_2$H$_5$NO) is further reduced from acetaldehyde (an active reaction intermediate that reduces CO$_2$ to ethanol) and *NH$_2$OH (an intermediate that reduces NO$_3^-$ to NH$_3$) to form the final product ethylamine. Among them, the reductions of acetaldehyde to ethanol and *NH$_2$OH to NH$_3$ are competitive reactions, and their presence limits the selectivity of ethylamine (Fig. 3c).

Notably, another related compound of C$_2$H$_5$NO is acetamide [19]. The essential difference between acetamide and acetaldehyde oxime is that the C atom attached to the C site of the methyl group forms a double bond with O. In contrast, the C site of acetaldehyde oxime is connected to N. The synthesis of acetamide was achieved by combining the intermediates *NH$_2$OH and acetaldehyde produced during NO$_3$RR and CO$_2$RR, respectively, to form acetaldoxime and then further reduction, which also provides a new idea for the formation of amide compounds by C-N coupling [4,37].

In summary, the focus of research on the synthesis of organic nitrogen by electrocatalytic coreduction of CO$_2$ and NO$_3^-$ at this stage is mainly the preparation of urea. In recent years, the coactivation of carbon and nitrogen sources and electrocatalytic C-N coupling for the in situ formation of carbon and nitrogen organic compounds have directed the development of urea synthesis. However, the electrocatalytic C-N coupling process for the synthesis of urea still suffers from various competing reactions, such as the simultaneous CO$_2$RR and NO$_3$RR and the inevitable hydrogen evolution reaction (HER) at negative potentials, resulting in the generation of various byproducts and low efficiency of urea synthesis [23]. According to Fig. 2, the first step in the electrocatalytic coreduction of CO$_2$ and NO$_3^-$ is the respective electroreduction of CO$_2$ and NO$_3^-$. However, the separate electroreduction reactions of CO$_2$ and NO$_3^-$ compete strongly with the desired C-N coupling reaction, leading to the generation of byproducts such as CO, HCOOH, and NH$_3$ in addition to H$_2$ and even the generation of C$_2$ byproducts, which seriously affects the product selectivity [38]. Among these byproducts, H$_2$ and CO usually account for a larger proportion. In addition to the HER competition issue that needs to be addressed, although CO sometimes needs to be activated to *CO to participate in C-N coupling, excessive CO content can cause catalyst poisoning, further hindering the NO$_3$RR and C-N coupling and greatly reducing the efficiency of the synthesis of carbon-nitrogen organic compounds [20]. Although CO has many uses in today's industry, CO can be effectively prepared by using the CO$_2$RR alone rather than using C-N coupling. Initially, the NO$_3$RR was proposed for the ultimate purpose of closing the NO$_x$ cycle, and the CO$_2$RR and

Fig. 3. Mechanism of electrocatalytic co-reduction of CO_2 and NO_3^- for the preparation of methylamine and ethylamine [9,14]. (a) Formation of methylamine and ethylamine. (b) ^1H NMR spectra of 25 mmol L^{-1} HCHO dissolved in electrolyte solution before and after adding 50 mmol L^{-1} NH_2OH, where the peaks pertaining to formaldoxime are highlighted in purple [9]. Copyright 2021 Springer Nature. (c) Product distribution and total current density for a 5 h coreduction electrolysis; the average liquid product FEs were measured after the electrolysis [14]. Copyright 2022 Elsevier.

NO_3RR were coupled to transform waste carbon and nitrogen-containing substances into more valuable products. In this way, the high selectivity of CO in the C-N coupling system needs to be addressed [39]. Similarly, ammonia byproducts (NH_3, NH_4^+, NH_2OH) are inevitably generated during the NO_3RR alone, and these ammonia byproducts mainly originate from a series of PCET reactions of N-based intermediates (*NH_2OH, *NH_2, *NH, etc.), sometimes with higher yields than even CO at the optimum reduction potential [20]. Therefore, at this stage, in the field of electrocatalytic coreduction of CO_2 and NO_3^-, in addition to the HER, the formation of the remaining high-yield byproducts needs to be suppressed.
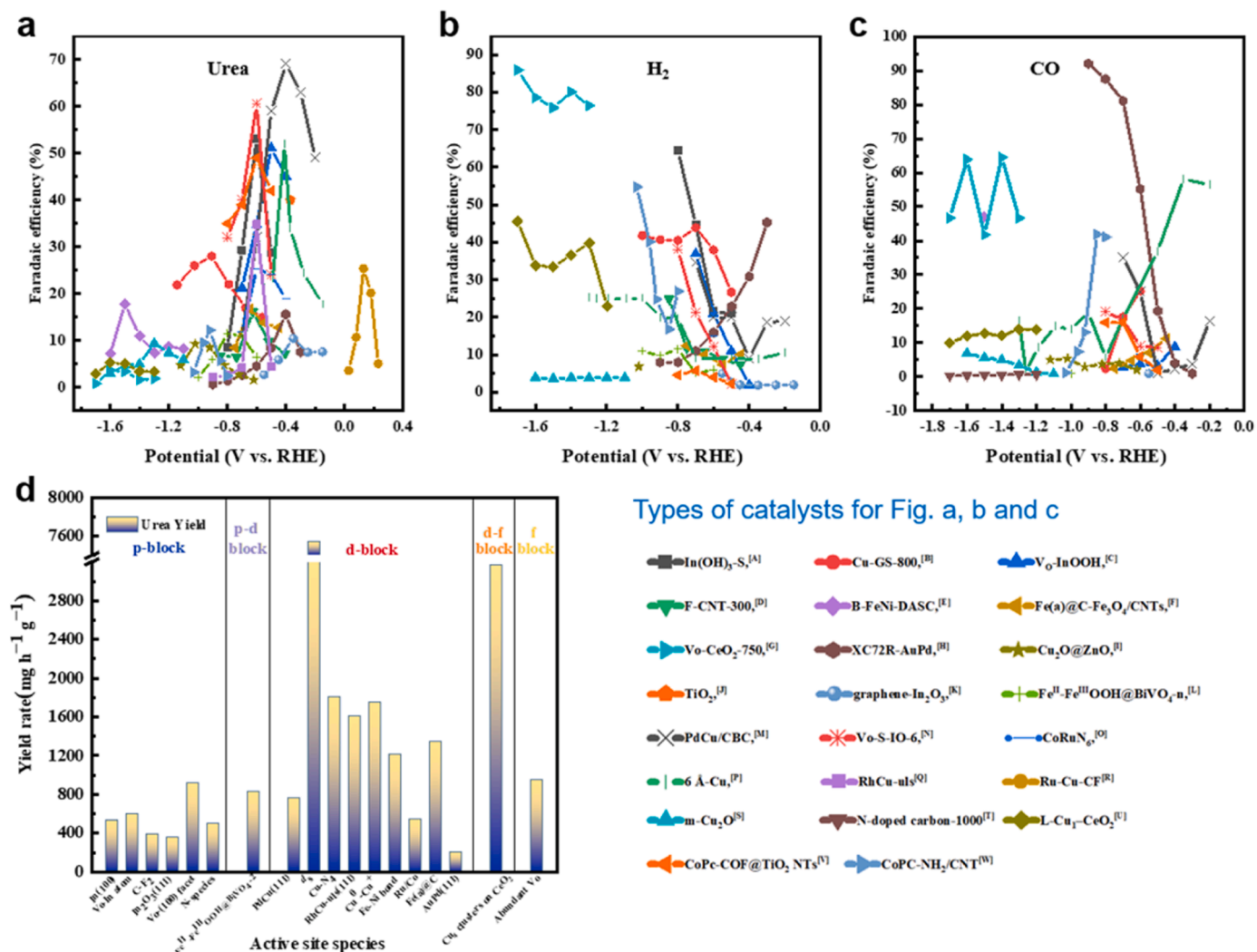
3. Construction strategies of active catalytic sites and coordination environment

It is not difficult to see that the selectivity of organic nitrogen is an important index to evaluate the C-N coupling process, and this index is closely related to the catalyst. That is, the design of the catalyst determines excellent catalytic performance [40]. Current metal and metal-free catalysts have excellent performance in the electrocatalytic coreduction of CO_2 and NO_3^-, but the catalytic center is still concentrated on metal elements [31,41]. Fig. 4 summarizes the performance of different types of catalysts for the electrocatalytic coreduction of CO_2 and NO_3^-. In addition to the initial comparison of the selectivity (Faradaic efficiency) for the synthesis of organic nitrogen (Fig. 4a), the production of the two main byproducts (H_2 and CO) in the respective systems mentioned above is compared to provide a more in-depth assessment of the catalytic performance through the inhibition of the byproducts (Fig. 4b and c). Fig. 4d further compares the respective organic nitrogen yield rates of the different active sites. Apart from bimetallic catalysts, indium seems to be selective for the synthesis of organic nitrogen compared to other single metal catalysts. However, the performance of an electrocatalyst should be evaluated not only

regarding the selectivity of the target product but also in terms of its inhibition of competitive reactions or even the effect of the intrinsic nature of the active site contributing to C-N coupling.

The performance of catalysts for the electrocatalytic coreduction of CO_2 and NO_3^- is significantly influenced by the elemental species within the catalytic active site and the active site coordination environment [23]. Regarding metal-based catalysts, different metal atoms, metal coordination structures, or coordination environments all play different roles in the occurrence of intermediate adsorption, activation, and coupling reactions [42–49]. Metal-free elements such as fluorine-doped carbon nanotubes have also been shown to catalyze the synthesis of urea [31]. The elemental species within the active site may determine the class of the reaction product, and the coordination environment of the active site may determine the yield of the product [50]. Thus, reasonable selection of the active site elements and adjustment of the coordination environment of the active center become the key to improving the catalyst performance.

According to previous studies, the central elements of the catalyst active site can be broadly divided into two categories: p- and d-block elements. Previous studies suggested that catalytic systems with d-block elements tended to be less selective in the synthesis of organic nitrogen and less able to inhibit competitive reactions. However, in N_2RR catalytic systems, p-block elements have been shown to possess superior HER inhibition performance to d-block elements. This performance has also been demonstrated at this stage in the field of electrocatalytic coreduction of CO_2 and NO_3^-. However, it is not sufficient to improve the selectivity of organic nitrogen by the type of elements alone. In addition to element selection, the methods of designing a coordination environment to regulate the active sites also determine the selectivity of the target product [51]. For example, d-block bimetallic metal sites can be designed, similar to p-block metals, to enhance the adsorption of free radicals to inhibit byproduct synthesis. Defect engineering, such as the design of oxygen vacancies (Vo), can reduce the reaction energy barrier

Fig. 4. Comparison of catalytic properties of electrochemical coupling CO$_2$RR and NO$_3$RR. (a) FEs ([A-V]: urea; [W]: methylamine); (b) Comparison of inhibition of HER by different catalysts; (c) Comparison of inhibition ability of different catalysts to CO overproduction; (d) The urea yields at different active sites. The data were obtained from the following studies: [A] Lv et al. [2]; [B] Leverett et al. [38]; [C] Lv et al. [25]; [D] Liu et al. [31]; [E] Zhang et al. [23]; [F] Geng et al. [68]; [G] Wei et al. [22]; [H] Wang et al. [20]; [I] Meng et al. [40]; [J] Saravanakumar et al. [53]; [K] Mao et al. [84]; [L] Yin et al. [83]; [M] Zhang et al. [119]; [N] Li et al. [136]; [O] Liu et al. [117]; [P] Shin et al. [124]; [Q] Fu et al. [122]; [R] Qin et al. [121]; [S] Qiu et al. [123]; [T] Chen et al. [82]; [U] Wei et al. [145]; [V] Li et al. [85]; [W] Wu et al. [9].

for C-N coupling and promote the production of organic nitrogen compounds. These two strategies correspond to the design of catalytic center structures in the first and second shells of the catalyst, respectively. Thus, the selection of elements and subsequent deep tuning is essential to improve the selectivity of organic nitrogen compounds.
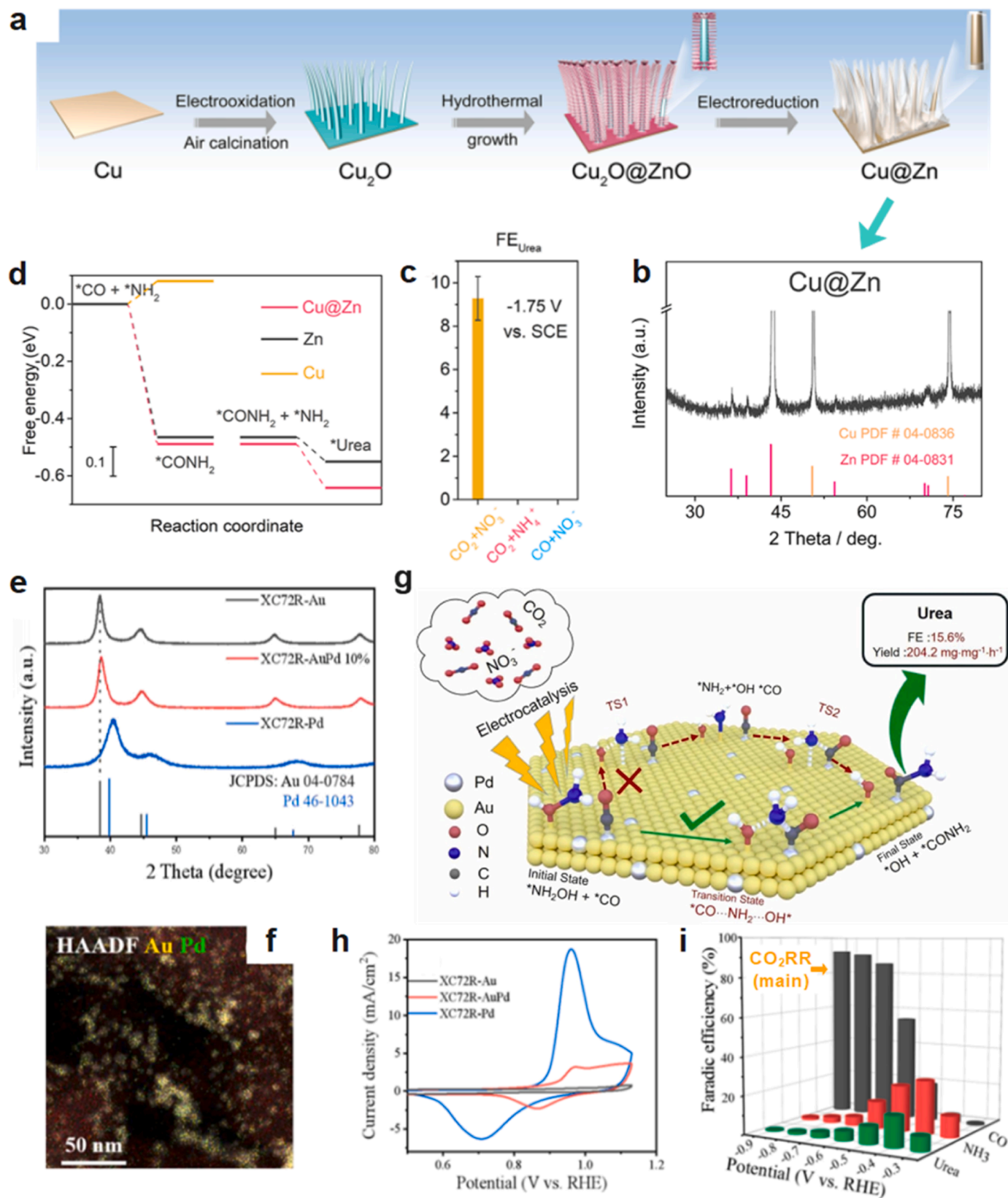
3.1. Selection of active site elements

The selectivity of the electrocatalytic coupling of the CO$_2$RR and NO$_3$RR depends mainly on the properties of the central elements. In the case of metal elements, different metal centers show different selectivities and activities. Notably, these metals include both p- and d-block metal elements. The difference in performance between p- and d-block metal elements is mainly due to their respective unique electronic structures.

3.1.1. D-block elements

Regarding the electrocatalytic coreduction of CO$_2$ and NO$_3$ with d-block element catalysts, the main elements are transition metals, such as Ti, Cu, Pd, Ni, and Fe [20,23,52]. Early urea synthesis by

electrochemical coupling of the CO$_2$RR and NO$_3$RR under acidic conditions was realized on a TiO$_2$/Nafion nanocomposite electrode, which mainly involved the coupling of *CO and *NH$_2$. Control experiments demonstrated that the electrons in the TiO$_2$ conduction band could catalyze the CO$_2$RR and NO$_3$RR simultaneously [53]. The synthesis of CO via the CO$_2$RR and NH$_3$ via the NO$_3$RR can increase the efficiency of C-N coupling while inhibiting the HER, which is important for efficient urea synthesis [40]. Among other d-block metals, Zn is effective in catalyzing CO$_2$ to CO and NO$_3$ to NH$_3$ [12]. Zn nanostructured electrodes have been proposed as the element of choice for direct urea synthesis. However, the low melting point of Zn makes the synthesis of Zn nanoparticles by conventional wet chemical or deposition methods challenging [54–56]. At this point, another strategy, namely, the construction of electron-deficient metals to catalyze the NO$_3$RR, was proposed [40,54]. The difference in the work function of Cu and Zn can cause electron transfer from Zn to Cu to obtain electron-deficient Zn [57, 58]. In this way, oxide-derived ZnO-Cu$_2$O nanocatalysts were developed [40]. The XRD results show that the original catalyst was converted to Cu and Zn metals after electrochemical reduction, and no alloy was formed (Fig. 5a and b) [40,59,60]. XPS and Raman spectra further

Fig. 5. D-block metallic elements catalyze C-N coupling. (a)Schematic illustration for the synthesis of the Cu@Zn catalyst; (b) XRD patterns and SEM images of Cu@Zn; (c) FE_{NH4+} for the electrochemical reduction of NO_3^- and the mixture (NO_3^-+CO_2) over Cu@Zn; (d) C-N coupling on Cu@Zn, pure Zn, and pure Cu surfaces [40]. Copyright 2022 American Chemical Society. (e) XRD patterns of Au&Pd series catalysts; (f) HAADF-STEM image and corresponding elemental mappings of XC72R-AuPd-10%, where Au and Pd atoms are represented by yellow and green pixels, respectively; (g) C-N coupling path on XC72R-AuPd catalyst; (h) CO stripping patterns of XC72R series catalysts; (i) The FE of urea, CO and NH_3 for XC72R-AuPd at different potentials [20]. Copyright 2022 Elsevier.

proved that Cu was surrounded by Zn, and the core-shell crystal surface corresponds to Cu(111) and Zn(100), respectively. Cu_2O-ZnO showed better efficiency in inhibiting the overproduction of CO, but the yield of byproduct NH_4^+ remained high, and the Faraday efficiency of urea was only 9.28% (Fig. 5c). As shown in Fig. 5d, the C-N coupling of this process was the coupling of *CO and *NH_2, and Cu_2O-ZnO reduced the reaction energy barriers of CO_2 to CO and NO_3^- to NH_2. In addition, the C-N coupling at the Cu_2O-ZnO surface was also a spontaneous exothermic process, so the synthesis of urea could be attributed to the increased ability to synthesize *CO and *NH_2 intermediates and the rapid coupling of carbon and nitrogen sources. Notably, in recent years, the Faraday efficiency of CO in reaction systems catalyzed by Cu-Zn catalysts was much lower than that of NH_4^+, which was most likely related to the high coverage of *NH_2 or NO_3^- on the catalyst surface, preventing the CO_2RR to some extent; however, this also led to a large production of the competing product NH_4^+.

Alloying is a feasible strategy that employs d-block metallic elements [20,61,62]. Examples include the alloyed d-block transition metal-based material XC72R-AuPd. The preparation of this catalyst was mainly based on the proper adsorption of *CO by Pd to catalyze C-N coupling [20]. Unlike the above Cu_2O and ZnO coloaded catalysts, as shown in Fig. 5e, with the displacement of the diffraction peaks on the Au(111) crystal plane, the high-angle annular dark-field scanning transmission electron microscopy (HAADF-STEM) and elemental mapping images (Fig. 5f) showed a high overlap of Au and Pd, indicating that the Pd atoms were alloyed to the exposed (111) crystal plane of Au and that Pd was uniformly distributed in the Au nanoparticles. Fig. 5g shows that the C-N coupling mechanism of urea synthesis corresponding to the catalyst mainly consisted of the spontaneous thermodynamic coupling of *CO and *NH_2OH (−1.29 eV). Notably, in addition to urea, the reaction system also includes the generation of H_2, NH_3, CO, NH_2OH, and other byproducts. Among them, the main byproducts corresponding to the CO_2RR and NO_3^-RR are CO and NH_3, respectively. CO is an intermediate product of the CO_2RR and is a crucial intermediate in C-N coupling, forming *CO by adsorption on the catalyst surface [20,55]. CO production originates from the strong adsorption of CO by Pd, while Au has difficulty adsorbing CO, as shown by electrochemical CO-stripping measurements (Fig. 5h). It is difficult to produce *CO if the adsorption capacity of CO is too low, and an excessively high capacity will result in catalyst poisoning. Therefore, introducing a small amount of Pd in XC72R-Au was beneficial to improve the adsorption of CO on the catalyst surface without causing catalyst poisoning, which was the core strategy of this catalytic mechanism [20]. For the byproduct CO, a lower applied potential value resulted in more active sites occupied by CO_2RR and stronger competition from CO, which prevented NO_3^-RR and C-N coupling (Fig. 5i). The direct coupling of *H_2NOH and *CO in this coupling process easily occurred both thermodynamically (−1.29 eV) and kinetically. In addition, the bond lengths of N-OH (2.457 Å) and C-N (1.365 Å) of *H_2NOH and *CO in the transition state were longer than those of *H_2NOH (1.449 Å) and the product *$OCNH_2$ (1.347 Å), indicating that the N-OH bond breakage was accompanied by the formation of C-N, which was consistent with a one-step coupling reaction. However, a small amount of NH_2OH was observed among the byproducts, which was speculated to be related to the rate of the NO_3^-RR.

As a comparison, as shown in Fig. 6a, the N-based intermediate involved in the preparation of ethylamine using an oxide-derived d-block metal Cu catalyst was also *NH_2OH, while there was no NH_2OH among the byproducts, and similarly, no acetaldehyde was found among the byproducts [14]. The researchers attributed this phenomenon to the fast and competitive nature of the CO_2RR and NO_3^-RR for C-N coupling (CO_2 to ethanol, NO_3^- to NH_4^+), mainly due to the undetectable production of acetaldehyde and NH_2OH in both electroreduction reactions [35]. In addition, the rate of reduction of acetaldoxime to ethylamine was much slower than the rates of the CO_2RR and NO_3^-RR, resulting in the low Faraday efficiency of ethylamine (Fig. 6b). However, this was a successful example of the synthesis of polycarboamines using C-N
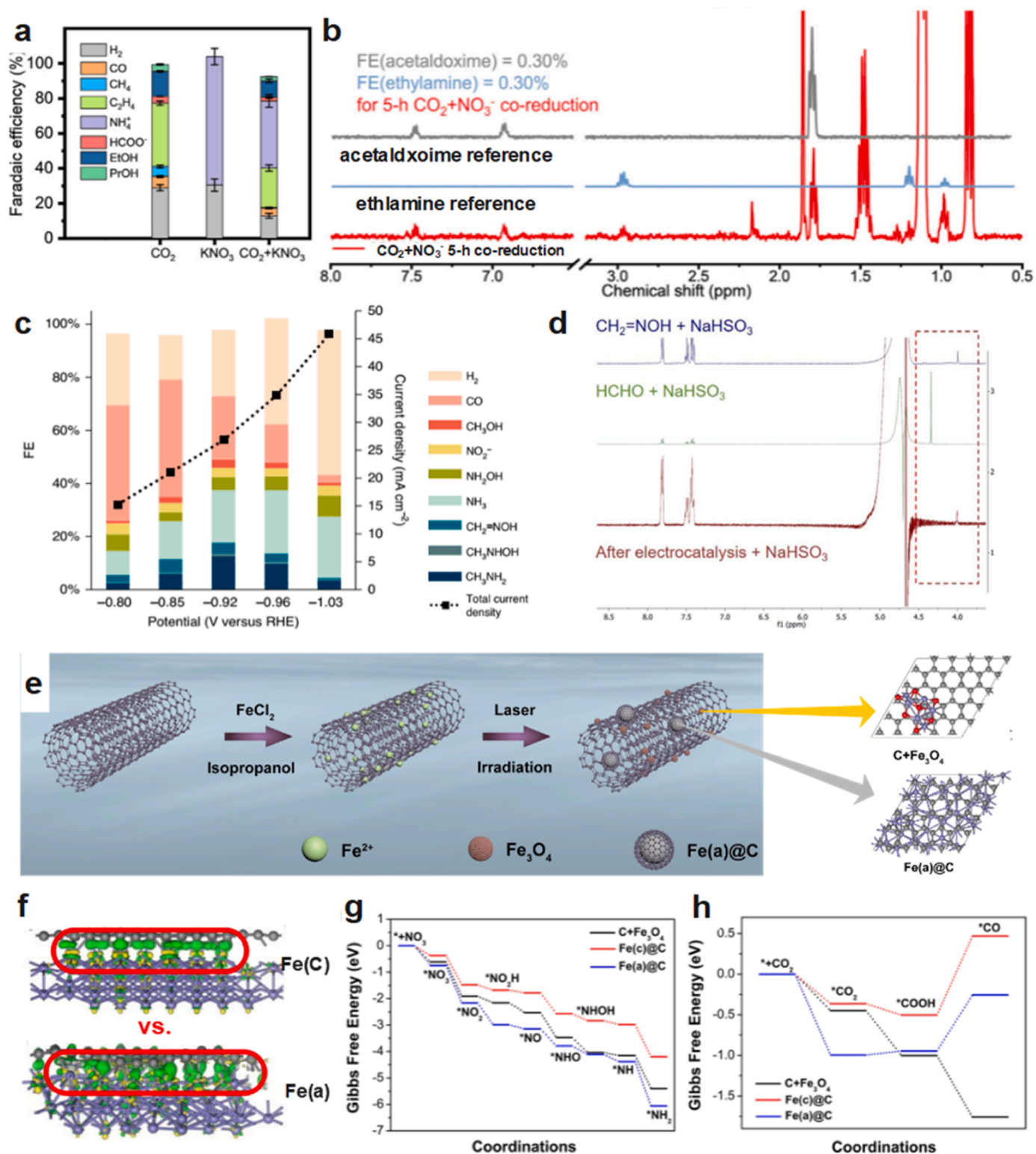
coupling reactions of aldehydes and hydroxylamine intermediates near the electrode surface produced by the CO_2RR and NO_3^-RR, respectively, and this work demonstrates the possibility of the electrochemical synthesis of C_{2+} carbon-nitrogen compounds from inexpensive and abundant inorganic feedstocks, laying the foundation for future studies [14]. For the preparation of ethylamine by electrocatalytic coupling of the CO_2RR and NO_3^-RR, the main idea comes from the synthesis of methylamine, as shown in Fig. 3. Initially, metal phthalocyanine coordination complexes were shown to catalyze the synthesis of NH_3 from the NO_3^-RR with *NO_2 and *NH_2OH as the main intermediates [63]. The electrocatalytic coreduction of CO_2 and NO_3^- synthesis of methylamine was mainly achieved by using the d-block metal Coβ-tetraminophthalocyanine/carbon nanotubes ($CoPc$-NH_2/CNT) to catalyze the synthesis of formaldehyde as an intermediate in the synthesis of methanol from the CO_2RR and *NH_2OH as a carbon and nitrogen source in the synthesis of NH_3 from the NO_3^-RR. The byproducts of the process were still dominated by H_2 and CO, and since the bisulfite derivatization method could not detect trace amounts of HCHO, NH_2OH was detected in the final product. Therefore, the researchers attributed the occurrence of the even step to the spillage of NH_2OH (Fig. 6c and d) [9].

Among d-block metal elements (such as Cu, Fe, Ni, and Pd), to further understand the activation mechanism of small molecules on d-block metal catalysts, an "accept-give" mechanism can be introduced [64]. When the adsorbent (*OO, *NN, *CO) is attached to the metal, the lone pair electrons from the adsorbent transfer to the d orbital of the empty d-block metal elements, or the partially filled metal d electrons transfer to the π* orbital of the adsorbent, thereby activating the adsorbent [64,65]. For a single active site, although the D-block metal base material shows good catalytic activity, its ability to inhibit the HER is poor [66,67]. This is also why the hydrogen Faraday efficiency is high in the hydrogen evolution reaction of d-block metallic elements compared with p-block metals (Fig. 4c). To solve this problem, a feasible strategy seems to be the construction of dual sites, such as the construction of carbon-coated amorphous (amorphous) iron (Fe(a)@C) and Fe_3O_4 NPs coloaded with Fe(a)@Fe_3O_4 NPs containing two iron-based sites (Fig. 6e), whose excellent HER inhibition can be seen in Fig. 4c [68]. Unlike the alloyed AuPd, as shown in Fig. 6f, it can be seen from the comparison between the two sites of Fe(a)@C and the crystalline state of Fe (Fe(c)@C) that at the Fe(a)@C site, C can gain electrons from Fe, significantly increasing the chemical activity and thus resulting in efficient catalytic reduction of NO_3^- to *NH_2 (Fig. 6g). At the same time, C+Fe_3O_4 also showed excellent catalytic ability to reduce CO_2 to *CO (Fig. 6h). In conclusion, this study designed d-block metal complexes for different types of ferro-based activation sites, and the excellent catalytic performance was attributed to the synergistic effect of the two active sites. However, it should be considered that the high yield of NH_3 in this reaction system may also be related to the minimum energy barrier for Fe(a)@C to adsorb NO_3^- and reduce to NH_3 or to the high desorption energy (−5.699 eV) of Fe(a)@C itself, that is, *NH_2 is easily detached from Fe(a)@C [68]. Subsequently, it is partially transferred to the Fe_3O_4 site to bind with *CO, and the C-N coupling reaction occurs. Although this process is the core of the coupling reaction, it does not rule out the possibility of catalyzing the NO_3^-RR to generate the byproduct NH_3 efficiently.

3.1.2. p-Block elements

Early on, researchers suggested that the main advantage of p-block elements over d-block elements was that they could inhibit the HER well [67,69]. In recent years, research on the electrocatalytic N_2RR synthesis of NH_3 has shifted from d-block element catalysts to focus on the design of p-block element-based catalysts to eliminate the inherent limitations of the N_2RR, promote the N_2RR, and inhibit the HER [69]. Although p-block elements have a partially occupied valence p-orbital similar to TMs, their hydrogen adsorption capacity is poor, which is also why p-block elements such as B, C, and Bi can inhibit the HER [70–73].

Fig. 6. Synthesis of methylamine and ethylamine by electrochemical coupling of CO_2RR and NO_3^-RR(a-d) [9,14]. (a) The ethylamine product distribution (FE) for CO_2 reduction, NO_3^- reduction, and CO_2 and NO_3^- coreduction; (b) ^1H NMR spectrum of the post-electrolysis solution [14]. Copyright 2022 Elsevier. (c) Potential-dependent product distribution (FE) and total current density of CoPc-NH_2/CNT for the coreduction of CO_2 and NO_3^-; (d) ^1H NMR spectrum of the catholyte solution after coreduction mixed with 1 mol L^{-1} NaHSO$_3$ [9]. Copyright 2021 Springer Nature. Urea synthesis on the surface of Fe(a)@C-Fe$_3$O$_4$/CNTs(e-h). (e) Schematic illustration of the synthetic process of Fe(a)@C-Fe$_3$O$_4$/CNTs; (f) Charge density difference structures of C on Fe(c)@C and Fe(a); (g) Free energy profiles of NO_3^- to *NH_2 on C +Fe$_3$O$_4$, Fe(c)@C and Fe(a)@C; (h) Free energy profiles of CO_2 to *CO on C +Fe$_3$O$_4$, Fe(c)@C and Fe(a)@C [68]. Copyright 2023 John Wiley and Sons.

However, the electronic structure of most p-block element catalysts is not similar to that of d-block element catalysts, the latter of which can contribute to the activation of N_2 molecules, thus also limiting the further study of this type of catalyst [74]. The N_2RR is closely related to the activation of triple bonds in N_2 molecules. Many previous studies focused on d-block metals, ignoring the advantage of p-block elements. These studies show that N≡N activation is mainly dependent on the "π back-donation" (π electron feedback) mechanism of d-block metallic elements' d-electron-orbital. Commonly used catalysts mainly include transition metals, but most transition metal-based catalysts cannot inhibit the HER effectively, which leads to a low Faraday efficiency [69]. To exploit the inhibition of HER by the p-block elements, N_2 was successfully activated through modulation of the surface electronic structure, which resulted in an interaction between the catalyst and the N_2 small molecule similar to π back donation [74]. For example, in the initial stage, bicoordinated boron with an empty sp^2 orbital and an occupied p-orbital (boride group) similar to a π back-donation process can effectively catalyze the N_2RR [75]. Late modification of phosphorus and bismuth showed excellent N_2RR catalytic performance [76–78].

Each nitrogen atom in N_2 has unpaired electrons that can donate electrons to the strong electron acceptor and act as a weak Lewis base [69]. To effectively activate N_2 and avoid the formation of metal-hydrogen bonds, Lewis acid catalytic sites with strong electrophilicity are necessary, and the creation of Lewis acid sites depends on the unoccupied orbitals (empty orbitals) that accommodate the lone pair of electrons of the N_2 molecule [69]. As shown in Fig. 7a, although the p-block metal Bi lacks an intrinsic Lewis acid site and has difficulty activating N_2 through Lewis acid—base interactions, interestingly, the Bi-Bi bond can be broken by the introduction of oxygen vacancies and hydroxyl groups, producing empty p orbitals that can act as Lewis acid sites to accommodate the lone pair of electrons of N_2 [69]. Empty orbitals can be generated by surface molecular modification or defect engineering strategies, which also inspires research ideas for the NO_3^-RR and even coupling of the CO_2RR and NO_3RR.

At the same time, in addition to metal materials, carbon-based materials also show good performance, such as nitrogen-doped carbon materials (notably, nitrogen-doped carbon materials have been used in the field of coreduction synthesis of urea by electrocatalysis of CO_2 and the NO_3RR, as shown in Fig. 4a) [31]. However, this is only the first step of nitrogen reduction. Despite excellent achievements in the development of advanced p-block element-based N_2RR electrocatalysts, increasing the NH_3 yield remains challenging due to the inherent properties of N_2, including an extremely high activation barrier and low water solubility. Therefore, using another nitrogen-containing source (NO_3^-) is a strategy to avoid this problem. Although synthesizing NH_3 from the NO_3RR involves two more electrons than the N_2RR, the former process has an advantage because there is no N≡N bond cleavage process [79]. NO_3^- usually exists in the aquatic environment and comes from nitrogen-containing fertilizers, animal manure, and industrial nitrogen oxide emissions, which have harmful effects on the human body [80]. The electrocatalytic NO_3RR process can simultaneously achieve NO_3^- removal and NH_3 production, representing sustainability.
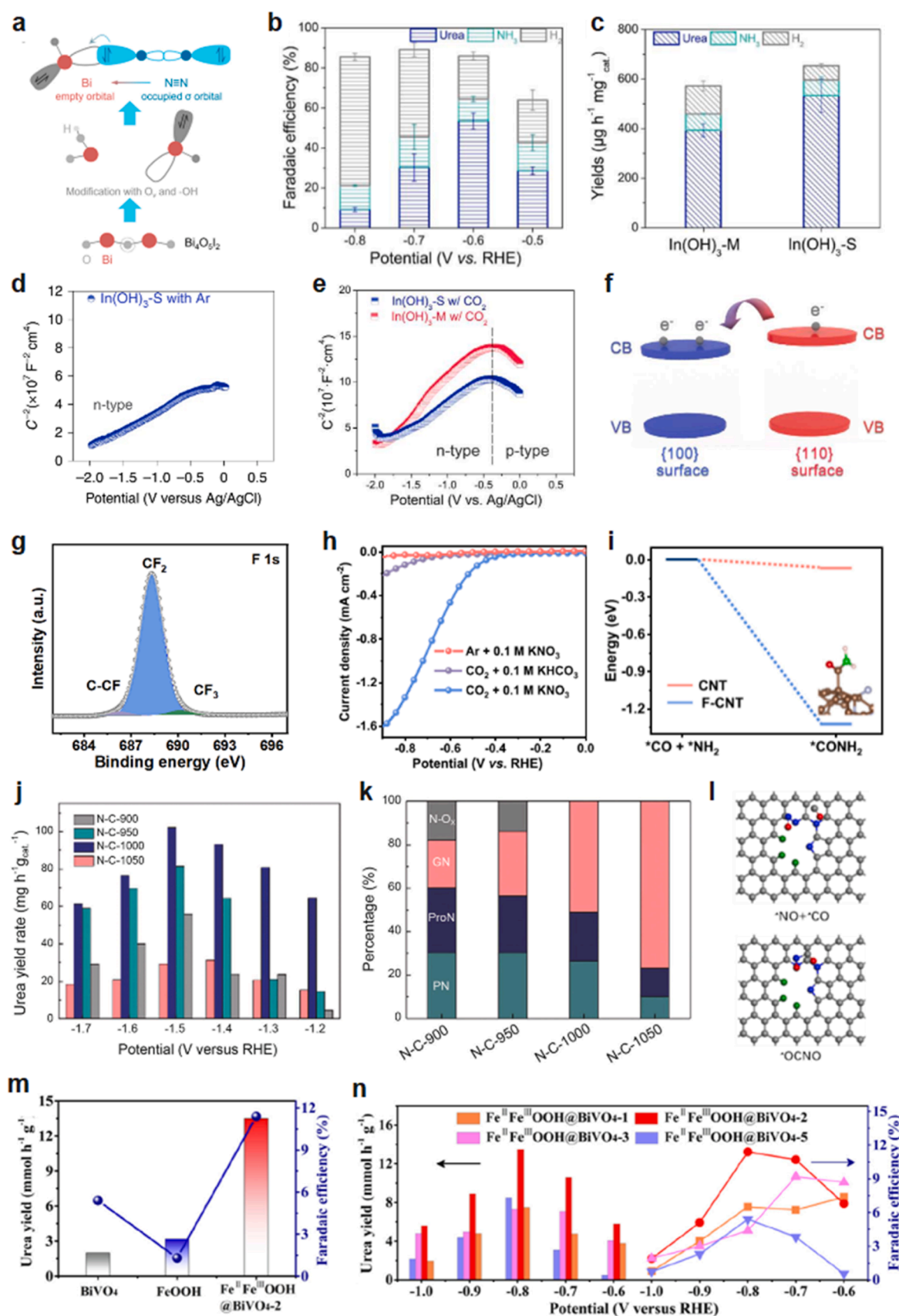
In summary, unlike d-block metals, p-block elements have achieved good results from their initial development and utilization in the catalytic N_2RR to prepare NH_3 and now the simple NO_3RR to prepare NH_3, and p-block elements also exhibit unique chemical properties [67]. However, at present, the main NO_3RR product generated by these elements is NH_3, which is unsuitable for preparing organonitrogen compounds. For example, among the p-block metals, Al, Sn, Bi, and Sb were shown to promote N_2RR [66], but for the electrochemically coupled CO_2 and NO_3RR, the N_2RR product is sometimes a byproduct, but the ability of the p-block metals to inhibit the HER, as shown by their unique electronic structure, has attracted attention. As shown in Fig. 4a and c, the indium metal in the p-block exhibits higher catalytic performance and weaker HER performance than Au, Pd, Cu, Fe, etc., in the d-block [66]. These unique properties of the highly efficient catalytic N_2RR can

also be applied to the present stage of electrocatalytic coreduction of CO_2 and NO_3^- with remarkable results.

$In(OH)_3$-S with (100) crystal planes prepared by the solution heating method has been proven to have better catalytic performance than $In(OH)_3$-M with (100) and (110) mixed crystal planes [2]. $In(OH)_3$-M and $In(OH)_3$-S are similar in phase, size, surface chemistry, and effective surface area except for the additional (110) crystal planes, but their properties differ greatly, as shown in Fig. 7b. Under − 0.6 V vs. RHE conditions, the Faraday efficiency of urea synthesis by the CO_2RR coupled with the NO_3RR catalyzed by $In(OH)_3$-S reached a maximum, and the production rates of the main and byproducts also showed significant differences (Fig. 7c).

Notably, the favorable ability of $In(OH)_3$-S to inhibit the HER during electrochemical coupling of the CO_2RR and NO_3RR is mainly related to proton rejection, mainly due to the change in the CO_2-guided semiconductor type [2]. By considering both Fig. 7d and e, it can be seen that CO_2 can adsorb electrons on the surface of some catalysts, causing a transformation of semiconductor indium from n-type to p-type. At the same time, CO_2 can adsorb surface electrons to form a hole accumulation layer, which can repel protons in the electrolyte [81]. This plays a decisive role in preventing the HER from occurring on the surface of $In(OH)_3$-S, which is one of the advantages of this catalyst. Fig. 7e shows that, compared with $In(OH)_3$-S, $In(OH)_3$-M seems to be able to absorb more CO_2. However, its ability to inhibit the HER is lower than that of $In(OH)_3$-S (Fig. 7c), indicating that enhanced CO_2 adsorption is sometimes not the best strategy to inhibit the HER. It can also be seen that enhanced adsorption of CO_2 does not necessarily promote the CO_2RR since no CO production was detected in either reaction system. The absence of CO generation in the reaction system may be related to the strong adsorption of $*NO_2$ on the catalyst because the conversion of NO_3^- to $*NO_2$ on the surface of the $In(OH)_3$ series catalysts is a thermodynamic and spontaneous process with adsorption energies of − 2.48 eV(S) and − 0.52 eV(M), while the adsorption energy for CO_2 is + 0.38 eV; these results can be explained by the fact that $*NO_2$ on both indium catalysts adsorbed heavily, preventing the CO_2RR, and the difference between these two spontaneous processes determined the efficiency of subsequent catalytic C-N coupling for both catalysts. The band relationship between the (100) and (110) crystal planes of $In(OH)_3$-M is shown in Fig. 7f. During the catalytic process, electrons are transferred from (110) to (100), which means that electrons and holes in the (100) crystal plane will combine; thus, the ability to inhibit the HER is weakened, which is also consistent with the experimental results shown in Fig. 7c.

In addition to metal elements, nonmetallic elements can also play a catalytic role in the catalytic coreduction of CO_2 and NO_3^- [31]. For example, fluorine-doped carbon nanotubes (F-CNT-300) can enhance the adsorption of $*CO$ and $*NH_2$ and promote C-N coupling. Due to the electronegativity of F, a charge shift occurred in the original CNT structure, resulting in defects and the formation of active sites [31]. Fig. 7g shows that F was successfully combined into the carbon skeleton, and the F dopant mainly existed in the form of $C-F_2$. The highest current density recorded for F-CNT-300 from a CO_2-saturated 0.1 mol L^{-1} KNO_3 solution indicated that CO_2 and NO_3^- reactants were essential for C-N coupling (Fig. 7h), and F-CNT-300 also exhibited strong CO_2 chemisorption properties. As shown in Fig. 7i, DFT calculations showed that this charge transfer mechanism was conducive to promoting the respective reduction of $*CO$ and NO_3^- and the coupling reaction between $*CO$ and $*NH_2$, thus further reducing the energy barrier of urea synthesis. Notably, the reactive nitrogen species and reaction conditions also affect the urea yield. As shown in Fig. 7j, the yields of urea obtained by varying the ratio of different nitrogen species on a carbon substrate were also shown to be different [82]. In addition, unlike F-CNT, urea synthesis under this reaction system originated from the coupling of $*NO$ and $*CO$ to generate the key intermediate $*OCNO$ (Fig. 7k). Importantly, this study performed a series of optimizations in terms of increasing the activity of nitrogen species, demonstrating the importance of both reaction (CO_2RR and NO_3RR) activities during urea

synthesis using N-C-1000 (Fig. 7l), which was moderately active toward both of them, providing new insights into catalyst design and reaction mechanisms.

For a single metal active site, the HER inhibition performance of p-block metals generally exceeds that of d-block metals under the optimal reaction conditions corresponding to different catalysts. In addition to the modulation strategy, this HER inhibition performance seems to be related to the poor adsorption of H by the p-block elements and their semiconducting properties. Notably, nonmetallic element-based catalysts have shown catalytic capabilities beyond those of some metal catalysts, and nonmetals have advantages over metals in terms of both economic factors and physicochemical properties, which will provide a new approach to design and utilize nonmetallic-based materials for electrocatalytic C-N coupling synthesis of carbon and nitrogen organics.

In addition, the combination of p- and d-block metals is also a new approach. In a series of Fe^{II}-Fe^{III}OOH@BiVO$_4$-n (n = 1, 2, 3 and 5, representing the molar ratio of Fe^{II}-Fe^{III}OOH@BiVO$_4$) heterostructures constructed by solvothermal synthesis, BiVO$_4$ and FeOOH are the active sites for the CO$_2$RR and NO$_3$RR, respectively, and the coupling of *CO and *NO is mainly achieved on Fe^{II}-Fe^{III}OOH@BiVO$_4$-2 heterostructures [83]. Notably, the formation of such n-n type heterojunctions has excellent potential to improve interfacial charge migration. This combination can simultaneously improve electron transport at the active site while promoting NO$_3$RR, CO$_2$RR, and C-N coupling (Fig. 7m and n). The C-N coupling process is a two-step coupling pathway (*CO+*NO→*ONCO; *ONCO+*NO→*ONCONO). Although BiVO$_4$ can boost the CO$_2$RR, the product CO in the catalytic reaction system of Fe^{II}-Fe^{III}OOH@BiVO$_4$-2 shows a low FE, with the main byproduct being *NH$_3$ and only 11.5% FE for urea. In addition to the combination of metals, metals and nonmetals can also be connected. Carbon and indium are nonmetallic and metallic elements of the p-block elements, respectively. The use of graphene as a carrier provides better dispersion of In$_2$O$_3$, inducing more active sites to be exposed [84]. Although indium is a p-block element, In$_2$O$_3$ is more favorable for catalyzing NO$_2^-$ formation than In(OH)$_3$-S. In addition to indium-based catalysts, in situ-grown phthalocyanine-based covalent organic frameworks (CoPc-COF@TiO$_2$ NTs) on multilayered TiO$_2$ nanotubes showed effective synergistic catalytic effects, with an FE$_{urea}$ of 49% at − 0.6 V vs. RHE [85]. The CoPc and TiO$_2$ NTs on the CoPc-COF@TiO$_2$ NTs were the sites for the formation of *CO and *NH$_2$ intermediates, respectively. Notably, the coupling reaction of *CO with *NH$_2$ on CoPc was thermodynamically spontaneous with lower energy values than those for CO desorption from CoPc and the transformation of *NH$_2$ to *NH$_3$ on TiO$_2$(101), suggesting that C-N bonds were favorably formed on CoPc, which indirectly suggests that designing a dual-site seems to be an effective promotion of the C-N coupling strategy. In this way, regardless of the type of element, modulation or modification of the active site may cause changes in the core C-N coupling pathway, and thus, a rational modulation strategy is necessary.

3.2. Regulation of the metal coordination environment

Although nonmetallic elements in the p-block have been shown to catalyze the coupled CO$_2$RR and NO$_3$RR, this direction still needs to be further explored. Generally, catalyst modulation is focused on metal elements. Inspired by various strategies for the regulation of the coordination environment of d-block metal catalysts in the CO$_2$RR, the current design of the metal coordination environment for the coupling of the CO$_2$RR and NO$_3$RR can be divided into two shells. The first shell is the design of the coordination environment, which mainly includes the regulation of the coordination number and the design of the diatomic structure; the second shell is the use of oxygen vacancies to regulate the adsorbate and the energy barrier of the C-N coupling reaction.
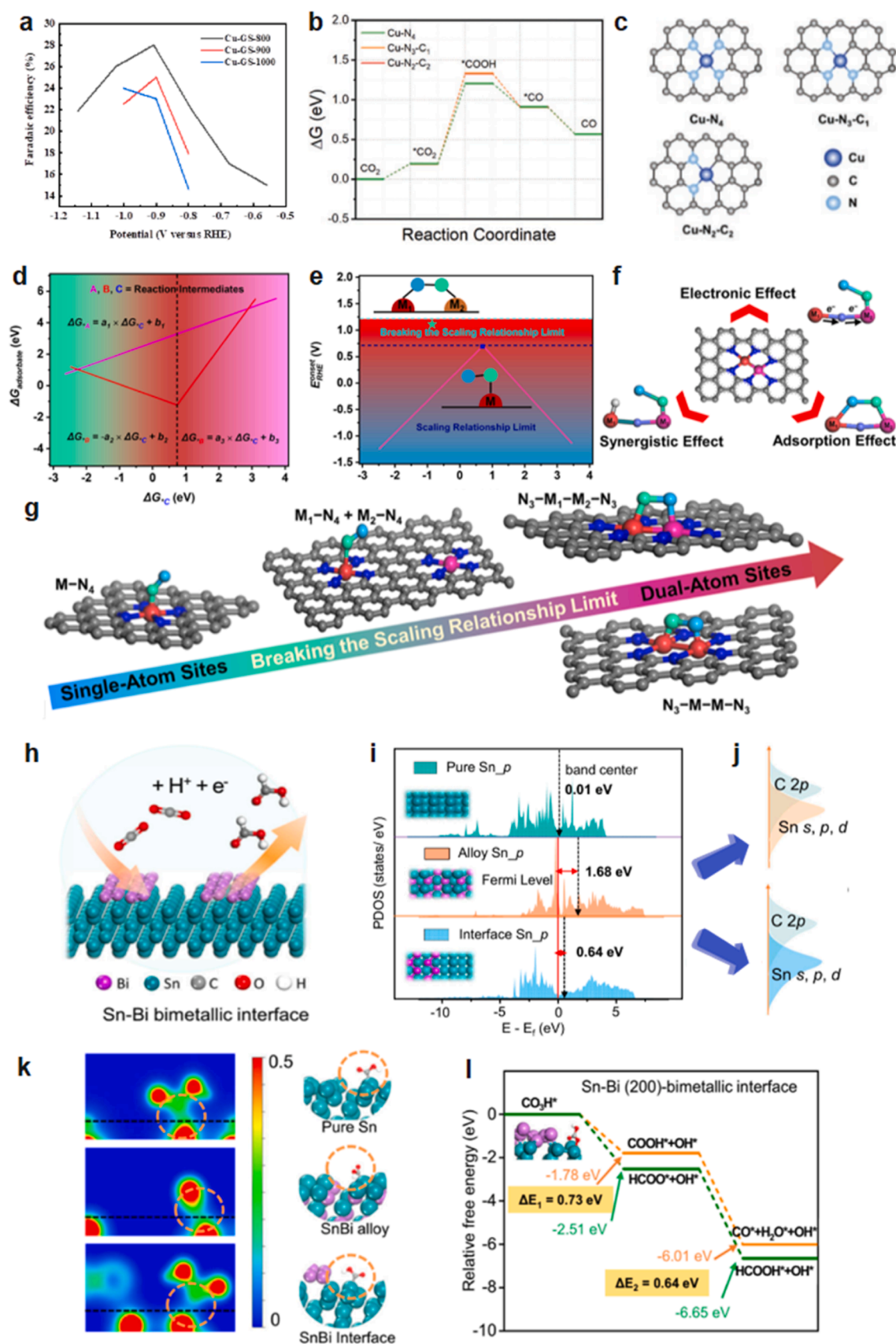
3.2.1. Metal atomic coordination design

In the field of CO$_2$RR, the design of catalyst atomic coordination is mainly focused on coordination for single-atom catalysts (SACs) [86, 87]. SACs have proven to have great potential in the field of electrocatalysis due to their excellent properties, and the atomically separated metal immobilized on the carrier is treated as a catalytically active site due to the empty/partially filled d orbitals of the metal (as mentioned for the copper single atom in Fig. 4a). To date, transition metal monatomic catalysts (M-N-C) anchored to carbon supports by N doping have been used for the CO$_2$RR and the NO$_3$RR [88–92]. M-N-C can catalyze C-N coupling efficiently only if it has a strong binding ability with intermediates. Although Ni-N-C has been proven to catalyze the CO$_2$RR synthesis of CO efficiently at the present stage, superior to Cu-N-C, a single Cu atom shows excellent performance in the synthesis of NH$_4^+$ by NO$_3$RR [93]. For example, copper atoms embedded in nitrogen-doped carbon nanosheets can efficiently reduce nitrate to NH$_4^+$, thus reducing the generation of nitrite [94]. How single copper atoms efficiently catalyze the electrochemical coupling of the CO$_2$RR and NO$_3$RR can be adjusted by changing the coordination number of the surrounding atoms of the central atom, which belongs to the first layer of central atom regulation in the field of M-N-C regulation [95]. Cu atom-doped graphene-like catalysts (Cu-GS) prepared by pyrolysis showed that some Cu-N$_4$ sites were converted to Cu-N$_{4−x}$-C$_x$ sites with increasing pyrolysis temperature (800–1000 °C), while Cu-N$_4$ sites were shown to be efficient catalytic sites by controlled experiments [38]. Fig. 8a shows a relatively high Faraday efficiency compared with that of Cu-GS-900, which is mainly attributed to the difference in copper coordination number. The coordination number of a single copper atom affects only the energy barrier that the C-N coupling needs to overcome and has no effect on HER inhibition. In the CO$_2$RR, the formation of *CO$_2$ is generally considered the RDS, but in this system, the formation of *COOH is considered the RDS [13]. Cu-N$_4$ in this reaction system showed a lower energy barrier for the formation of *COOH (Fig. 8b and c).

Similar to Cu$_2$O-ZnO, although Cu-N$_4$ has shown a high urea synthesis rate and excellent efficiency in inhibiting CO generation, the ammonia byproduct of this catalytic system is very high, resulting in a low Faraday efficiency of urea, which is mainly due to the high catalytic performance of copper itself in the NO$_3$RR synthesis of NH$_4^+$ [94,96]. However, it is worth noting that the concentration of NO$_3^-$ also leads to a high yield of NH$_3$ and decreases the Faraday efficiency of urea synthesis. Therefore, additional attention should be given to the concentration ratio of HCO$_3^-$ and NO$_3^-$ in the electrolyte in future studies [97].

Despite their superior performance in the field of catalysis, SACs have encountered considerable challenges in more complex catalytic reactions involving a variety of reactants and intermediates or free
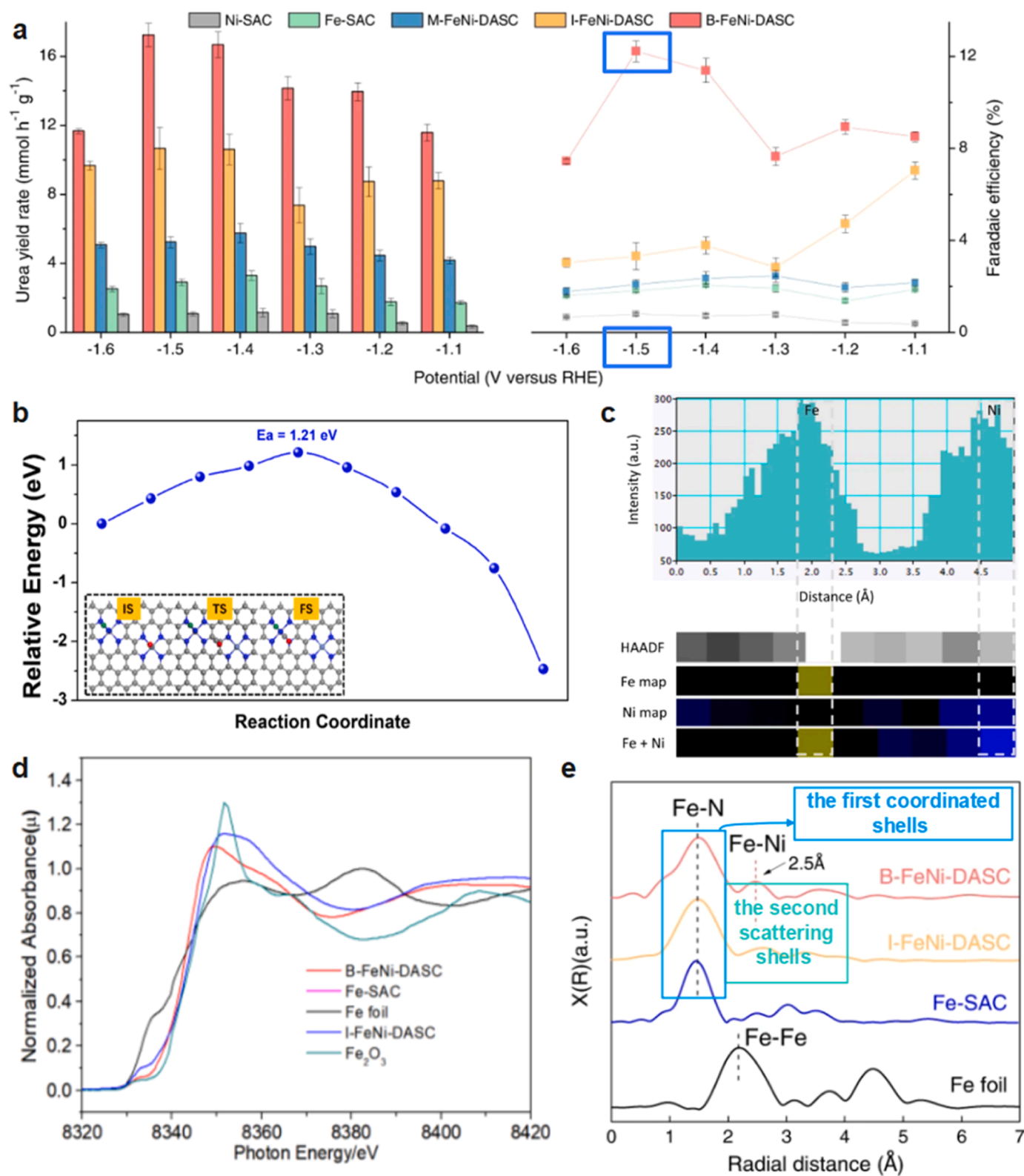
(caption on next page)

Fig. 8. Regulation of the coordination structure of the active center. (a) Comparison of C-N coupling properties of different copper single atom catalysis; (b) Comparison of energy barriers of CO_2RR catalyzed by different copper single atoms; (c) Graphical representations of modeled Cu-N-C sites [38]. Copyright 2022 John Wiley and Sons. (d) Linear relationships among the adsorption free energy of intermediates for SACs; (e) Diagram of breaking the scaling relationship limit: from SACs to DACs; (f) Advantages of DACs, including electronic effect, synergistic effect, and adsorption effect; (g) Adsorption forms of intermediates in SACs and DACs [64]. Copyright 2022 American Chemical Society. (h) Scheme of CO_2RR on Sn–Bi bimetallic interface; (i) PDOS of Sn 5p orbitals of pure Sn, alloy Sn, and interface Sn and weighted band center for all three models without adsorbate (overall range); (j) Schematic illustration for PDOS overlapping areas of Sn s, p, and d orbitals on Sn–Bi alloy and Sn–Bi bimetallic interface with C 2p orbitals of *COOH, respectively; (k) Calculated volume slices of calculated charge densities and corresponding optimized configurations for the three models with *COOH adsorbate, where the black dashed lines indicate the positions of the metal surfaces; (l) Gibbs free energy profiles of CO and HCOOH production pathways on Sn–Bi bimetallic interface [109]. Copyright 2022 Springer Nature.

radicals [64]. Generally, under optimal conditions, a single atomic site cannot guarantee the adsorption and activation of all intermediates [98]. Thus, a multi-intermediate reaction path on the SAC will result in a strength relation limit (SRL) [99]. For example, in the process of oxygen reduction (ORR), it is assumed that there are three intermediates A, B, and C, and the adsorption-free energies of these three intermediates (ΔG_{*A}, ΔG_{*B}, ΔG_{*C}) have some linear relationship (Fig. 8d). The value of ΔG_{*C} determines the performance of the multistage reaction, while SRL limits the multistep reaction occurring on the SAC [100]. In recent years, diatomic catalysts (DACs) have been shown to have higher catalytic performance than homologous SACs [52]. DACs can ideally inherit the advantages of SAC, and in some cases, the intermediates in the reaction process can be simultaneously adsorbed to bimetallic sites (DMS). That is, DACs provide additional adsorption sites compared to SACs, and this additional adsorption site can break the SRL (Fig. 8e). Therefore, the construction of DMSs is an effective strategy to overcome the inherent structural simplicity of active centers in SACs [101]. As shown in Fig. 8f and g, DMS configurations in DACs can be divided into three types at this stage, namely, two separated single metal sites (N_x-M_1 +N_x-M_2), two connected heavy metal sites (N_x-M-M-N_x), and two connected metal sites of different kinds (N_x-M_1-M_2-N_x), where N is a heteroatom (N, O, S, P) and M, M_1, and M_2 represent different metal centers [64]. The improved catalytic performance of DACs can be attributed to the optimization of the two metal centers by the interaction of short- and medium-range electrons in the two metal atoms [102]. In addition to their excellent results in the removal of organic pollutants, DACs are also widely used in the field of CO_2RR research [41,103–106]. In the field of CO_2RR research, the construction of diatomic interfaces has been developed at this stage to further improve catalytic performance. As shown in Fig. 8h, in the CO_2RR, the unique atomic combination of Sn and Bi (Sn-Bi bimetallic interface, not alloy) improves the catalytic performance of pure Sn metal to prepare formic acid from the CO_2RR. In this strategy, Bi is used to adjust the electron density of Sn. The addition of Bi causes the electronic state of Sn to move away from the Fermi level, indicating that Sn supplies electrons to Bi [107,108]. The P-band center of the Sn-Bi interface model is located between the p-band centers of pure Sn and the Sn-Bi alloy. *Sn-C in COOH adsorption and PDOS in HCOO* adsorption indicate more p-p and p-s overlap between C-2p and Sn-5 s and Sn-5p states on Sn-Bi alloys and in the Sn-Bi interface (Fig. 8i and j), which means that *COOH adsorption at the Sn-Bi interface is weak, which can be attributed to a decrease in Sn-C hybridization [109–111]. Furthermore, these findings can be explained by the fact that the addition of Bi promotes a moderate upward shift of the p-band center of Sn, reducing the electron density of Sn. Volume slices of the calculated charge density of the three models with *COOH (Fig. 8k) demonstrate this phenomenon. Therefore, the bimetallic Sn-Bi interface inhibits the formation of the CO byproduct by weakening the adsorption of *COOH. In addition, the most active Sn-Bi interface location for HCOOH formation provides suitable HCOO* adsorption, implying enhanced Sn-O hybridization, which is beneficial for formic acid formation (Fig. 8l).

For the electrocatalytic reduction of CO_2 and NO_3, C-N coupling is critical, so in addition to suppressing the HER, reducing the reaction energy barrier of C-N coupling can be considered a challenge today. Currently, a new strategy is to construct a "triad" of active, activation, and coupling sites by adjusting atomic coordination and coordination structures. This strategy can be realized by constructing bimetallic

active sites, such as iron-nickel bimetallic bonding, which can effectively catalyze C-N coupling to generate urea [23]. As shown in Fig. 9a, traditional iron or nickel monatomic catalysts only have high selectivity for NH_3 and CO, while their selectivity for urea is very low or even negligible. Compared with the two monatomic catalysts mentioned above, the isolated diatomic Fe-Ni electrocatalyst (I-FeNi-DASC) overcomes the limitation of unilateral selective adsorption and activation of carbon or nitrogen reactants and can improve the catalytic performance, which is mainly attributed to the synergistic effect [112]. This synergistic effect significantly improves the electrochemical synthesis of urea by realizing synergistic adsorption and activation of multiple reactants. The isolated $Fe-N_4$ and $Ni-N_4$ sites in the I-FeNi-DASC generate many activated C- and N-based intermediate species and increase the likelihood of these intermediate species coming into contact and coupling, thus providing the basis for the generation of key C-N bonds [23]. However, it is not enough to have abundant reaction intermediates because the efficiency of the catalytic synthesis of urea by the I-FeNi-DASC is not significantly higher than that of Fe-SAC, indicating that the catalyst is not particularly effective in catalyzing the C-N coupling reaction. This is demonstrated by the presence of distances (TM-N_4) between $Fe-N_4$ and $Ni-N_4$ isolated bimetallic sites. As shown in Fig. 9b, the presence of TM-N_4 resulted in a kinetic reaction energy barrier of + 1.21 eV for C-N coupling, which inhibited C-N coupling under ambient conditions. Therefore, a strategy to preserve the synergistic effect in the I-FeNi-DASC while enhancing the kinetics of the catalytic CO_2 coupling of the NO_3RR, thus providing the active site for C-N coupling, is needed. Thus, researchers proposed a bonded Fe-Ni diatomic configuration. The presence of Fe-Ni coordination in the bonded Fe-Ni diatomic electrocatalyst (B-FeNi-DASC) was confirmed by electron energy-loss spectroscopy (EELS) (Fig. 9c). The X-ray absorption near edge structure (XANES) results further revealed the reduced valence of Fe in the I-FeNi-DASC, indicating that the Fe coordination environment is regulated (Fig. 9d) [23,113]. Fourier transform extended X-ray absorption fine structure (FT-EXAFS) was performed to analyze the changes in the Fe coordination environment, as shown in Fig. 9e. First, in the first coordination shell (1–2 Å), the sizes of scattered peaks from the Fe-N and Ni-N paths in the first shell were nearly the same at approximately 1.5 Å, indicating that the coordination environments of Fe and Ni atoms were almost identical in the B-FeNi-DASC catalyst. However, in the second shell (2–3.5 Å), a broad peak was observed at 2.5 Å. The scattering path was attributed to the formation of the Fe-Ni bond, in which Fe is coordinated to Ni in addition to the 3 N site. In contrast, the Fe-Ni bond was not observed in the I-FeNNi-DASC, indicating that the Fe-Ni bond was not present in the I-FeNi-DASC. On the other hand, compared with Fe-SAC and Ni-SAC, the first-shell scattering (Fe-N and Ni-N) of B-FeNi-DASC showed asymmetry and a slightly reduced intensity, indicating that the chemical state of Fe was changed by coupled Ni atoms, which confirmed that Ni was an important factor in changing/regulating the coordination environment of Fe atoms. In conclusion, a Fe-Ni diatomic bond structure was formed in the B-FeNi-DASC catalyst, and Fe-Ni-N_6 proved to be the active unit structure.

Similar to the Lewis acid sites (unoccupied empty orbitals) in the N_2RR, in FeNi-N_6, the electron-deficient Fe sites formed Lewis acid sites due to charge transfer, which enhanced the adsorption and activation of *NO, while in I-FeNi-DASC, the electrons were all concentrated on Ni-N_4

Fig. 9. C-N coupling is catalyzed by diatomic isolation and diatomic bonding. (a) Urea yield rates and corresponding Faradaic efficiencies on Ni-SAC, Fe-SAC, M-FeNi-DASC, I-FeNi DASC, and B-FeNi-DASC at various applied potentials; (b) The kinetic energy barrier of *CO+ *NH coupling on FeN$_4$-NiN$_4$, where the insert frame included the optimized structures of initial state, transition state and finial state along the reaction pathway; (c) Acquired HAADF-STEM image intensity profile accompanied by atomic-resolution EELS mapping of the Fe–Ni bond; (d) X-ray absorption near edge structures of Fe K edges of Fe-SAC, I-FeNi-DASC, and B-FeNi-DASC (XANES); (e) Fourier transform extended X-ray absorption fine structure (FT-EXAFS) spectra of Fe-SAC, I-FeNi-DASC, and B-FeNi-DASC [23]. Copyright 2022 Springer Nature.

and Fe-N$_4$, indicating that the bonded Fe-Ni optimized the adsorption and activation of the intermediates. Operando SR-FTIR measurements further confirmed the combined coactivation and PCET process of *NO and the occurrence of C-N coupling, as shown in Fig. 10a. The spectral bands in the presence of N $=$ O and C$=$O demonstrated the coactivation of NO$_3$ and CO$_2$, which fulfilled the purpose of preserving the synergistic effect in the I-FeNi-DASC [114]. Furthermore, the infrared band of N-H demonstrates a further PCET process of *NO on the B-FeNi-DASC [115]. More importantly, the *NHCO band was detected and this band increased with the negative potential (-1.6 to -1.1 V), reaching a maximum at -1.5 V, which coincided with the test results of Fig. 10a, implying that *NHCO was associated with the formation of urea [116]. It was concluded that Fe-Ni-N$_6$ is a triple site of activity, activation, and coupling. The reaction mechanism of this process was revealed by DFT theory calculations. C-N coupling was divided into two steps. In the first step, the C-N coupled carbon source and nitrogen source were *CO and *NH, respectively, and *NH was activated by *NO. Thermodynamically spontaneous and kinetically feasible coupling ($+0.21$ eV) between *NH and adjacent *CO was observed at the bonded Fe-Ni site and released the Ni center (the first C-N coupling), as shown in Fig. 10b, which had much lower energy than the energy barrier ($+1.21$ eV) obtained at the FeN$_4$-NiN$_4$ counterpart. This result may be related to the lower adsorption of NO$_3$ by FeN$_4$-NiN$_4$ than by FeNi-N$_6$. Subsequently, the released new Ni center adsorbed a second *NO, *NO and *NHCO underwent a second coupling to generate the key intermediate *NHCONO, and finally, urea was produced by the PCET process, which only needed to overcome a very low $+0.09$ eV reaction energy barrier (Fig. 10c). The reaction mechanism is shown in Fig. 2. In summary, urea synthesis on B-FeNi-DASC resulted from the coupling of *NH and *CO to form the first C-N bond and the subsequent C-N coupling between *NHCO and *NO to form the second C-N bond, both thermodynamically spontaneous and highly dynamically feasible. Two C-N couplings at the bonded Fe-Ni site were required to overcome only the lower energy barriers ($+0.21$ eV and $+0.09$ eV), all due to the formation of the Fe-Ni bond. Interestingly, when NO$_3$ was replaced with nitrite, the catalytic performance was only slightly decreased (the Faraday efficiency of urea was reduced by less than 1%), which indicated that the B-FeNi-DASC catalyst could effectively catalyze the NO$_3$RR.

Notably, another advantage of dual active sites is that they can significantly inhibit the HER response. As shown in Fig. 4b, the dual-active site catalysts, B-FeNi-DASC and Fe(a)@C-Fe$_3$O$_4$, produce negligible H$_2$ in the electrocatalytic coupling of CO$_2$RR and NO$_3$RR reduction, where the HER is completely inhibited at B-FeNi-DASC. However, the B-FeNi-DASC did not strongly inhibit CO, which may be related to the fact that the excessive CO$_2$RR process was not inhibited. From previous studies, it can be seen that the inhibition of the CO$_2$ to CO process is mainly by adsorption of NO$_3$ to promote the NO$_3$RR and thus C-N coupling rather than lowering the energy barrier of C-N coupling to promote C-N coupling as in the Fe-Ni bond. Therefore, subsequent studies can focus on exposing the N-terminus by realizing adsorption on the O-terminus to achieve the construction of a two-site efficient catalytic CO$_2$RR coupling NO$_3$RR.

Regarding the inhibition of excess CO$_2$RR or NO$_3$RR by dual monometallic atomic catalysts, synergistic effects between asymmetric sites can be exploited to reduce coupling barriers to facilitate C-N coupling. For example, CoRuN$_6$, prepared by anchoring Ru and Co atoms on nitrogen-doped carbon, successfully suppressed the CO$_2$RR and NO$_3$RR, and the FE$_{urea}$ was enhanced to 25.31% (Fig. 11a) [117]. The C-N coupling pathway induced by CoRuN$_6$ is also different from that of the B-FeNi-DASC. As shown in Fig. 11b and c, although the coupling process still proceeds in two steps, it shows an early binding of *CO$_2$ and *NO$_2$ that differs from the Fe-Ni bond. The key to the active site Ru/Co design was to utilize the difference in selectivity of the two metals for carbon and nitrogen intermediates to establish asymmetric adsorption of the intermediates. This dual monoatomic site-induced asymmetric conformation can inhibit competitive reactions and lower the reaction energy
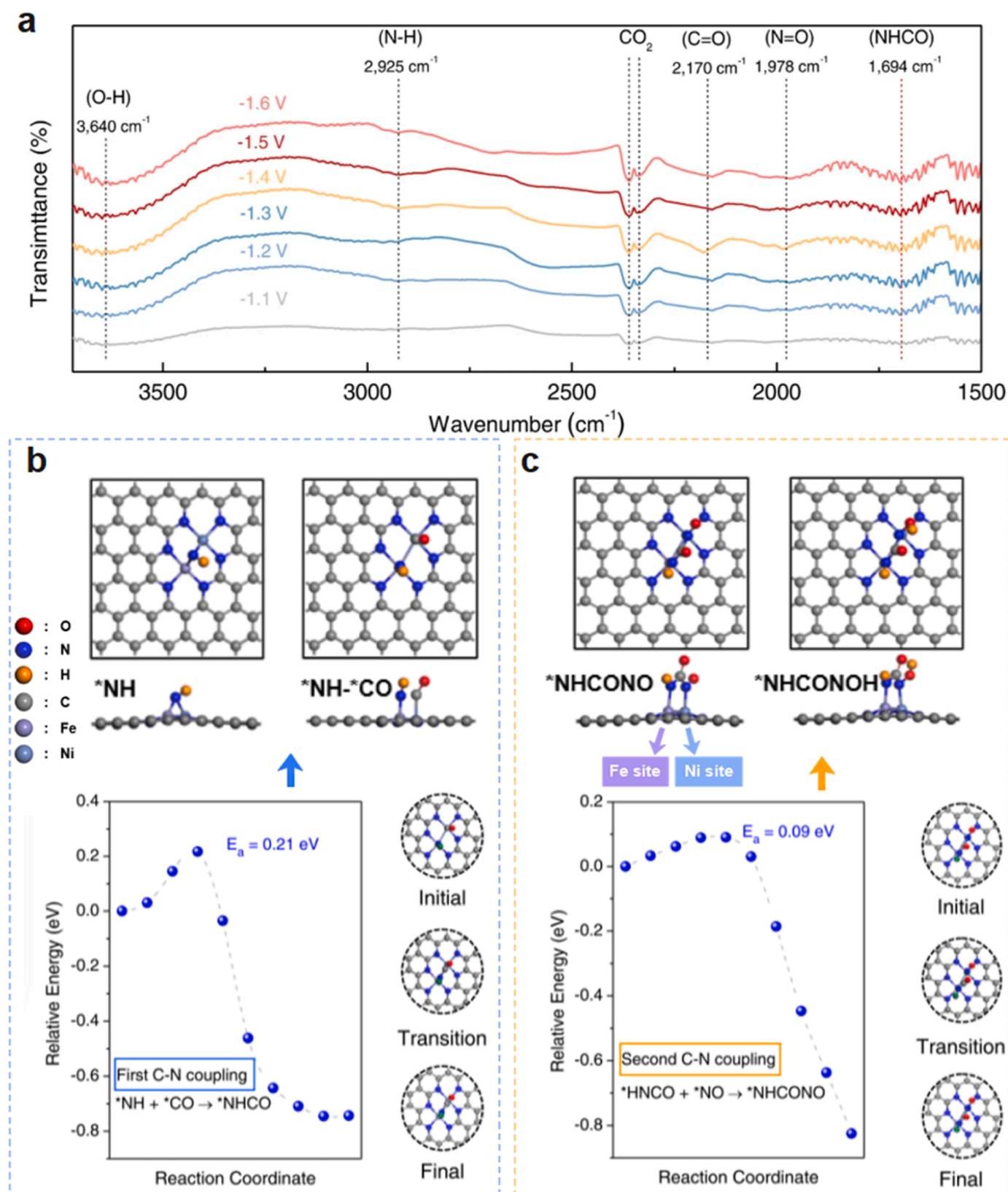
barrier, improving the selectivity of urea [118]. Thus, it appears that spatial modulation can also be exploited in the design of dual single metal-atom catalysts.

In addition, the construction of alloy-phase bilocations is also feasible [119]. As shown in Fig. 11d, in the synthesis of PdCu alloy nanoparticles anchored on carbonized bacterial cellulose (PdCu/CBC), it was found that the d-band center value of Cu atoms shifted upward from -2.313 eV to -1.528 eV after the formation of PdCu alloys due to an increase in the position of the d-band center regulated by the electron distribution caused by charge transfer [120]. This implied that the PdCu nanoalloys could provide more d-bands for the adsorbate compared to single Pd or Cu, facilitating strong adsorption and activation of CO$_2$ and NO$_3$ and efficiently promoting the C-N coupling reaction (Fig. 11e), which was the intrinsic reason for the high FE$_{urea}$. Notably, on the PdCu (111) active site, early carbon and nitrogen coupling (*CO$_2$ $+$*NO$_2$) occurred, with the overall reduction pathway shown in Fig. 2. At this active site, subsequent hydrogenation of *CO$_2$ was difficult, while the thermodynamic output from *NO$_2$ to *CO$_2$NO$_2$ was more favorable than the hydrogenation of *NO$_2$ to *HNO$_2$ and of *CO$_2$ to *COOH, which was essential for the efficient synthesis of urea. Similarly, the noble metals Ru, Pt, and Pd (Ru/Pt/Pd-Cu CF) immobilized on copper foam prepared by in situ deposition also showed good catalytic activity [121]. Among them, Ru-Cu CF showed the best performance with an FE$_{urea}$ of 25.4% at -0.3 V vs. Ag/AgCl. Similar to Cu SACs, the calculated free energies showed that the formation of *COOH intermediates was a rate-determining step. Cu(111)/Ru enabled a higher bonding ability of Ru sites, which lowered the energy barrier for *COOH formation. In addition, copper could also modulate the electronic structure of other metals. For example, the RhCu-uls nanospheres prepared by the ultrasonic-assisted hydrothermal method show much higher performance than the RhCu-none nanospheres prepared by the hydrothermal method. However, their FE$_{urea}$ was lower than that of PdCu alloys (34.82 ± 2.47% vs. 69.1 ± 3.8%), which seemed to indirectly show the potential of copper [122]. Thus, bonding noble metals to Cu may be an effective strategy to promote C-N coupling, but this still needs to be further explored.
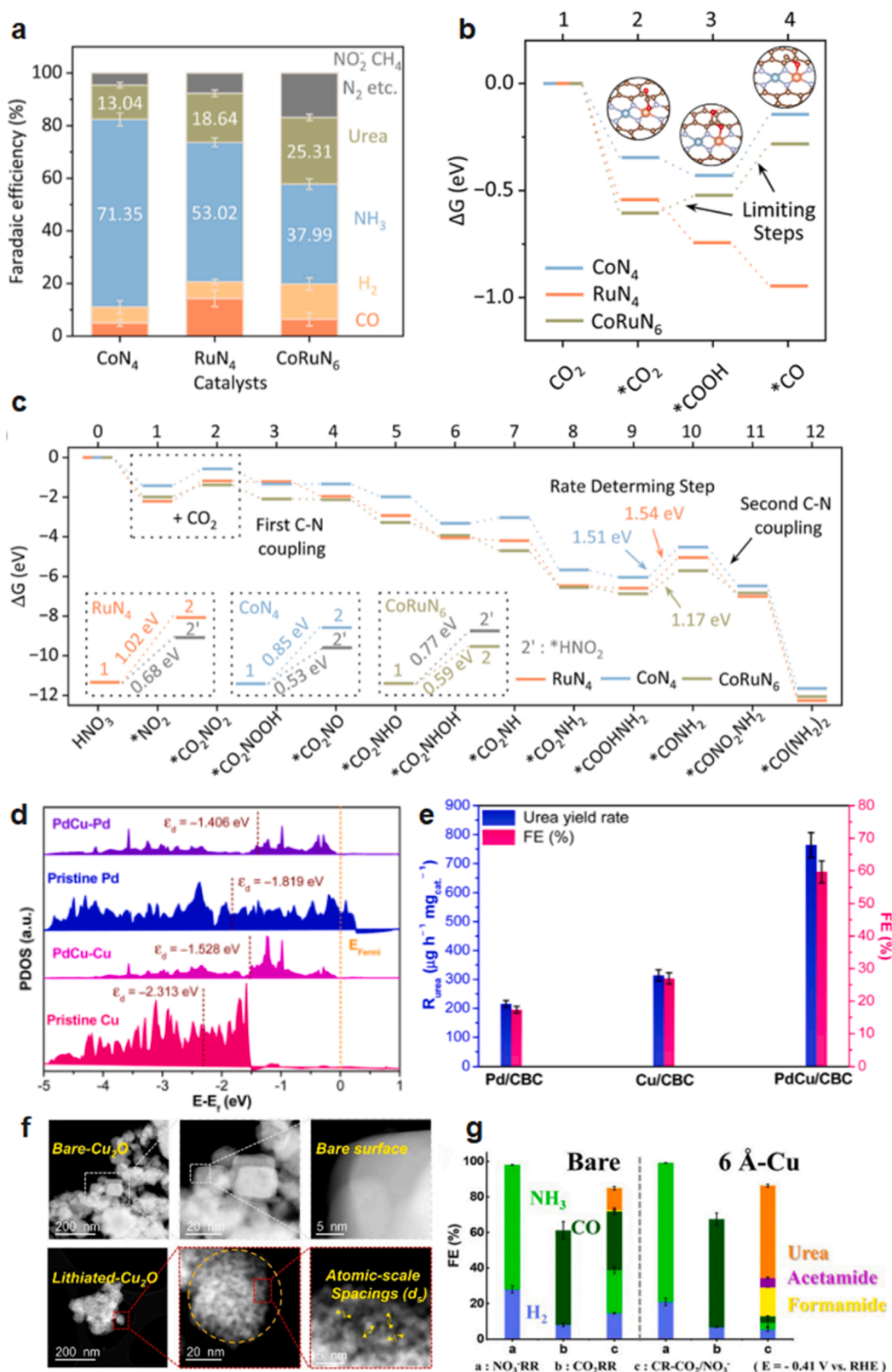
Similar to Ru/Co, the asymmetric coupling of *CO with *NO on Cu^0-Cu$^+$ in Cu$_2$O could increase the urea yield [123]. The asymmetric C-N coupling reaction occurred using neighboring copper sites with different electronic structures interacting with the two intermediates. *NO tended to be adsorbed at the Cu$^+$ site, while Cu$^+$ could promote the adsorption of *CO at the Cu^0 site. Thus, the asymmetric coupling of * CO and *NO was thermodynamically and kinetically rationally designed.

Due to the specific binding energy of copper-based materials for C- and N-intermediates, metallic copper also seems to have great potential to be exploited in the electrocatalytic coreduction of CO$_2$ and NO$_3$ [124]. Recently, a strategy to introduce atomic-scale defects or spacings (d_s) between two Cu$_2$O nanoparticles via the electrochemical lithiation approach was proposed, significantly improving urea's selectivity and yield in a flow cell electrode system with a gas diffusion electrode [124]. As shown in Fig. 11f, lithiation treatment of Cu$_2$O nanoparticles caused the splitting of the particles and generation of defects, as well as increased atomic spacing. Similar to other studies, this study also showed high selectivity for NH$_3$ in pure Cu catalysts due to the unique binding energy of copper toward nitrogen intermediates [38,40,125]. As shown in Fig. 11g, the catalyst exhibited high j_{urea} and high FE$_{urea}$ and remained stable for 50 h when the d_s value of lithiated Cu was 6. Furthermore, byproducts such as H$_2$, CO, and HCOOH were generated within the system. Notably, the high performance of 6 Å-Cu was not attributed to the catalyst morphology or specific surface area but rather to the d_s value between the Cu nanoparticles. The energy barrier for C-N coupling was at its lowest when $d_s = 6$, mainly due to the stability provided by the Cu surface through electron transfer at this value. In summary, in addition to constructing diatomic/dual active sites, strategies such as spatial effects, alloying, and atomic spacing can also be used to prepare catalysts for the electrocatalytic coreduction of CO$_2$ and

Fig. 10. Two-step C-N coupling process of N-intermediate and C-intermediate in Fe-Ni bond. The structure of the initial state, transition state, and final state and the formation of *NHCO and *NHCONO are also given. (a) Infrared signal in the range of 1500–3750 cm^{-1} under various potentials for B-FeNi-DASC during the electrocoupling of nitrate and CO_2; (b) The first C-N coupling reaction pathway formed by *NHCO and the adsorption of *NH and *CO on Fe-Ni bond; (c) The second C-N coupling formed by *NHCONO, and the iron, nickel, nitrogen, oxygen, and carbon atoms are represented by purple, indigo, blue, red and gray spheres, respectively [23]. Copyright 2022 Springer Nature.

Fig. 11. Spatial effects, alloying, and atomic spacing strategies. (a) Faradaic efficiencies distribution of all products for different catalysts at − 0.6 V vs. RHE; (b) Free-energy diagram for CO_2 reduction on $CoRuN_6$; (c) Free-energy diagram of different catalysts for urea production on $CoRuN_6$ [117]. Copyright 2023 Elsevier. (d) The projected density of states (PDOS) onto the Pd-4d or Cu-3d orbitals of the PdCu/CBC, pristine Pd, and pristine Cu, and the dashed line represents the d-band center of Pd or Cu atoms at 0 eV; (e) The urea yield rate and FE of the PdCu/CBC, Cu/CBC, and Pd/CBC at − 0.50 V vs. RHE for 2 h reaction [119]. Copyright 2023 Royal Society of Chemistry. (f) STEM images of bare Cu_2O and lithiated Cu_2O (atomic-scale spacings highlighted in an orange circle and yellow parallel lines with points); (g) The product analysis of NO_3^-RR, CO_2RR, and CR-CO_2/NO_3^- on bare and 6 Å-Cu at − 0.41 V vs. RHE [124]. Copyright 2023 The Royal Society of Chemistry.

NO_3^-. Moreover, in addition to the p-block metals, copper also seems to have a large scope for development in electrocatalytic C-N coupling due to its special properties.

3.2.2. Oxygen vacancy engineering

Oxygen vacancy engineering is considered an effective strategy for improving the catalytic behavior of electrocatalysts [126–128]. In the process of the CO_2RR, vacancies can effectively improve the electron capture ability, adjust the d-block metal element d orbital band structure, and reduce the reaction energy barrier [129]. In this process, in general, CO_2 adsorption or CO_2 being reduced to $*CO_2/*COOH$ is PDS [130,131]. In recent years, copper has been widely used to enhance the adsorption of CO_2, and some metal oxides have been regarded as potential vacancy carriers. For example, the CeO_2 oxygen vacancies in CeO_2 nanorods were replaced by Cu, promoting the selective electric reduction of CO_2 to $*CH$, and the catalytic center consisted of a single Cu site and a polyoxygen vacancy (Fig. 12a) [132]. A similar process occurs during the coreduction of CO_2 and NO_2. When the nitrogen source is nitrite, the key intermediates are $*CO$ and $*NH_2$, and the general reduction mechanism is shown in Fig. 12b [133]. Different from the CO_2RR process, in the electrochemical coupling of the CO_2RR and NO_3^-RR, oxygen vacancies reduce the energy barrier of C-N coupling by trapping the intermediate product. For example, hydroxylated indium oxide with oxygen vacancies (Vo-InOOH), as synthesized by the dissolution thermal method, had excellent electrocatalytic C-N coupling activity for the synthesis of urea, and Vo-InOOH exhibited excellent inhibition of the CO_2RR (CO_2 to CO) and the HER compared to InOOH and In(OH)3-S (Fig. 12c and d) [25]. Similar to In(OH)3-S, NO_3^- was spontaneously reduced to $*NO_2$ on the surface of Vo-InOOH, and $*NO_2$ covered a large area on the catalyst surface during the coreaction, which inhibited the CO_2RR to a large extent [25]. The ability of Vo-InOOH to inhibit the HER was also attributed to the conversion between CO_2-guided semiconductor n-p types. In an Ar atmosphere, both InOOH and Vo-InOOH had n-type properties, as shown in Fig. 12d. Vo endowed InOOH with more electrons on its surface. In the CO_2 atmosphere, the slope of the Mott−Schottky diagram of Vo-InOOH was higher, indicating a decrease in surface electrons, which was due to electron trapping by CO_2 [133]. Therefore, more electrons were transferred to the CO_2 adsorbed on the surface of Vo, resulting in the p-type property of InOOH as well, as shown in Fig. 12e. The inhibition of the HER was also attributed to the repulsion of protons in the electrolyte by the CO_2-induced hole accumulation layer. The superior ability of Vo-InOOH to inhibit the HER compared to In(OH)₃-S was attributed to the fact that Vo confers more surface electrons and CO_2 traps electrons to form a thicker hole accumulation layer, thus causing the repulsion of more protons and greater inhibition of the HER, which is the first effect of Vo [134]. Five consecutive electrocatalytic experiments and long-term CA experiments proved the stability of Vo-InOOH. The In1 atom, one of the two indium atoms adjacent to Vo (In1 and In2), was regarded as the active site. Similar to Pd/Cu, the early central C-N coupling process at this active site was the combination of $*CO_2$ and $*NO_2$ to form $*CO_2NO_2$ (+0.20 eV), which was subsequently protonated to $*CO_2NH_2$, and the conversion of $*CO_2NH_2$ to $*COOHNH_2$ was regarded as PDS (+1.04 eV). Finally, $*COOHNH_2$ was converted to urea by the PCET process (Fig. 2). As shown in Fig. 12f, the presence of Vo caused the positive charge of In1 to be reduced, suggesting that Vo plays a major role in regulating the electronic structure around indium atoms in addition to inducing electron transfer, which is the second effect of Vo. At the same time, the O atom in $*CO_2NH_2$ acted as a Lewis base, and the bonding states of In1 increased while the antibonding states decreased; In2 showed the opposite trend, indicating that the interaction between In1 and $*CO_2NH_2$ was weakened [135]. Thus, the introduction of Vo caused the electrons around indium near Vo to be reconfigured. Although the active site was an indium atom, Vo played an essential role in regulating the electronic structure of the indium active site. In addition, as shown in Fig. 12g, this regulated electronic structure led to cleavage of the In1-O
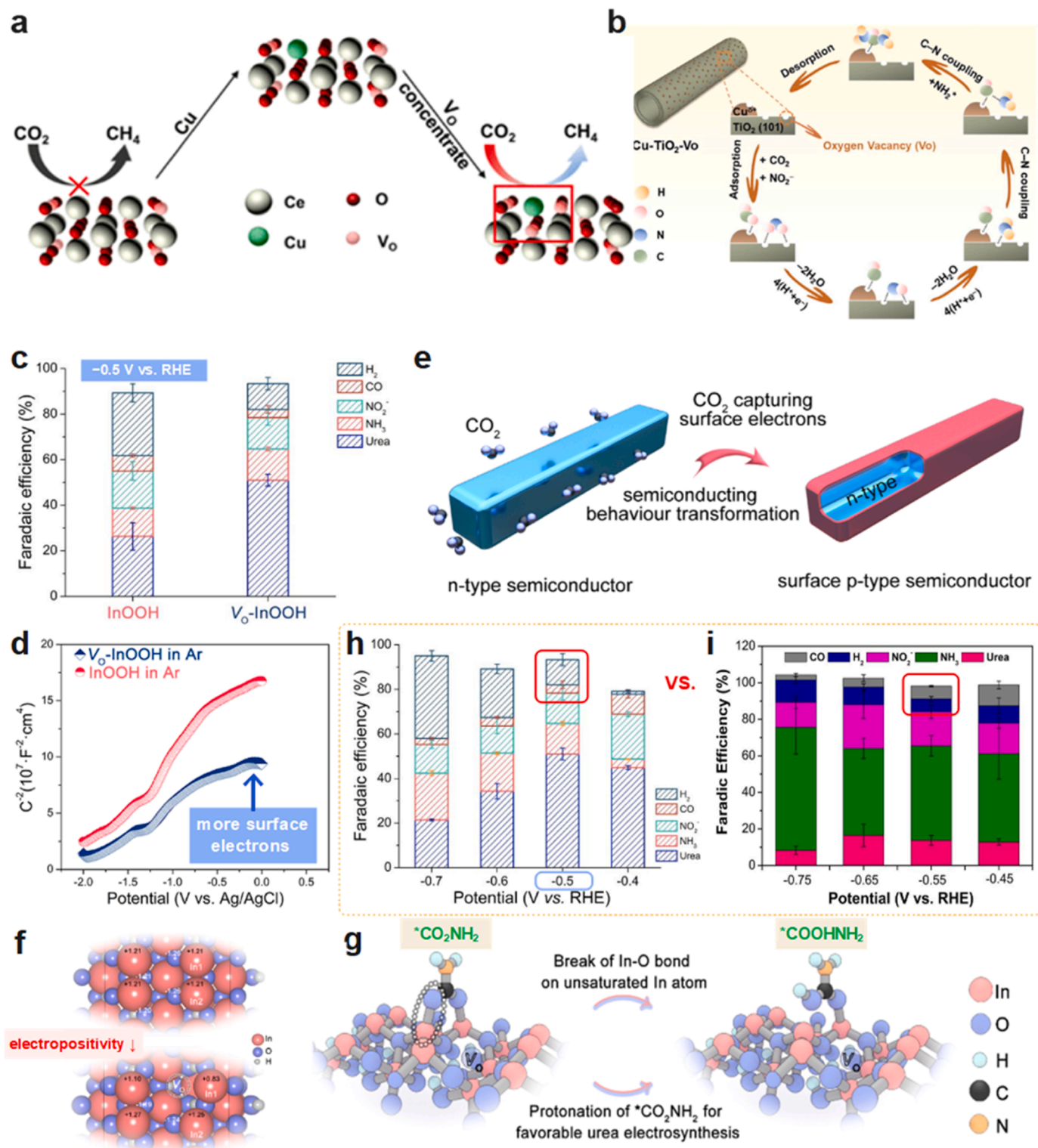
bond formed by the oxygen atom from $*CO_2NH_2$ and In1, which promoted the protonation of $*CO_2NH_2$ and thus reduced the energy barrier of $*CO_2NH_2$ to $*COOHNH_2$, which was also the fundamental reason behind the high catalytic activity of this catalyst.

Overall, the ability of oxygen vacancy engineering to inhibit the HER is higher than that of the crystal plane modulation strategy. Another advantage of Vo-InOOH compared to the previous In(OH)3-S is its ability to further reduce the reaction energy barrier for $*CO_2$ and $*NO_2$ coupling (0.35 eV vs. 0.25 eV). As seen in Fig. 12c, a small amount of CO was present in the Vo-InOOH-catalyzed coreduction of CO_2 and NO_3^- system, while no CO was detected in the In(OH)₃-catalyzed system, considering that this is most likely related to the adsorption and transfer of electrons on the catalyst surface. Compared with In(OH)₃, excessive electron transfer from the Vo-InOOH surface to the CO_2 surface led to some enhancement of the CO_2RR performance, and thus, a small amount of CO was detected in the reaction system. However, it can also be seen that enhanced adsorption of electrons sometimes leads to the generation of byproducts.

Notably, however, although indium is affiliated with p-block metallic elements, its ability to inhibit hydrogen evolution is sometimes inferior to that of Fe-Ni-N₆ and Fe@C-Fe₃O₄/CNTs, and there are many byproducts (Fig. 12h and i). The inhibition of the HER on In(OH)₃-S regulated by the crystal plane structure is lower than that of Vo-InOOH, indicating the advantage of the second layer coordination environment regulation of the active center.
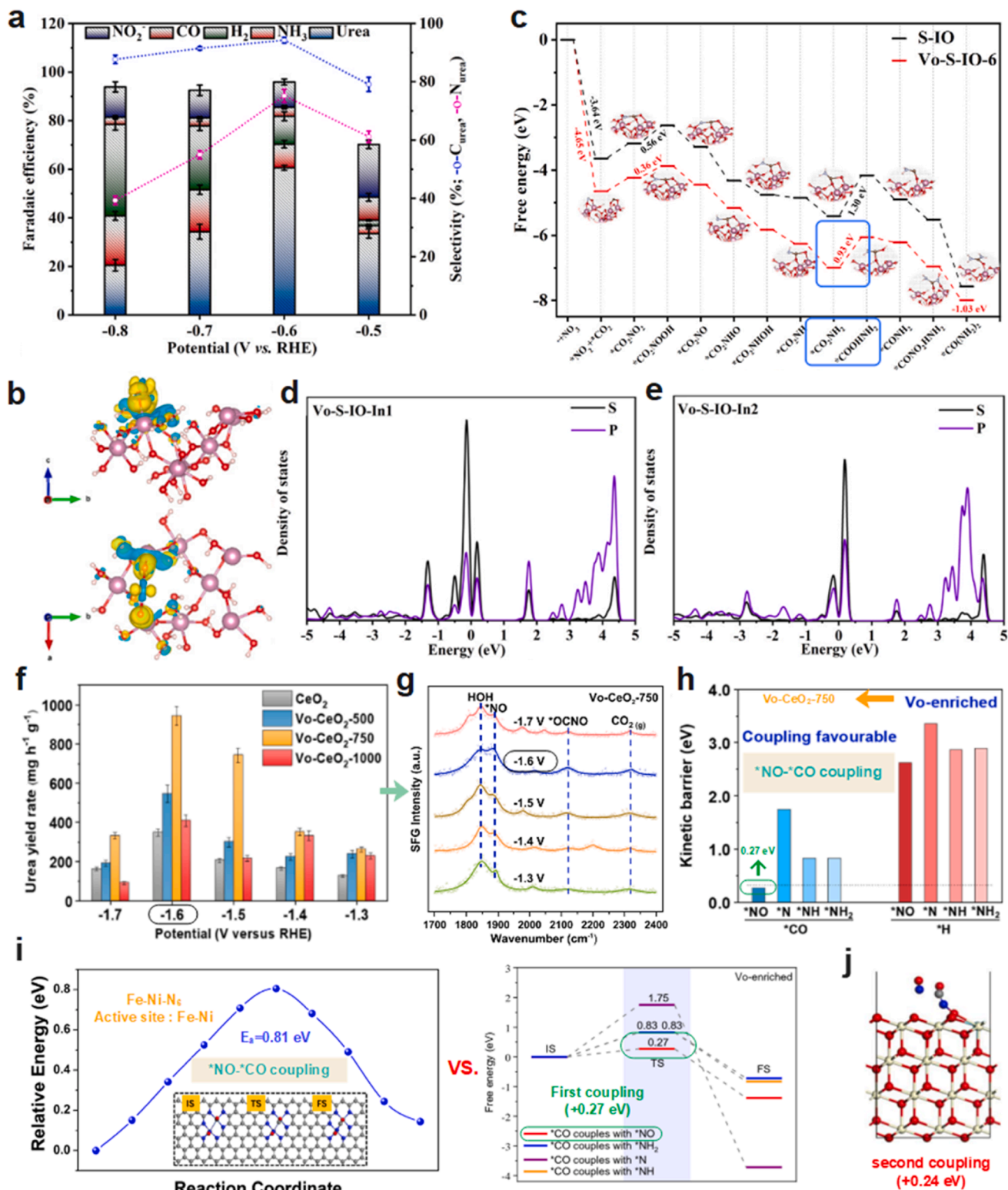
Although the other indium-based catalyst, graphene-In₂O₃, which had almost no oxygen vacancies, was more effective for the inhibition of HER, a large amount of nitrogen byproducts were generated within the reaction system, with the highest FE of NO_2, indicating that it was not as good as the other two indium-based catalysts for the adsorption of $*NO_2$ [84]. While HER is an issue that needs to be addressed, there is also a need to balance the selectivity of the target product. The efficiency of an electrocatalyst can be tuned by the active site and the local electronic structure. In(OH)₃-S provided a platform for efficient C-N coupling by designing a specific facet, and Vo could improve the intrinsic activity of the catalyst by adjusting the electronic structure. Thus, combining the advantages of facets and Vo, an efficient Vo-rich indium hydroxide nanocube catalyst (denoted as Vo-S-IO) with (100) facets was designed [136]. The catalyst achieved a high Faraday efficiency of 60.6% at − 0.6 V vs. RHE (Fig. 13a), which could be attributed to the enhanced adsorption of $*NO_2$ on the oxygen-rich vacancy of the (100) facet. In addition, the formation of Vo not only enhanced the adsorption of CO_2 but also weakened the NO_3^-RR and CO_2RR on the (100) facet (FE_{CO} < 5%), but excessive Vo content reduced the activity. Although the d-block metal-based catalyst RuCoN₆ inhibits the CO_2RR and NO_3^-RR, it appears to be less effective than the indium-based catalyst based on experimental results, which is likely related to the choice of elemental species and catalyst morphology [117]. Notably, a larger negative potential generates excess $*H$, increasing coupling with other $*H$ or $*NO_2$, producing H_2 and NH_3 and reducing the selectivity of urea. As shown in Fig. 13b, similar to In(OH)₃, electrons from the two unsaturated In atoms on the (100) facet could be transferred to $*NO_2$, promoting $*NO_2$ activation, which was also considered intrinsically active for C-N coupling. Meanwhile, CO_2 was activated by the formation of In-O-C-O-In on the (100) facet, promoting the transfer of electrons to $*CO_2$. In contrast to the C-N coupling on In(OH)₃, on the Vo-S-IO-6 surface, $*NO_2$ was coupled to $*CO_2$ by overcoming only very low free energy. At the (100) facet, $*CO_2NO_2$ was thermodynamically favored for urea production. Protonation of $*CO_2NO_2$ occurred at the In atom near the oxygen vacancy, and the presence of Vo favored the protonation of $*CO_2NO_2$. As shown in Fig. 13c, similar to In(OH)₃ and Vo-InOOH, the protonation process of $*CO_2NH_2$, which was considered a PDS, was a heat-absorbing process, but the energy barrier for this process occurring on the Vo-S-IO-6 surface was only + 0.93 eV. The density of states (DOS) of In atoms bound to O atoms in $*CO_2NO_2$ further explained the enhanced Vo effect. As shown in Fig. 13d and e, the O atom bound to the In1 atom in $*CO_2NH_2$ was

Fig. 12. Oxygen defect engineering. (a) Copper-doped CeO_2 improves the performance of CO_2RR [132]. Copyright 2018 American Chemical Society. (b) Possible reduction mechanism of urea synthesis by CO_2 and NO_2^- on Cu-TiO$_2$-Vo [133]. Copyright 2020 Elsevier. (c) FEs of all the products distribution for both the Vo-InOOH and InOOH at − 0.5 V vs. RHE; (d) Mott−Schottky measurements in Ar; (e) Schematic illustration of the n-p semiconductor type transformation process; (f) Bader charge analysis on Vo-InOOH and pristine InOOH; (g) Urea synthesis process on the surface of the Vo-InOOH catalyst; (h) FEs of all products distribution for Vo-InOOH at various potentials [25]. Copyright 2022 American Chemical Society. (i) All products distribution for Fe(a)@C-Fe$_3$O$_4$/CNTs during electrocatalytic urea synthesis at various potentials [68]. Copyright 2023 John Wiley and Sons.

Fig. 13. The enhancement of oxygen vacancies. (a) Summary of results of urea electrosynthesis catalyzed by Vo-S-IO-6 at − 0.5 to − 0.8 V vs. RHE; (b) Side view and top view of the charge density difference of the S-IO upon the adsorption of a *NO₂ on the (100) facets, where the equivalent surfaces show the build-up (yellow) and exhaustion (cyan) of charge in real space respectively; (c) Free energy plots of S-IO and Vo-S-IO-6 for the electrosynthesis of urea at 0 V vs. RHE; (d, e) DOS of the In1 and In2 in contact with O in *CO₂NH₂ [136]. Copyright 2023 Elsevier. (f) Urea yield rates of CeO₂, Vo-CeO₂-500, Vo-CeO₂-750, and Vo-CeO₂-1000 at various applied potentials; (g) SFG signals of intermediate species on Vo-CeO₂-750; (h) Comparison of the coupling energy barrier of *NO, *N, *NH and *NH₂ with *CO and protonation on Vo-enriched CeO₂ [22]. Copyright 2022 American Chemical Society. (i) The kinetic energy barrier of *CO+ *NO coupling on FeNi-N₆ [23] vs. on Vo-CeO₂-750. Copyright 2022 Springer Nature. (j) Transition states for the second C-N bond formation on Vo-enriched CeO₂ (111) surface, where *OCNO binds with *NO, and the C, N, O, and Ce (IV) atoms are represented by gray, blue, red, and white balls, respectively [22]. Copyright 2022 American Chemical Society.

more likely to undergo cleavage, promoting the protonation of $*CO_2NH_2$ [136]. Thus, it is likely that the Vo-regulated (100) facet further reduces the energy barrier for the protonation of $*CO_2NH_2$ while retaining the original active site, resulting in relatively high activity. This shows that crystal faces and Vo have a synergistic contribution to the electrocatalytic C-N coupled synthesis of urea, providing a new idea for the synthesis of efficient electrocatalysts under ambient conditions.

Notably, graphene-In_2O_3 did not induce early C-N coupling due to its weak adsorption of $*NO_2$, and therefore, the urea selectivity was poor. In addition to indium, the PdCu alloy catalyst also enhanced the adsorption of CO_2 and NO_3^-, promoting the spontaneous formation of $*CO_2NO_2$. Thus, increased adsorption of CO_2 as well as intermediates prior to the reduction of NO_3^- to $*NO_2$ seems to induce early C-N coupling, which indirectly reflected that there seems to be a great potential for inducing early C-N coupling ($*CO_2 + *NO_2$), but this still needs to be further explored.

In addition to the d- and p-block element catalysts mentioned above, the rare earth metal-based catalysts in the f-block also show excellent catalytic performance. For example, the Vo-CeO_2-750 electrocatalyst with abundant oxygen vacancies prepared by different annealing temperatures also showed good catalytic performance (Fig. 13f) [22]. Although oxygen vacancies can adsorb CO_2 and reduce it to CO, compared with the CO_2RR, the CO production rate under the condition of C-N coelectrolysis decreases sharply, which can be attributed to the fact that Vo-CeO_2 provides an adsorption site for NO_3^- [137–139]. In addition, Vo-CeO_2 inhibited the formation of the byproduct ammonia, which was attributed to Vo stabilizing the N-intermediate and inhibiting its hydrogenation to generate byproducts, which also facilitated the C-N coupling process. It can be seen from the electrochemical in situ SFG spectrum in Fig. 13g that the characteristic peak of Vo-CeO_2-750 can be attributed to *NO and *OCNO intermediates, indicating that the stable N-intermediate of the catalyst is *NO rather than *NH, *N, $*NH_2$ or other intermediates that easily form the byproduct NH_3 (Figs. 2 and 13 h) [22, 140]. At the same time, with the change in applied potential consistent with the changing trend of *OCNO, SFG reached the maximum value at -1.6 V, which was consistent with the experimental results in Fig. 13f. Thus, the C-N coupling mechanism of the process occurred under the condition that Vo achieved adsorption of CO_2, causing it to be reduced to *CO, but reduced the production of byproduct CO because Vo-CeO_2 also adsorbed NO_3^- (the process was similar to that of Vo-InOOH), while the oxygen vacancy also prevented further hydrogenation of *NO and promoted the formation of *OCNO. It has been proposed that C-N coupling on the V_o-CeO_2-750 surface is thermodynamically and kinetically advantageous. Similar to Fe-Ni-N_6, the C-N coupling of the process is also a two-step process. The first step is the coupling of *NO and *CO to form *ONCO, which is the most critical process. Notably, on the Fe-Ni bond, *NO tends to form *NH binding to *CO (+0.21 eV), but as shown in Fig. 13i, the energy barrier (+0.81 eV) overcome by the combination of *NO and *CO on the Fe-Ni bond is higher than the energy barrier (+0.27 eV) needed to overcome on Vo-CeO_2 with abundant oxygen vacancies. According to the characterization of the catalyst morphology and the theoretical DFT calculations, it can be seen that this is probably related to the binding nature of *NH with the active site [141–143]. From the adsorption conformation of the intermediate species on the catalyst, it can be seen that on Fe-Ni coordination, the nitrogen end of *NO or *NH binds to the Ni site (Fig. 10c), while on the surface of Vo-CeO_2, the oxygen vacancy induces the oxygen end of *NO to bind to the oxygen vacancy so that the nitrogen end of *NO will be directly exposed, reducing the spatial site resistance of the C-N coupling. Furthermore, CeO_2 lacking oxygen vacancies needs to overcome a large reaction energy barrier, which is consistent with the experimental results in Fig. 13f. As shown in Fig. 13j, the second C-N coupling was the combination of *ONCO and *NO to form *ONCONO (+0.24 eV), which in turn produces urea through the PCET process, but the first step of C-N coupling was considered the key. It can be seen that in the Vo-CeO_2 active site, *NO can directly bind to *CO as the first step of the C-N

coupling process without being activated to *NH before binding to *CO, as in the case of the Fe-Ni bond. However, the yield rate of Fe-Ni-N_6 is even higher than that of Vo-CeO_2-750 (20.2 mmol h^{-1} g^{-1} vs. 15.73 mmol h^{-1} g^{-1}, Fig. 4d), which is not only related to the catalyst mass itself but also most likely related to the C-N coupling rate [144]. Notably, in most cases, when the nitrogen source is an intermediate containing hydrogen atoms or both hydrogen and oxygen atoms, such as *NH, $*NH_2OH$, and $*NH_2$, the reaction system exhibits a better ammonia yield, while when the nitrogen source is an intermediate containing oxygen atoms alone, such as *NO or $*NO_2$, the ammonia yield of the reaction system decreases.

Regarding the inhibition of byproducts by oxygen vacancy engineering, the indium-based catalysts inhibited CO and H_2 more than the f-block catalysts, despite the lower urea yield than Vo-CeO_2-750. Oxygen vacancy engineering induced different C-N mechanisms for the different block catalysts. While this is likely to be related to the nature of the element, it also appears to be strongly linked to the adsorption of intermediates on the active site, which can be achieved by modulating the coordination environment. The enhanced adsorption of CO_2 or $*NO_2$ is likely to induce the onset of $*CO_2 + *NO_2$ coupling, which can be achieved by spatial and crystallographic modulation. In addition, changing the electron distribution seems to be a feasible strategy, such as alloying to alter the d-band electronic structure of the metal and the mentioned oxygen vacancy engineering, which would also enhance the adsorption of intermediates and lower the C-N coupling energy barrier. Similarly, if the active site is poorly adsorbed for $*NO_2$, it is likely to lead to further protonation to form *NH, $*NH_2$, or $*H_2NOH$ [25]. These N-intermediates can likely combine with any of the C-intermediates to synthesize urea via various pathways, but usually, these FE_{urea} are not excellent.

In terms of catalyst type, although the C-N coupling processes involved are different for single atom catalysts and oxide or alloy catalysts, these processes can be regulated by electronic structure [38]. For example, a Pd/Cu alloy could regulate the d-band of copper and alter the electron distribution, not only improving the catalytic performance but also facilitating the coupling of $*CO_2$ with $*NO_2$, producing a different reduction mechanism than that of the copper single atom. In this respect, tuning the local electronic environment may be an applicable method to improve the intrinsic activity of the electrocatalyst, making selective coupling of intermediates possible. Notably, loading Cu single atoms onto the CeO_2 surface (L-Cu_1-CeO_2) could enhance the FE_{urea} and urea yield [145]. The new hybridization orbitals of Cu_1-CeO_2 with NO_3^- and CO_2 promoted electron migration in Cu_1-CeO_2, providing new channels for electron exchange transport. Meanwhile, due to the adsorption of copper on NO_3^- and CO_2, C-N coupling was promoted. However, during the reaction, single copper atoms (Cu_1) reorganized into clusters (Cu_4), which were considered the real active sites. Compared to Vo-CeO_2-750, Cu_4 changed the electronic state of CeO_2 so that the adsorption and activation of *NO on the active sites were enhanced, and the energy barrier for *CO and *NO coupling was reduced. Although a high yield (52.84 mmol h^{-1} g$_{cat.}^{-1}$) was obtained, the FE_{urea} was not significantly enhanced, and the reaction system was still accompanied by the generation of many byproducts (H_2, CO, NH_3, etc.). Therefore, combining f-block metals and d-block still needs further investigation. Meanwhile, in the subsequent catalyst design, further in-depth exploration of the dynamic recombination process of the catalyst in the catalytic process with real active sites may be worthwhile to design catalysts with high activity.

The rate of organic nitrogen formation also seems to be an indicator of the electrocatalytic coreduction of CO_2 and NO_3^-. However, regardless of the control strategy, for the synthesis of urea, the production rate of the p-block metal catalyst is in the middle among all catalysts, while the d-block element catalyst shows a faster production rate. This may be similar to the properties of the role of the d-block element in the N_2RR [146,147]. This suggests that the construction of a Lewis acid site alone is not sufficient if the p-block elements are to achieve the same effect as

the d-block elements. Designing sites with high surface area and density can maximize the number of active sites and thus further enhance the production rate.
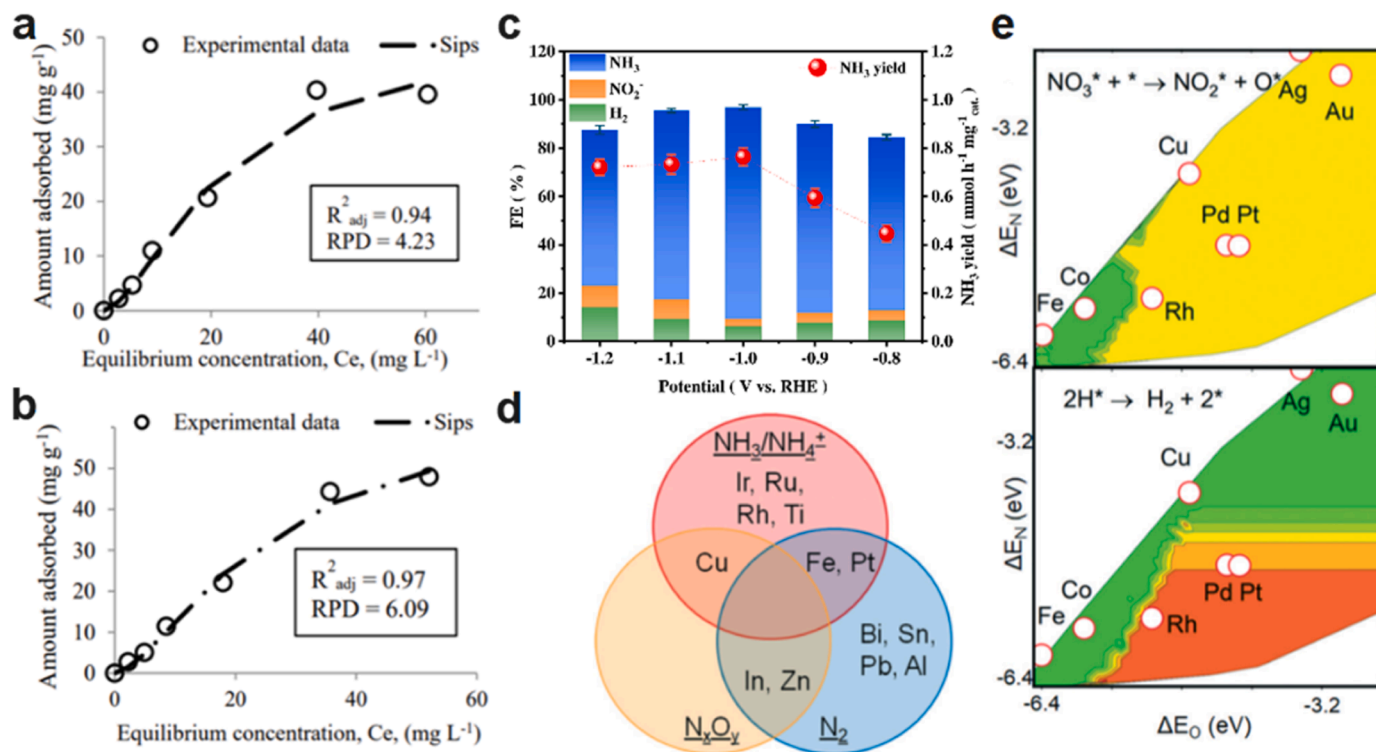
4. Evaluation of the practicability and feasibility of the reaction system

Domestic sewage, fertilizer, food and other industrial wastewater, and farmland drainage all contain large amounts of nitrogen. Eutrophication occurs when natural water bodies receive these effluents [148–152]. NO_3^- in wastewater is the decomposition product of nitrogen-containing organic matter at the last stage of the inorganic reaction. After ingestion by the human body, nitrate is converted into nitrite through the action of intestinal microorganisms, resulting in toxic effects [153]. Nitrites can oxidize normal human hemoglobin to methemoglobin, resulting in methemoglobin syndrome, loss of oxygen supply capacity, and tissue hypoxia [154]. Traditional NO_3^- removal methods are mainly based on biological denitrification technology, but traditional biological denitrification technology cannot satisfy the requirements of energy conservation and consumption reduction in sewage treatment. Furthermore, effluent nitrate nitrogen is also an important indicator leading to substandard total nitrogen emissions [155,156]. In addition, the final product of biological nitrogen removal is mainly N_2, which is not very practical. Coupled ion exchange/biological denitrification technologies have been shown to overcome the problems of the individual processes described above. However, a large amount of NaCl solution (50–100 g L^{-1}) is consumed by the ion exchange process for resin regeneration, and the recovered waste solution usually contains high concentrations of SO_4^{2-} and Cl^-, which requires further treatment and increases the operating cost [157].

At present, the main methods of nitrate removal are adsorption and

reduction of ammonia synthesis. Regarding the choice of metal catalysts, iron is always the best choice [158]. For example, iron-exchange nanobentonite is superior to Fe_3O_4 nanoparticles in removing NO_3^- and bicarbonate (HCO_3^-) from wastewater [159]. As shown in Fig. 14a and b, according to the Sips isothermal model, the adsorption energies of iron exchange nanobentonite and Fe_3O_4 nanoparticles for NO_3^- are 64.76 mg g^{-1} and 49.90 mg g^{-1}, respectively, and NO_3^- can be reduced to ammonia under electrocatalysis conditions. In addition, Fe_2TiO_5 nanofibers (FTO-E) prepared by the defect engineering method contain abundant oxygen vacancies. The Faraday efficiency reached 87.6% in phosphate-buffered brine solution containing 0.1 mol L^{-1} $NaNO_3$ (Fig. 14c), but this method may be accompanied by the formation of iron-containing sludge [24]. Therefore, compared with the traditional NO_3RR treatment of nitrate, the direct conversion of nitrate into valuable chemical products through C-N coupling has excellent potential. .

Notably, studies indicate that, in general, the concentration of NO_3^- is set at 0.1 mol L^{-1}, which can be achieved through the concentration of nitrate wastewater, such as evaporation and reverse osmosis [40]. It is feasible to obtain nitrogen sources in the NO_3RR from actual water bodies. To end the NO_x cycle and prevent damage to the environment, NO_3RR has considerable significance. Fig. 14d compares the selectivity of different metals to different products synthesized by the NO_3RR, which can also provide a theoretical reference for the coupling of the CO_2RR and NO_3RR by electrocatalysis at the present stage [160,161]. It can be seen that iron has a certain selectivity for the reduction of NO_3^- to NH_3, which seems to be consistent with the results in Fig. 10 and Table 2. Meanwhile, as a low-cost metal, iron has strong adsorption energy for NO_3^- (Fig. 14e) [161]. However, either too strong or too weak an adsorption capacity leads to a decrease in activity, but this adsorption energy does not seem to be unregulatable [11,161–163]. In addition, Cu has a strong ability to induce NO_3^- to NH_4^+, which is further verified in

Fig. 14. Sips models of nitrate isotherm adsorption onto Fe-exchanged nano-bentonite: (a) and onto Fe_3O_4 nanoparticles(b) [24]. Copyright 2019 Elsevier. (c) FE_{NH3}, FE_{NO2-} and FE_{H2}, and NH_3 yield of FTO-E tested at each given potential [159]. Copyright 2022 John Wiley and Sons. (d) Distribution of dominant products (>20% selectivity) formed for different pure metals in steady-state or cycling potential experiments, where the overlap regions indicate different product formations under various reaction conditions or a mixture of reaction products, and the selectivity towards NH_3/NH_4^+, N_2, and N_xO_y are represented by red, blue, and orange circles, respectively; (e)Computed degree of rate control (DRC) for nitrate dissociation and H* combination steps as a function of O and N adsorption energy at 0 V vs. RHE [161]. Copyright 2021 The Royal Society of Chemistry.

Table 1

Comparison of CO2RR and NO3-RR coupling properties (A-V: urea; W: Methylamine) of different catalyst structures.

Catalyst (s)	Active site (s)	Onset potential	FE [%]	j [mA cm^{-2}]	Yield rates	Byproducts	Ref.
[A] In(OH)$_3$-S	In(OH)$_3$ (100)	-0.5 V (vs. RHE)	53.4 @ −0.6 V (vs. RHE)	0.32(urea) @ −1.4 V (vs. RHE)	533.1 mg h^{-1} g^{-1} @ −0.6 V (vs. RHE)	H$_2$、NH$_3$	[2]
[B]Cu-GS-800	Cu-N$_4$	-0.5 V (vs. RHE)	28 @ −0.9 V (vs. RHE)	27 @ −0.9 V (vs. RHE)	1800 mg h^{-1} g^{-1} @ −1.0 V (vs. RHE)	H$_2$, CO, NH$_4^+$	[38]
[C] Vo-InOOH	Vo-In atom	-0.4 V (vs. RHE)	51 @ −0.5 V (vs. RHE)	42.11 @ −0.5 V (vs. RHE)	592.5 mg h^{-1} g^{-1} @ −0.5 V (vs. RHE)	H$_2$, CO, NO$_2^-$, NH$_3$	[25]
[D]F-CNT-300	C-F$_2$	-0.45 V (vs. RHE)	18 @ −0.65 V (vs. RHE)	0.3(urea) @ −0.65 V (vs. RHE)	382 mg h^{-1} g^{-1} @ −0.65 V (vs. RHE)	H$_2$, NH$_3$	[31]
[E]Fe-Ni-N$_6$	Fe-Ni bond	-1.1 V (vs. RHE)	17.8 @ −1.5 V (vs. RHE)	59.9 @ −1.5 V (vs. RHE)	1213 mg h^{-1} g^{-1} @ −1.5 V (vs. RHE)	CO, NH$_3$	[23]
[F] Fe(a)@C-Fe$_3$O$_4$/CNTs	Fe(a)@C, Fe$_3$O$_4$	-0.45 V (vs. RHE)	16.5 ± 6.1 @ −0.65 V (vs. RHE)	14.2 @ −0.9 V (vs. RHE)	1341.3 ± 112.6 mg h^{-1} g^{-1} @ −0.65 V (vs. RHE)	H$_2$、CO, NH$_3$	[68]
[G] Vo-CeO$_2$-750	Abundant Vo	-1.3 V (vs. RHE)	3.84 @ −1.6 V (vs. RHE)	19.8 @ −1.6 V (vs. RHE)	943.6 mg h^{-1} g^{-1} @ −1.6 V (vs. RHE)	H$_2$, CO, NO$_2^-$, NH$_3$	[22]
[H] XC72R-AuPd	AuPd(111)	-0.3 V (vs. RHE)	15.6 @ −0.4 V (vs. RHE)	17.6 @ −1.1 V (vs. RHE)	204.2 mg h^{-1} g^{-1} @ −0.5 V (vs. RHE)	H$_2$, CO, NO$_2^-$, NH$_3$, NH$_2$OH	[20]
[I] Cu@Zn Nanowires	Cu$_2$O@ZnO	-1.75 V (vs. SCE)	9.28 @ −1.02 V (vs. RHE)	3.13(urea) @ −1.02 V (vs. RHE)	7.29 μmol cm^{-2} h^{-1} @ −1.02 V (vs. RHE)	H$_2$, N$_2$, CO, NO$_2^-$, NH$_4^+$	[40]
[J] TiO$_2$-Nafion-ITC	TiO$_2$	/	40 @ −0.98 V (vs. Ag/AgCl)	0.18 @ −0.98 V (vs. Ag/AgCl)	0.33 μmol h^{-1} @ −0.98 V (vs. Ag/AgCl)	H$_2$, CO, NH$_3$	[53]
[K] graphene-In$_2$O$_3$	In$_2$O$_3$(111)	-0.15 V (vs. RHE)	10.46 @ −0.35 V (vs. RHE)	~20 @ −0.55 V (vs. RHE)	357.47 μg h^{-1} mg^{-1} @ −0.35 V (vs. RHE)	H$_2$, NO$_2^-$, NH$_3$	[84]
[L] Fe^{II}-Fe^{III}OOH@BiVO$_4$-n	Fe^{II}-Fe^{III}OOH@BiVO$_4$-2	-0.6 V (vs. RHE)	11.5 @ −0.8 V (vs. RHE)	> 80 @ −1.4 V (vs. RHE)	13.8 mmol h^{-1} g^{-1} @ −0.8 V (vs. RHE)	H$_2$, NO$_2^-$, N$_2$H$_4$, NH$_3$	[83]
[M] PdCu/CBC	PdCu(111)	-0.2 V (vs. RHE)	69.1 ± 3.8 @ −0.4 V (vs. RHE)	~6 @ −0.7 V (vs. RHE)	763.8 ± 42.8 μg h^{-1} mg^{-1} @ −0.65 V (vs. RHE)	H$_2$, CO, NO$_2^-$, NH$_3$	[119]
[N] Vo-S-IO-6	Vo-(100)facet	-0.5 V (vs. RHE)	60.6 @ −0.6 V (vs. RHE)	~2 @ −0.8 V (vs. RHE)	910.4 μg h^{-1} mg^{-1} @ −0.6 V (vs. RHE)	H$_2$, CO, NO$_2^-$, NH$_3$	[136]
[O] CoRuN$_6$	Ru/Co	-0.4 V (vs. RHE)	25.31 @ −0.6 V (vs. RHE)	3.04 @ −0.6 V (vs. RHE)	8.98 mmol h^{-1} g^{-1} @ −0.6 V (vs. RHE)	H$_2$, CO, CH$_4$, N$_2$, NO$_2^-$, NH$_3$, etc.	[117]
[P] 6 Å-Cu	ds between the copper facets	-0.15 V (vs. RHE)	51.97 @ −0.41 V (vs. RHE)	115.25(urea)@ −0.41 V (vs. RHE)	7541.9 μg h^{-1} mg^{-1} @ −0.41 V (vs. RHE)	H$_2$, CO, HCOOH, NH$_3$, etc.	[124]
[Q] RhCu-uls	RhCu-uls(111)	-0.5 V (vs. RHE)	34.82 ± 2.47 @ -0.6 V (vs. RHE)	~4.5 @ −1.0 V (vs. RHE)	26.81 ± 0.62 mmol h^{-1} g^{-1} @ −0.6 V (vs. RHE)	NO$_2^-$, NH$_3$, N$_2$H$_4$	[122]
[R] Ru-Cu CF	Ru sites	-0.2 V (vs. Ag/AgCl)	25.4 @ −0.3 V (vs. Ag/AgCl)	~13.1 @ −0.3 V (vs. Ag/AgCl)	151.6 μg h^{-1} cm^{-2} @ −0.3 V (vs. Ag/AgCl)	CO, HCOOH, NO$_2^-$, NH$_4^+$, etc.	[121]
[S] m-Cu$_2$O	Cu^0-Cu$^+$	-1.1 V (vs. RHE)	9.43 @ −1.3 V (vs. RHE)	4.42(urea) @ −1.3 V (vs. RHE)	29.2 mmol h^{-1} g^{-1} @ −1.3 V (vs. RHE)	H$_2$, CO, HCOOH, CH$_4$, NH$_3$, etc.	[123]
[T] N-doped carbon-1000	N-species	-1.2 V (vs. RHE)	1.67 @ −1.5 V (vs. RHE)	~43 @ −1.5 V (vs. RHE)	498.5 mg h^{-1} g^{-1} @ −1.5 V (vs. RHE)	Ammonia, etc.	[82]
[U] L-Cu$_1$-CeO$_2$	Cu$_4$ clusters on CeO$_2$	-1.2 V (vs. RHE)	5.29 @ −1.6 V (vs. RHE)	~80 @ −1.6 V (vs. RHE)	52.84 mmol h^{-1} g^{-1} @ −1.6 V (vs. RHE)	H$_2$, CO, CH$_4$, NO$_2^-$, NH$_3$, etc.	[145]
[V] CoPc-COF@TiO$_2$ NTs	CoPc; anatase phase TiO$_2$.	-0.5 V (vs. RHE)	49%@ −0.6 V (vs. RHE)	~20 @ −0.6 V (vs. RHE)	1205 μg h^{-1} cm^{-2} @ −0.6 V (vs. RHE)	H$_2$, CO, NO$_2^-$, NH$_3$	[85]
[W] CoPC-NH$_2$/CNT	CoPC-NH$_2$	-0.92 V (vs. RHE)	13 @ −0.92 V (vs. RHE)	3.42(H$_3$CNH$_2$)@ −0.92 V (vs. RHE)	/	H$_2$, CO, CH$_3$OH, NO$_2^-$, NH$_3$, etc.	[9]

Fig. 14d. Compared with d-block metals, the p-block metal indium induces the process of NO$_3^-$ to N$_x$O$_y$, which seems to be regarded as the early reduction of the NO$_3$RR. That is, N$_x$O$_y$ may be directly involved in C-N coupling without being reduced to intermediates such as *NH or *NH$_2$, and thus, the yield of the byproduct NH$_3$/NH$_4^+$ is low, which can be interpreted as an inhibition of the NO$_3$RR. Although Zn can also induce this process, its ability to inhibit the HER is not as good as that of indium. This further explains why indium is regarded as an excellent element for electrocatalytic coupling of the CO$_2$RR and NO$_3$RR at the present stage, but it does not mean that the design of catalysts is limited to indium. At this stage, other p-block metals, such as Al [164] and Bi [77], and other nonmetal elements, such as P [165] and B [166], have been shown to have the ability to catalyze nitrogen conversion; it is not impossible to apply these mechanisms to the electrocatalytic coreduction of CO$_2$ and NO$_3^-$, and it is still possible to design new and efficient p-block activation sites in the future.

5. Summary and outlook

In conclusion, electrocatalytic coupling of the CO$_2$RR and NO$_3$RR to synthesize carbon, nitrogen, and organic matter with higher value has been regarded as a new technology to prevent CO$_2$ and NO$_3^-$ pollution in recent years, and this approach has excellent potential. Considering the mechanism of coreduction of CO$_2$ and NO$_3^-$ by electrocatalysis, the key is to generate intermediates that can be coupled with C-N. However, this requires an efficient catalyst that can properly absorb and activate CO$_2$ and NO$_3^-$ at the same time. However, this is simply not enough because the CO$_2$RR and NO$_3$RR each generate competing products, and the Faraday efficiency is generally higher than that of carbon, nitrogen, and organic matter. Furthermore, the high reaction energy barrier also needs to be overcome [167]. However, a variety of mechanisms exist for carbon-nitrogen coupling. The same product involves several coupling mechanisms, such as the preparation of urea. The C intermediates and N

Table 2
Mechanism of C-N coupling induced by different catalyst types (active sites).

Major C-N coupling	Relevant catalysts and active sites	Ref.
$*CO_2$ + $*NO_2$	Vo-InOOH (Vo-In atom); In(OH)$_3$ [In(OH)$_3$ (100)]; Vo-S-IO-6 [Vo-(100)facet]; PdCu/CBC [PdCu(111)]; CoRuN$_6$ (Ru/Co);	[2,25,117,119, 136]
$*CO$ + $*H_2NOH$	XC72R-AuPd [AuPd(111)]	[20]
$*CO$ + $*NH_2$	Cu-GS-800 (Cu-N$_4$); F-CNT-300 (C-F$_2$); Cu@Zn Nanowires (Cu$_2$O@ZnO); Fe(a)@C-Fe$_3$O$_4$/CNTs [Fe(a)@C and Fe$_3$O$_4$]; CoPc-COF@TiO$_2$ NTs (CoPC-NH$_2$)	[31,38,40,68, 85]
$*CO$ + $*NH$	FeNi-N$_6$ (Fe-Ni bond)	[23]
$*CO$ + $*NO$	Vo-CeO$_2$ (Abundant Vo); Fe^{II}-Fe^{III}OOH@BiVO$_4$-n (Fe^{II}-Fe^{III}OOH@BiVO$_4$-2); m-Cu$_2$O (Cu^0-Cu$^+$); N-doped carbon-1000 (N-species); L-Cu$_1$-CeO$_2$ (Cu$_4$ clusters on CeO$_2$)	[22,82,83,123, 145]
$*CO_2$ + $*NH_2$	graphene-In$_2$O$_3$ [In$_2$O$_3$(111)]	[84]
$*HCHO$ + $*H_2NOH$	CoPC-NH$_2$/CNT (CoPC-NH$_2$)	[9]
$*C_2H_3OH$ + $*H_2NOH$	oxide-derived Cu catalysts (Cu nanoparticles)	[14]

intermediates corresponding to urea preparation by this process vary, the advantages of different types of intermediates are different, and the corresponding reduction/coupling mechanisms are also different. However, regardless of the kind of mechanism, there is still the problem of poor selectivity at this stage. In view of this, researchers have started from the reaction mechanism and modified the catalyst to inhibit the formation of competing products as much as possible, such as by reducing the formation of PVC products or preventing the desorption of $*CO$ (reducing the formation of CO). Metal-derived oxides or mono-/diatomic catalysts based on copper, iron, nickel, gold, and indium have excellent catalytic performance. The main properties that need to be enhanced differ between the different types of elemental catalysts. The design of catalysts includes the control of metal centers, the control of metal crystal surfaces or structural defects, and the preparation of diatomic active sites to enhance the thermodynamics and kinetics of C-N critical coupling. Some regulatory strategies at this stage achieve the trinity of the active site, activation site, and coupling site, which enhances the key C-N coupling from thermodynamic and kinetic perspectives. However, there still exists low FE$_{urea}$, low yield, or more competitive reactions. In this way, there is still a wide scope of exploration to enhance C-N coupling by modifying catalysts. Here, some prospects and challenges are proposed:

(1) Further exploration of electrocatalytic C-N coupling. To date, C-N coupling has been studied in the direction of urea synthesis, and continuous breakthroughs have been made. In addition, copper-based and inorganic nonmetallic-based catalysts can also be used to synthesize other valuable organic nitrogen compounds, such as methylamine and ethylamine, by catalytic electro-reduction of CO$_2$ and NO$_3$. However, the selectivity of these products still needs to be improved due to the high reaction rates of the CO$_2$RR and NO$_3$RR or the adsorption of intermediates on the catalyst surface and other factors, and there is great space for development. However, this proves the excellent potential of the electrocatalytic synthesis of organic nitrogen compounds from inexpensive and abundant inorganic raw materials. At the same time, it is worth noting that these organic nitride compounds are coupled by different types of intermediates of the CO$_2$RR and NO$_3$RR. Interestingly, the CO$_2$RR seems to play a role in determining the product type in C-N coupling. For example, C-intermediates for urea synthesis come from CO$_2$ to CO. Methylamine was synthesized from CO$_2$ to CH$_3$OH. N-Intermediates, such as $*NH_2OH$, are involved in the C-N coupling of urea and other organonitrogen compounds. To date, the CO$_2$RR can synthesize many different kinds of carbon products, and the reduction pathways or intermediates corresponding to these carbon products are also different [168–171]. Therefore, whether these intermediates will participate in the C-N coupling formation of other carbon and nitrogen organic compounds still needs to be further explored.

(2) Further development of semiconductor and nonmetallic elements in p-block elements. Catalysts based on p-block elements are still preferred for electrocatalytic coupling of the CO$_2$RR and NO$_3$RR compared to d-block element, such as transition metals, or f-block element, for several reasons: (a) the advantages of p-block element nontoxicity and low cost; (b) the unique ability of p-block element to inhibit HER; (c) the inhibition effect of p-block element catalysts on byproducts except H$_2$ are better than that of d-block element catalysts; and (d) in some cases, various types of modulation of the p-block monometallic active site can increase the adsorption of intermediates or reduce the energy barrier of the $*CO_2$ + $*NO_2$ coupling, producing high FE$_{urea}$ that is generally superior to that of the d-block monometallic site regulated in an equivalent measure. Indium is a semiconductor element, and the efficient catalytic C-N coupling by overly successful induction of a semiconductor-type transition for the CO$_2$RR provides a research basis for future semiconductor development of C-N coupling. In this way, it is worthwhile to develop semiconductor effects similar to those of indium, such as bismuth, which has semiconductor properties [172–176]. F-doped C can catalyze C-N coupling, which proves that nonmetallic elements also have considerable development space, and the development of new nonmetallic elements is also worth further exploration, such as nonmetallic element B. Notably, the weak hydrogen adsorption ability of these two elements is also worthy of being used in the C-N coupling process. In particular, B has been proven to catalyze N$_2$RR efficiently. Whether the empty sp orbital similar to the Lewis acid site can catalyze the NO$_3$RR remains to be explored because increasing the NO$_3$RR can inhibit the CO$_2$RR to a certain extent. This is also a strategy to improve the efficiency of catalytic C-N coupling. At the same time, it also lays a foundation for nonmetallic elements to catalyze C-N coupling.

(3) Further exploration of metal coordination center regulation. Combined with the advantages of p-block elements, the current oxygen position engineering related to adjusting the coordination structure or coordination environment can regulate the electronic structure of p-block metallic elements or construct Lewis acid sites to achieve the adsorption of intermediates to further accelerate the catalytic C-N coupling process. Although C-N coupling can be divided into one-step and two-step coupling processes, the two-step C-N coupling pathway involved in the construction of d-block bimetal or double sites can also reduce the reaction energy barrier of coupling to a large extent, such as Fe-Ni bonds. Most importantly, it even achieves an effect similar to or even surpassing the p-block element's inhibition of HER or excessive CO$_2$RR. However, the selectivity of carbon and nitrogen target products needs to be improved. Therefore, the establishment of double p-block element active sites may be a feasible method to further enhance the advantages of p-block elements inhibiting HER, such as the construction of M$_1$-M$_2$-N-C of p-block metals.

Alternatively, loading two or more p-block element sites is not limited to metal elements on the same carrier. While constructing Lewis acid sites to reduce the reaction energy barrier, the ability to inhibit the HER and even the ability to inhibit the CO_2RR and NO_3RR to produce byproducts can be further improved to efficiently catalyze C-N coupling to prepare carbon and nitrogen organic compounds. The promotion of early C-N coupling seems to have promising applications, but the regulation of the intrinsic activity of the catalyst cannot be ignored. Thus, systematic studies are necessary to identify optimized dual active species and their configurations, such as alloys, intermetallic compounds, supported catalysts, and composite oxides. In addition, the design of reactors or flow cells is necessary for the large-scale synthesis of organic carbon and nitrogen compounds.

(4) Although the NO_3RR has been proven to have great development prospects compared with the traditional N_2RR, such as a low energy barrier and high conversion rate, and is considered the best strategy to prevent nitrate pollution, few studies have focused on the utilization of nitrate wastewater [177]. At the present stage, the physical method only concentrates nitrate wastewater but does not remove nitrogen [178,179]. The chemical method will also generate a large amount of sludge, and the combination of the CO_2RR and NO_3RR, which are popular at the present stage, is a reasonable strategy to solve CO_2 and NO_3 pollution at the same time. In the future, the induction of NO_3 to N_xO_y rather than $*NH/*NH_2$, that is, the induction mechanism and the adsorption of carbon and nitrogen sources to guide the design of catalysts, will be a priority direction. However, this does not mean that $*NH$ and other intermediates will not efficiently catalyze C-N coupling. In the long run, electrocatalytic coupling of the CO_2RR and NO_3RR can address both the greenhouse effect and nitrate pollution problems, but there is still a wide range of areas to explore.

Declaration of Competing Interest

The authors declare that they have no known competing financial interests or personal relationships that could have appeared to influence the work reported in this paper.

Data Availability

Data will be made available on request.

Acknowledgments

Appendix A. Supporting information

Supplementary data associated with this article can be found in the online version at doi:10.1016/j.apcatb.2023.123292.

References

[1] E. Rueda, V. Senatore, T. Zarra, V. Naddeo, J. García, M. Garfí, Life cycle assessment and economic analysis of bioplastics production from cyanobacteria, Sustain. Mater. Technol. 35 (2023), e00579.
[2] C. Lv, L.X. Zhong, H.J. Liu, Z.W. Fang, C.S. Yan, M.X. Chen, Y. Kong, C. Lee, D. B. Liu, S.Z. Li, Selective electrocatalytic synthesis of urea with nitrate and carbon dioxide, Nat. Sustain. 4 (2021) 868–876.
[3] J. Leverett, J.A. Yuwono, P. Kumar, T. Tran Phu, J. Qu, J. Cairney, X.C. Wang, A. N. Simonov, R.K. Hocking, B. Johannessen, Impurity tolerance of unsaturated Ni-NC active sites for practical electrochemical CO_2 reduction, ACS Energy Lett. 7 (2022) 920–928.
[4] C. Chen, X.R. Zhu, X.J. Wen, Y.Y. Zhou, L. Zhou, H. Li, L. Tao, Q.L. Li, S.Q. Du, T. T. Liu, Coupling N_2 and CO_2 in H_2O to synthesize urea under ambient conditions, Nat. Chem. 12 (2020) 717–724.
[5] M.H. Jiang, M.F. Zhu, M.J. Wang, Y. He, X.J. Luo, C.J. Wu, L.Y. Zhang, Z. Jin, Review on electrocatalytic coreduction of carbon dioxide and nitrogenous species for urea synthesis, ACS Nano 17 (2023) 3209–3224.
[6] M.L. Yuan, J.W. Chen, Y.L. Bai, Z.J. Liu, J.X. Zhang, T.K. Zhao, Q. Wang, S.W. Li, H.Y. He, G.J. Zhang, Unveiling electrochemical urea synthesis by co-activation of CO_2 and N_2 with Mott-Schottky heterostructure catalysts, Angew. Chem. Int. Ed. 133 (2021) 11005–11013.
[7] S. Wang, H.X. Gao, L. Li, K.S. Hui, D.A. Dinh, S.X. Wu, S. Kumar, F.M. Chen, Z. P. Shao, K.N. Hui, High-throughput identification of highly active and selective single-atom catalysts for electrochemical ammonia synthesis through nitrate reduction, Nano Energy 100 (2022), 107517.
[8] M.K. Xia, C.L. Mao, A. Gu, A.A. Tountas, C.Y. Qiu, T.E. Wood, Y.F. Li, U. Ulmer, Y. F. Xu, C.J. Viasus, J. Ye, C.X. Q, G. Ozin, Solar urea: towards a sustainable fertilizer industry, Angew. Chem. Int. Ed. 61 (2022), e202110158.
[9] Y.S. Wu, Z. Jiang, Z.C. Lin, Y.Y. Liang, H.L. Wang, Direct electrosynthesis of methylamine from carbon dioxide and nitrate, Nat. Sustain. 4 (2021) 725–730.
[10] G.F. Chen, Y.F. Yuan, H.F. Jiang, S.Y. Ren, L.X. Ding, L. Ma, T.P. Wu, J. Lu, H. H. Wang, Electrochemical reduction of nitrate to ammonia via direct eight-electron transfer using a copper-molecular solid catalyst, Nat. Energy 5 (2020) 605–613.
[11] Y.H. Wang, A. Xu, Z.Y. Wang, L.S. Huang, J. Li, F.W. Li, J. Wicks, M.C. Luo, D. H. Nam, C.S. Tan, Enhanced nitrate-to-ammonia activity on copper-nickel alloys via tuning of intermediate adsorption, J. Am. Chem. Soc. 142 (2020) 5702–5708.
[12] Y.T. Wang, W. Zhou, R.R. Jia, Y.F. Yu, B. Zhang, Unveiling the activity origin of a copper-based electrocatalyst for selective nitrate reduction to ammonia, Angew. Chem. Int. Ed. 59 (2020) 5350–5354.
[13] Y.G. Feng, H. Yang, Y. Zhang, X.Q. Huang, L.G. Li, T. Cheng, Q. Shao, Te-doped Pd nanocrystal for electrochemical urea production by efficiently coupling carbon dioxide reduction with nitrite reduction, Nano Lett. 20 (2020) 8282–8289.
[14] Z.X. Tao, Y.S. Wu, Z.S. Wu, B. Shang, C. Rooney, H.L. Wang, Cascade electrocatalytic reduction of carbon dioxide and nitrate to ethylamine, J. Energy Chem. 65 (2022) 367–370.
[15] B.H. Suryanto, K. Matuszek, J. Choi, R.Y. Hodgetts, H.L. Du, J.M. Bakker, C. S. Kang, P.V. Cherepanov, A.N. Simonov, D.R. MacFarlane, Nitrogen reduction to ammonia at high efficiency and rates based on a phosphonium proton shuttle, Science 372 (2021) 1187–1191.
[16] F. Barzagli, F. Mani, M. Peruzzini, From greenhouse gas to feedstock: formation of ammonium carbamate from CO_2 and NH_3 in organic solvents and its catalytic conversion into urea under mild conditions, Green. Chem. 13 (2011) 1267–1274.
[17] C. He, Z.Y. Wu, L. Zhao, M. Ming, Y. Zhang, Y.P. Yi, J.S. Hu, Identification of FeN_4 as an efficient active site for electrochemical N_2 reduction, ACS Catal. 9 (2019) 7311–7317.
[18] C. Tang, Y. Zheng, M. Jaroniec, S.Z. Qiao, Electrocatalytic refinery for sustainable production of fuels and chemicals, Angew. Chem. Int. Ed. 60 (2021) 19572–19590.
[19] M. Jouny, J.J. Lv, T. Cheng, B.H. Ko, J.J. Zhu, W.A. Goddard, F. Jiao, Formation of carbon-nitrogen bonds in carbon monoxide electrolysis, Nat. Chem. 11 (2019) 846–851.
[20] H. Wang, Y. Jiang, S.J. Li, F.L. Gou, X.R. Liu, Y.M. Jiang, W. Luo, W. Shen, R. X. He, M. Li, Realizing efficient CN coupling via electrochemical co-reduction of CO_2 and NO_3 on AuPd nanoalloy to form urea: Key CN coupling intermediates, Appl. Catal. B Environ. 318 (2022), 121819.
[21] C.H. Wang, C.M. Li, J.L. Liu, C.X. Guo, Engineering transition metal-based nanomaterials for high-performance electrocatalysis, Mater. Rep.: Energy 1 (2021), 100006.
[22] X.X. Wei, X.J. Wen, Y.Y. Liu, C. Chen, C. Xie, D.D. Wang, M.Y. Qiu, N.H. He, P. Zhou, W. Chen, Oxygen vacancy-mediated selective C-N coupling toward electrocatalytic urea synthesis, J. Am. Chem. Soc. 144 (2022) 11530–11535.
[23] X.R. Zhang, X.R. Zhu, S.W. Bo, C. Chen, M.Y. Qiu, X.X. Wei, N.H. He, C. Xie, W. Chen, J.Y. Zheng, Identifying and tailoring C-N coupling site for efficient urea synthesis over diatomic Fe-Ni catalyst, Nat. Commun. 13 (2022) 1–9.
[24] R. Mukhopadhyay, T. Adhikari, B. Sarkar, A. Barman, R. Paul, A.K. Patra, P. C. Sharma, P. Kumar, Fe-exchanged nano-bentonite outperforms Fe_3O_4 nanoparticles in removing nitrate and bicarbonate from wastewater, J. Hazard. Mater. 376 (2019) 141–152.
[25] C. Lv, C. Lee, L.X. Zhong, H.J. Liu, J.W. Liu, L. Yang, C.S. Yan, W. Yu, H.H. Hng, Z. M. Qi, A defect engineered electrocatalyst that promotes high-efficiency urea synthesis under ambient conditions, ACS Nano (5) (2022) 8213–8222.
[26] P.P. Li, Z.Y. Jin, Z.W. Fang, G.H. Yu, A single-site iron catalyst with preoccupied active centers that achieves selective ammonia electrosynthesis from nitrate, Energy Environ. Sci. 14 (2021) 3522–3531.
[27] Y. Wang, C. Wang, M. Li, Y. Yu, B. Zhang, Nitrate electroreduction: mechanism insight, in situ characterization, performance evaluation, and challenges, Chem. Soc. Rev. 50 (2021) 6720–6733.
[28] J. Long, S.M. Chen, Y.L. Zhang, C.X. Guo, X.Y. Fu, D.H. Deng, J.P. Xiao, Direct electrochemical ammonia synthesis from nitric oxide, Angew. Chem. Int. Ed. 59 (2020) 9711–9718.
[29] Y.M. Huang, R. Yang, C.H. Wang, N.N. Meng, Y.M. Shi, Y.F. Yu, B. Zhang, Direct Electrosynthesis of urea from carbon dioxide and nitric oxide, ACS Energy Lett. 7 (2021) 284–291.
[30] T. Hu, C.H. Wang, M.T. Wang, C.M. Li, C.X. Guo, Theoretical insights into superior nitrate reduction to ammonia performance of copper catalysts, ACS Catal. 11 (2021) 14417–14427.

[31] X.W. Liu, P.V. Kumar, Q. Chen, L.J. Zhao, F.H. Ye, X.Y. Ma, D. Liu, X.C. Chen, L. M. Dai, C.G. Hu, Carbon nanotubes with fluorine-rich surface as metal-free electrocatalyst for effective synthesis of urea from nitrate and CO₂, Appl. Catal. B Environ. 316 (2022), 121618.

[32] D.R. Corbin, S. Schwarz, G.C. Sonnichsen, Methylamines synthesis: A review, Catal. Today 37 (1997) 71–102.

[33] Z.M. Wu, H. Liang, J. Lu, Synthesis of poly (N-isopropylacrylamide)-poly (ethylene glycol) miktoarm star copolymers via RAFT polymerization and aldehyde aminooxy click reaction and their thermoinduced micellization, Macromolecules 43 (2010) 5699–5705.

[34] J.E. Hudak, R.M. Barfield, G.W. de Hart, P. Grob, E. Nogales, C.R. Bertozzi, D. Rabuka, Synthesis of heterobifunctional protein fusions using copper-free click chemistry and the aldehyde tag, Angew. Chem. Int. Ed. 51 (2012) 4161–4165.

[35] E. Subbotina, F. Ram, S.V. Dvinskikh, L.A. Berglund, P. Olsén, Aqueous synthesis of highly functional, hydrophobic, and chemically recyclable cellulose nanomaterials through oxime ligation, Nat. Commun. 13 (1) (2022) 12.

[36] M. Horvat, V. Weilch, R. Rädisch, S. Hecko, A. Schiefer, F. Rudroff, B. Wilding, N. Klempier, M. Pátek, L. Martínková, Chemoenzymatic one-pot reaction from carboxylic acid to nitrile via oxime, Catal. Sci. Technol. 12 (2022) 62–66.

[37] M. Jouny, J.J. Lv, T. Cheng, B.H. Ko, J.J. Zhu, W.A. Goddard III, F. Jiao, Formation of carbon-nitrogen bonds in carbon monoxide electrolysis, Nat. Chem. 11 (2019) 846–851.

[38] J. Leverett, T. Tran Phu, J.A. Yuwono, P. Kumar, C. Kim, Q. Zhai, C. Han, J. Qu, J. Cairney, A.N. Simonov, Tuning the coordination structure of Cu-N-C single atom catalysts for simultaneous electrochemical reduction of CO₂ and NO₃⁻ to urea, Adv. Energy Mater. 12 (2022) 2201500.

[39] X.S. Lv, T. Mou, J.W. Li, L.Z. Kou, T. Frauenheim, Tunable surface chemistry in heterogeneous bilayer single-atom catalysts for electrocatalytic NOₓ reduction to ammonia, Adv. Funct. Mater. 32 (2022) 2201262.

[40] N.N. Meng, X.M. Ma, C.H. Wang, Y.T. Wang, R. Yang, J. Shao, Y.M. Huang, Y. Xu, B. Zhang, Y.F. Yu, Oxide-derived core-shell Cu @ Zn nanowires for urea electrosynthesis from carbon dioxide and nitrate in water, ACS Nano 16 (2022) 9095–9104.

[41] G.Y. He, H.Y. Tang, H. Wang, Z.Y. Bian, Highly selective and active Pd-In/three-dimensional graphene with special structure for electroreduction CO₂ to formate, Electroanalysis 30 (2018) 84–93.

[42] S.L. Li, W.C. Yu, X.Y. Zhang, L. Liu, H. Wang, Y.Y. Peng, Z.Y. Bian, Mo-based heterogeneous interface and sulfur vacancy synergistic effect enhances the fenton-like catalytic performance for organic pollutant degradation, ACS Appl. Mater. Interfaces 15 (2022) 1326–1338.

[43] Y.J. Yang, Z.Y. Bian, L. Zhang, H. Wang, Bi@BiOₓ(OH)ᵧ modified oxidized g-C₃N₄ photocatalytic removal of tetracycline hydrochloride with highly effective oxygen activation, J. Hazard. Mater. 427 (2022), 127866.

[44] L. Zhang, X.Y. Zhang, C. Wei, F. Wang, H. Wang, Z.Y. Bian, Interface engineering of z-scheme α-Fe₂O₃/g-C₃N₄ photoanode: simultaneous enhancement of charge separation and hole transportation for photoelectrocatalytic organic pollutant degradation, Chem. Eng. J. 435 (2022), 134873.

[45] M. Abaszadeh, R. Hosseinzadeh, M. Tajbakhsh, S. Ghasemi, The synthesis of functionalized magnetic graphene oxide with 5-amino-1, 10-phenanthroline and investigation of its dual application in CN coupling reactions and adsorption of heavy metal ions, J. Mol. Struct. 1261 (2022), 132832.

[46] X.X. Wei, Y.Y. Liu, X.R. Zhu, S.W. Bo, L. Xiao, C. Chen, T.T.T. Nga, Y.Q. He, M. Y. Qiu, C. Xie, Dynamic reconstitution between copper single atoms and clusters for electrocatalytic urea synthesis, Adv. Mater. (2023), 2300020.

[47] W.H. Zhang, Y.Y. Peng, Y.J. Yang, L. Zhang, Z.Y. Bian, H. Wang, Bismuth-rich strategy intensifies the molecular oxygen activation and internal electrical field for the photocatalytic degradation of tetracycline hydrochloride, Chem. Eng. J. 430 (2022), 132963.

[48] N. Li, X.Z. Song, L. Wang, X.L. Geng, H. Wang, H.Y. Tang, Z.Y. Bian, Single-atom cobalt catalysts for electrocatalytic hydrodechlorination and oxygen reduction reaction for the degradation of chlorinated organic compounds, ACS Appl. Mater. Interfaces 12 (2020) 24019–24029.

[49] T.T. Adamson, K.B. Uttley, S.P. Kelley, W.H. Bernskoetter, Coordination chemistry of (triphos) Fe(0) ethylene complexes and their application to CO₂ valorization, Organometallics 41 (2022) 2909–2919.

[50] S.T. Stripp, B.R. Duffus, V. Fourmond, C. Léger, S. Leimkühler, S. Hirota, Y. Hu, A. Jasniewski, H. Ogata, M.W. Ribbe, Second and outer coordination sphere effects in nitrogenase, hydrogenase, formate dehydrogenase, and CO dehydrogenase, Chem. Rev. 122 (2022) 11900–11973.

[51] Y.M. Huang, Y.T. Wang, Y.M. Wu, Y.F. Yu, B. Zhang, Electrocatalytic construction of the C-N bond from the derivates of CO₂ and N₂, Sci. China Chem. 65 (2021) 204–206.

[52] J.J. Fu, Y. Yang, J.S. Hu, Dual-sites tandem catalysts for C-N bond formation via electrocatalytic coupling of CO₂ and nitrogenous small molecules, ACS Mater. Lett. 3 (2021) 1468–1476.

[53] D. Saravanakumar, J. Song, S. Lee, N.H. Hur, W. Shin, Electrocatalytic conversion of carbon dioxide and nitrate ions to urea by a titania-nafion composite electrode, ChemSusChem 10 (2017) 3999–4003.

[54] Y. Yu, C.H. Wang, Y.F. Yu, Y.T. Wang, B. Zhang, Promoting selective electroreduction of nitrates to ammonia over electron-deficient Co modulated by rectifying Schottky contacts, Sci. China Chem. 63 (2020) 1469–1476.

[55] X. Liu, L.S. Zhu, H. Wang, G.Y. He, Z.Y. Bian, Catalysis performance comparison for electrochemical reduction of CO₂ on Pd-Cu/graphene catalyst, RSC Adv. 6 (2016) 38380–38387.

[56] X.L. Geng, L. Wang, L. Zhang, H. Wang, Y.Y. Peng, Z.Y. Bian, H₂O₂ production and in situ sterilization over a ZnO/g-C₃N₄ heterojunction photocatalyst, Chem. Eng. J. 420 (2021), 129722.

[57] H. Kawano, Effective work functions of the elements: database, most probable value, previously recommended value, polycrystalline thermionic contrast, change at critical temperature, anisotropic dependence sequence, particle size dependence, Prog. Surf. Sci. 97 (2022), 100583.

[58] C. Wu, F.M. Wu, H.Z. Hu, C.Q. Ma, J.H. Ye, S.L. Wang, H.P. Wu, J.B. Wang, A. P. Liu, D.Y. Guo, Work function tunable laser induced graphene electrodes for Schottky type solar-blind photodetectors, Appl. Phys. Lett. 120 (2022), 101102.

[59] C.B. Liu, S.Y. Han, M.Y. Li, X.D. Chong, B. Zhang, Electrocatalytic deuteration of halides with D₂O as the deuterium source over a copper nanowire arrays cathode, Angew. Chem. Int. Ed. 132 (2020) 18685–18689.

[60] J. Rosen, G.S. Hutchings, Q. Lu, R.V. Forest, A. Moore, F. Jiao, Electrodeposited Zn dendrites with enhanced CO selectivity for electrocatalytic CO₂ reduction, ACS Catal. 5 (2015) 4586–4591.

[61] D.D. Xu, L. Zhang, H. Wang, Z.Y. Bian, Optimization of electrochemical sequential reduction-oxidation of chlorophene with CoNi alloy anchored ionic liquid-graphene cathode: Comparison, mechanism and toxicity study, Chem. Eng. J. 358 (2019) 1371–1382.

[62] X.Z. Song, D.D. Xu, Q. Shi, F. Wang, H. Wang, Z.Y. Bian, Abundant size-controlled Cu-Ni (Fe) alloy nanoparticles decorated reduced graphene with enhanced electrocatalytic activities for chloramphenicol, J. Electrochem. Soc. 164 (2017) H779–H787.

[63] N. Chebotareva, T. Nyokong, Metallophthalocyanine catalysed electroreduction, J. Appl. Electrochem. 27 (1997) 975–981.

[64] L.B. Li, K. Yuan, Y.W. Chen, Breaking the scaling relationship limit: From single-atom to dual-atom catalysts, Acc. Mater. Res. 6 (2022) 584–596.

[65] H.Y. Tang, Z.Y. Bian, Y.Y. Peng, S.L. Li, H. Wang, Stepwise dechlorination of chlorinated alkenes on an Fe-Ni/rGO/Ni foam cathode: Product control by one-electron-transfer reactions, J. Hazard. Mater. 433 (2022), 128744.

[66] L.Q. Li, C. Tang, H.Y. Jin, K. Davey, S.Z. Qiao, Main-group elements boost electrochemical nitrogen fixation, Chem 7 (2021) 3232–3255.

[67] C. Lv, J.W. Liu, C. Lee, Q. Zhu, J.W. Xu, H.G. Pan, C. Xue, Q.Y. Yan, Emerging p-block-element-based electrocatalysts for sustainable nitrogen conversion, ACS Nano 16 (2022) 15512–15527.

[68] J. Geng, S.H. Ji, M. Jin, C. Zhang, M. Xu, G.Z. Wang, C.H. Liang, H.M. Zhang, Ambient electrosynthesis of urea with nitrate and carbon dioxide over iron-based dual-sites, Angew. Chem. Int. Ed. 62 (2022), e202210958.

[69] C. Lv, L.X. Zhong, Y. Yao, D.B. Liu, Y. Kong, X.L. Jin, Z.W. Fang, W.J. Xu, C. S. Yan, K.N. Dinh, Boosting electrocatalytic ammonia production through mimicking "π back-donation", Chem 6 (2020) 2690–2702.

[70] P.P. Power, Main-group elements as transition metals, Nature 463 (2010) 171–177.

[71] Y. Sun, Y. Wang, H. Li, W. Zhang, X.M. Song, D.M. Feng, X. Sun, B.H. Jia, H. Mao, T.Y. Ma, Main group metal elements for ambient-condition electrochemical nitrogen reduction, J. Energy Chem. 62 (2021) 51–70.

[72] B.E. Conway, G. Jerkiewicz, Relation of energies and coverages of underpotential and overpotential deposited H at Pt and other metals to the 'volcano curve' for cathodic H₂ evolution kinetics, Electrochim. Acta 45 (2000) 4075–4083.

[73] E. Dražević, E. Skulason, Are there any overlooked catalysts for electrochemical NH₃ synthesis—new insights from analysis of thermochemical data, iScience 23 (2020), 101803.

[74] Y.Y. Yang, L.F. Zhang, Z.P. Hu, Y. Zheng, C. Tang, P. Chen, R.G. Wang, K.W. Qiu, J. Mao, T. Ling, S.Z. Q, The crucial role of charge accumulation and spin polarization in activating carbon-based catalysts for electrocatalytic nitrogen reduction, Angew. Chem. Int. Ed. 59 (2020) 4525–4531.

[75] M.A. Légaré, G. Bélanger Chabot, R.D. Dewhurst, E. Welz, I. Krummenacher, B. Engels, H. Braunschweig, Nitrogen fixation and reduction at boron, Science 359 (2018) 896–900.

[76] L.L. Zhang, L.X. Ding, G.F. Chen, X.F. Yang, H.H. Wang, Ammonia synthesis under ambient conditions: selective electroreduction of dinitrogen to ammonia on black phosphorus nanosheets, Angew. Chem. Int. Ed. 131 (2019) 2638–2642.

[77] Y.C. Hao, Y. Guo, L.W. Chen, M. Shu, X.Y. Wang, T.A. Bu, W.Y. Gao, N. Zhang, X. Su, X. Feng, Promoting nitrogen electroreduction to ammonia with bismuth nanocrystals and potassium cations in water, Nat. Catal. 2 (2019) 448–456.

[78] Y. Wang, M.M. Shi, D. Bao, F.L. Meng, Q. Zhang, Y.T. Zhou, K.H. Liu, Y. Zhang, J. Z. Wang, Z.W. Chen, Generating defect-rich bismuth for enhancing the rate of nitrogen electroreduction to ammonia, Angew. Chem. Int. Ed. 131 (2019) 9564–9569.

[79] P.H. van Langevelde, I. Katsounaros, M.T. Koper, Electrocatalytic nitrate reduction for sustainable ammonia production, Joule 5 (2021) 290–294.

[80] Z.W. Fang, Z.Y. Jin, S.S. Tang, P.P. Li, P. Wu, G.H. Yu, Porous two-dimensional iron-cyano nanosheets for high-rate electrochemical nitrate reduction, ACS Nano 16 (2021) 1072–1081.

[81] L.D. Xu, C. Wang, X.C. Zhang, D.C. Guo, Q.J. Pan, G. Zhang, S.H. Wang, NOₓ sensitivity of conductometric In(OH)₃ sensors operated at room temperature and transition from p-to n-type conduction, Sens. Actuators B Chem. 245 (2017) 533–540.

[82] C. Chen, S. Li, X. Zhu, S. Bo, K. Cheng, N. He, M. Qiu, C. Xie, D. Song, Y. Liu, W. Chen, Y. Li, C. Li, L. S, Wang, Balancing sub-reaction activity to boost electrocatalytic urea synthesis using a metal-free electrocatalyst, Carbon Energy 13 (2023), e345.

[83] H.Q. Yin, Z.S. Sun, Q.P. Zhao, L.L. Yang, T.B. Lu, Z.M. Zhang, Electrochemical urea synthesis by coreduction of CO₂ and nitrate with Feᴵᴵ-FeᴵᴵᴵOOH@BiVO₄ heterostructures, J. Energy Chem. 84 (2023) 385–393.

[84] Y.N. Mao, Y. Jiang, H. Liu, Y.M. Jiang, M. Li, W. Su, R.X. He, Ambient electrocatalytic synthesis of urea by co-reduction of NO_3^- and CO_2 over graphene-supported In_2O_3, Chin. Chem. Lett. 8 (2023) 108540.

[85] N. Li, H. Gao, Z.X. Liu, Q.J. Zhi, B.W. Li, L. Gong, B.T. Chen, T. Yang, K. Wang, P. Jin, J.Z. Jiang, Metalphthalocyanine frameworks grown on TiO_2 nanotubes for synergistically and efficiently electrocatalyzing urea production from CO_2 and nitrate, Sci. China Chem. 66 (2023) 1417–1424.

[86] Y.C. Wang, Y. Liu, W. Liu, J. Wu, Q. Li, Q.G. Feng, Z.Y. Chen, X. Xiong, D.S. Wang, Y.P. Lei, Regulating the coordination structure of metal single atoms for efficient electrocatalytic CO_2 reduction, Energy Environ. Sci. 13 (2020) 4609–4624.

[87] Y.X. Wang, H.Y. Su, Y.H. He, L.G. Li, S. Zhu, H. Shen, P.F. Xie, X.B. Fu, G.Y. Zhou, C. Feng, Advanced electrocatalysts with single-metal-atom active sites, Chem. Rev. 120 (2020) 12217–12314.

[88] J.Q. Feng, L.R. Zheng, C.Y. Jiang, Z.P. Chen, L. Liu, S. Zeng, L. Bai, S.J. Zhang, X. P. Zhang, Constructing single Cu-N_3 sites for CO_2 electrochemical reduction over a wide potential range, Green. Chem. 23 (2021) 5461–5466.

[89] C.C. Xu, X. Zhi, A. Vasileff, D. Wang, B. Jin, Y. Jiao, Y. Zheng, S.Z. Qiao, Highly selective two-electron electrocatalytic CO_2 reduction on single-atom Cu catalysts, Small Struct. 2 (2021) 2000058.

[90] L. Yan, X.D. Liang, Y. Sun, L.P. Xiao, B.A. Lu, G. Li, Y.Y. Li, Y.H. Hong, L.Y. Wan, C. Chen, Evolution of Cu single atom catalysts to nanoclusters during CO_2 reduction to CO, Chem. Commun. 58 (2022) 2488–2491.

[91] D.T. Chen, L.H. Zhang, J. Du, H.H. Wang, J.Y. Guo, J.Y. Zhan, F. Li, F.S. Yu, A tandem strategy for enhancing electrochemical CO_2 reduction activity of single-atom Cu-S_1N_3 catalysts via integration with Cu nanoclusters, Angew. Chem. Int. Ed. 133 (2021) 24224–24229.

[92] Z.C. Luo, Z.Y. Yin, J.Q. Yu, Y. Yan, B. Hu, R.F. Nie, A.F. Kolln, X. Wu, R.K. Behera, M. Chen, General synthetic strategy to ordered mesoporous carbon catalysts with single-atom metal sites for electrochemical CO_2 reduction, Small 18 (2022) 2107799.

[93] S.X. Jiang, H.T. Ni, P.Y. Li, J.L. Wang, H. Ren, Metal/N-doped carbon (metal=Ag, Cu, Ni) nanocatalysts for selective hydrogenation of 4-nitrophenol, Catal. Commun. 151 (2021), 106280.

[94] T.H. Zhu, Q.S. Chen, P. Liao, W.J. Duan, S. Liang, Z. Yan, C.H. Feng, Single-atom Cu catalysts for enhanced electrocatalytic nitrate reduction with significant alleviation of nitrite production, Small 16 (2020) 2004526.

[95] P. Ren, Q.L. Li, T. Song, Y. Yang, Facile fabrication of the Cu-NC catalyst with atomically dispersed unsaturated Cu-N_2 active sites for highly efficient and selective glaser-hay coupling, ACS Appl. Mater. Interfaces 12 (2020) 27210–27218.

[96] X. Zhao, G.Z. Hu, F. Tan, S.S. Zhang, X.Z. Wang, X. Hu, A.V. Kuklin, G. V. Baryshnikov, H. Ågren, X.H. Zhou, Copper confined in vesicle-like BCN cavities promotes electrochemical reduction of nitrate to ammonia in water, J. Mater. Chem. A 9 (2021) 23675–23686.

[97] P.M. Krzywda, A.P. Rodríguez, N.E. Benes, B.T. Mei, G. Mul, Carbon-nitrogen bond formation on Cu electrodes during CO_2 reduction in NO_3^- solution, Appl. Catal. B Environ. 316 (2022), 121512.

[98] Y. Zhou, E. Song, W. Chen, C.U. Segre, J.D. Zhou, Y.C. Lin, C. Zhu, R. Ma, P. Liu, S.F. Chu, Dual-metal interbonding as the chemical facilitator for single-atom dispersions, Adv. Mater. 32 (2020) 2003484.

[99] B.T. Qiao, A.Q. Wang, X.F. Yang, L.F. Allard, Z. Jiang, Y.T. Cui, J.Y. Liu, J. Li, T. Zhang, Single-atom catalysis of CO oxidation using Pt_1/FeO_x, Nat. Chem. 3 (2011) 634–641.

[100] J. Pérez Ramírez, N. López, Strategies to break linear scaling relationships, Nat. Catal. 2 (2019) 971–976.

[101] J.H. Fu, J.H. Dong, R. Si, K.J. Sun, J.Y. Zhang, M.R. Li, N.N. Yu, B.S. Zhang, M. G. Humphrey, Q. Fu, J.H. Huang, Synergistic effects for enhanced catalysis in a dual single-atom catalyst, ACS Catal. 11 (2021) 1952–1961.

[102] D.D. Xu, Q. Shi, X.Z. Song, H. Wang, Z.Y. Bian, Improving oxygen reduction reaction and selective hydrodechlorination performance based on CoNi on graphene using ionic liquids as a binder, J. Electrochem. Soc. 166 (2019) H157–H166.

[103] N. Ma, J. Xu, Z.Y. Bian, Y.J. Yang, L. Zhang, H. Wang, $BiVO_4$ plate with Fe and Ni oxyhydroxide cocatalysts for the photodegradation of sulfadimethoxine antibiotics under visible-light irradiation, Chem. Eng. J. 389 (2020), 123426.

[104] M. Zhang, L. Zhang, H. Wang, Z.Y. Bian, Hybrid electrocatalytic ozonation treatment of high-salinity organic wastewater using Ni-Ce/OMC particle electrodes, Sci. Total Environ. 724 (2020), 138170.

[105] Y.J. Yang, N. Ma, H. Wang, Q. Liang, Z.Y. Bian, Pd-Ag/graphene electrochemical sensor for chlorophenol contaminant determination, J. Electrochem. Soc. 166 (2019) B266–B275.

[106] Y.J. Guo, X.Y. Zhang, D.D. Zhang, S.L. Li, H. Wang, Y.Y. Peng, Z.Y. Bian, Catalysts containing Fe and Mn from dewatered sludge showing enhanced electrocatalytic degradation of triclosan, Environ. Res. 214 (2022), 114065.

[107] G.B. Wen, D.U. Lee, B.H. Ren, F.M. Hassan, G. Jiang, Z.P. Cano, J. Gostick, E. Croiset, Z.Y. Bai, L. Yang, Orbital interactions in Bi-Sn bimetallic electrocatalysts for highly selective electrochemical CO_2 reduction toward formate production, Adv. Energy Mater. 8 (2018) 1802427.

[108] V.G. Rao, U. Aslam, S. Linic, Chemical requirement for extracting energetic charge carriers from plasmonic metal nanoparticles to perform electron-transfer reactions, J. Am. Chem. Soc. 141 (2018) 643–647.

[109] B.H. Ren, G.B. Wen, R. Gao, D. Luo, Z. Zhang, W.B. Qiu, Q.Y. Ma, X. Wang, Y. Cui, L. Ricardez-sandoval, Nano-crumples induced Sn-Bi bimetallic interface pattern with moderate electron bank for highly efficient CO_2 electroreduction, Nat. Commun. 13 (2022) 1–11.

[110] B.H. Ren, X.Q. Dong, Y.Z. Yu, G.B. Wen, M.H. Zhang, A density functional theory study on the carbon chain growth of ethanol formation on Cu-Co (111) and (211) surfaces, Appl. Surf. Sci. 412 (2017) 374–384.

[111] F.M. Hassan, R. Batmaz, J.D. Li, X.L. Wang, X.C. Xiao, A.P. Yu, Z.W. Chen, Evidence of covalent synergy in silicon-sulfur-graphene yielding highly efficient and long-life lithium-ion batteries, Nat. Commun. 6 (2015) 1–11.

[112] D.D. Zhang, Y.Y. Peng, L. Zhang, Y.J. Guo, L. Liu, H. Wang, Z.Y. Bian, Synergistic effect of atomically dispersed Fe-Ni pair sites for electrocatalytic reactions to remove chlorinated organic compounds, Chemosphere 303 (2022) 134992.

[113] X.Y. Shen, X.K. Liu, S.C. Wang, T. Chen, W. Zhang, L.L. Cao, T. Ding, Y. Lin, D. Liu, L. Wang, Synergistic modulation at atomically dispersed Fe/Au interface for selective CO_2 electroreduction, Nano Lett. 21 (2020) 686–692.

[114] K. Hadjiivanov, E. Ivanova, M. Daturi, J. Saussey, J.C. Lavalley, Nitrosyl complexes on Co–ZSM-5: an FTIR spectroscopic study, Chem. Phys. Lett. 370 (2003) 712–718.

[115] J. Sárkány, Effects of water and ion-exchanged counterion on the FT-IR spectra of ZSM-5: Part III. $Cu^+(CO)_2$-ZSM-5: interaction of $Cu^+(CO)_2$ complex with H_2O and changes in skeletal T-O-T vibrations, Appl. Catal. A Gen. 229 (2002) 291–312.

[116] S.K. Geng, Y. Zheng, S.Q. Li, H. Su, X. Zhao, J. Hu, H.B. Shu, M. Jaroniec, P. Chen, Q.H. Liu, Nickel ferrocyanide as a high-performance urea oxidation electrocatalyst, Nat. Energy 6 (2021) 904–912.

[117] C.C. Liu, H.L. Tong, P.F. Wang, R. Huang, P.L. Huang, G. Zhou, L.Z. Liu, The asymmetric orbital hybridization in single-atom-dimers for urea synthesis by optimizing the C-N coupling reaction pathway, Appl. Catal. B Environ. 336 (2023), 122917.

[118] L. Cheng, X.Y. Yue, L.X. Wang, D.N. Zhang, P. Zhang, J.J. Fan, Q.J. Xiang, Dual-single-atom tailoring with bifunctional integration for high-performance CO_2 photoreduction, Adv. Mater. 33 (2021) 2105135.

[119] S.B. Zhang, J. Geng, Z. Zhao, M. Jin, W.Y. Li, Y.X. Ye, K. Li, G.Z. Wang, Y. X. Zhang, H.J. Yin, H.M. Zhang, H.J. Zhao, High-efficiency electrosynthesis of urea over bacterial cellulose regulated Pd-Cu bimetallic catalyst, EES Catal. 1 (2023) 45–53.

[120] A.A.B. Padama, A.P.S. Cristobal, J.D. Ocon, W.A. Diño, H. Kasai, Effects of adsorbates (CO, COH, and HCO) on the arrangement of Pd atoms in PdCu(111), J. Phys. Chem. C. 121 (2017) 17818–17826.

[121] J.Z. Qin, N.S. Liu, L.Z. Chen, K. Wu, Q.L. Zhao, B.J. Liu, Z.F. Ye, Selective electrochemical urea synthesis from nitrate and CO_2 using in situ Ru anchoring onto a three-dimensional copper electrode, ACS Sustain. Chem. Eng. 10 (2022) 15869–15875.

[122] S. Fu, K. Chu, M. Guo, Z. Wu, Y. Wang, J. Yang, F. Lai, T. Liu, Ultrasonic-assisted hydrothermal synthesis of RhCu alloy nanospheres for electrocatalytic urea production, Chem. Commun. 59 (2023) 4344–4347.

[123] M.Y. Qiu, X.R. Zhu, S.W. Bo, K. Cheng, N.H. He, K.Z. Gu, D.Z. Song, C. Chen, X. X. Wei, D.D. Wang, Y.Y. Liu, S. Li, X.J. Tu, Y.F. Li, Q.H. Liu, C.G. Li, S.Y. Wang, Boosting electrocatalytic urea production via promoting asymmetric C-N coupling, CCS Chem. (2023) 1–11.

[124] S. Shin, S. Sultan, Z.X. Chen, H. Lee, H. Choi, T.U. Wi, C. Park, T. Kim, C. Lee, J. Jeong, H. Shin, T.H. Kim, H. Ju, H.C. Yoon, H.K. Song, H.W. Lee, J. Bang, Y. Kwon, Copper with an atomic-scale spacing for efficient electrocatalytic co-reduction of carbon dioxide and nitrate to urea, Energy Environ. Sci. 16 (2023) 2003–2013.

[125] X. Zhu, Q. Imtiaz, F. Donat, C.R. Müller, F. Li, Chemical looping beyond combustion-a perspective, Energy Environ. Sci. 13 (2020) 772–804.

[126] D.F. Yan, H. Li, C. Chen, Y.Q. Zou, S.Y. Wang, Defect engineering strategies for nitrogen reduction reactions under ambient conditions, Small Methods 3 (2019) 1800331.

[127] C. Xie, D.F. Yan, W. Chen, Y.Q. Zou, R. Chen, S.Q. Zang, Y.Y. Wang, X.D. Yao, S. Q. Wang, Insight into the design of defect electrocatalysts: from electronic structure to adsorption energy, Mater. Today 31 (2019) 47–68.

[128] C. Xie, D.F. Yan, H. Li, S.Q. Du, W. Chen, Y.Y. Wang, Y. Zou, R. Chen, S.Y. Wang, Defect chemistry in heterogeneous catalysis: recognition, understanding, and utilization, ACS Catal. 10 (2020) 11082–11098.

[129] C. Tang, H.F. Wang, X. Chen, B.Q. Li, T.Z. Hou, B. Zhang, Q. Zhang, M.M. Titirici, F. Wei, Topological defects in metal-free nanocarbon for oxygen electrocatalysis, Adv. Mater. 28 (2016) 6845–6851.

[130] S. Liu, H.B. Yang, S.F. Hung, J. Ding, W. Cai, L. Liu, J. Gao, X. Li, X. Ren, Z. Kuang, Elucidating the electrocatalytic CO_2 reduction reaction over a model single-atom nickel catalyst, Angew. Chem. Int. Ed. 59 (2020) 798–803.

[131] F. Hu, S.C. Abeyweera, J. Yu, D.T. Zhang, Y. Wang, Q.M. Yan, Y.G. Sun, Quantifying electrocatalytic reduction of CO_2 on twin boundaries, Chem 6 (2020) 3007–3021.

[132] Y.F. Wang, Z. Chen, P. Han, Y.H. Du, Z.X. Gu, X. Xu, G.F. Zheng, Single-atomic Cu with multiple oxygen vacancies on ceria for electrocatalytic CO_2 reduction to CH_4, ACS Catal. 8 (2018) 7113–7119.

[133] N. Cao, Y.L. Quan, A.X. Guan, C. Yang, Y. Ji, L.J. Zhang, G.F. Zheng, Oxygen vacancies enhanced cooperative electrocatalytic reduction of carbon dioxide and nitrite ions to urea, J. Colloid Interface Sci. 577 (2020) 109–114.

[134] C. Wei, S. Sun, D. Mandler, X. Wang, S.Z. Qiao, Z.J. Xu, Approaches for measuring the surface areas of metal oxide electrocatalysts for determining their intrinsic electrocatalytic activity, Chem. Soc. Rev. 48 (2019) 2518–2534.

[135] J.B. Zhang, R.G. Yin, Q. Shao, T. Zhu, X.Q. Huang, Oxygen vacancies in amorphous InO_x nanoribbons enhance CO_2 adsorption and activation for CO_2 electroreduction, Angew. Chem. Int. Ed. 58 (2019) 5609–5613.

[136] Z.Y. Li, P. Zhou, M. Zhou, H. Jiang, H. Li, S.Q. Liu, H. Zhang, S. Yang, Z.H. Zhang, Synergistic electrocatalysis of crystal facet and O-vacancy for enhancive urea synthesis from nitrate and CO_2, Appl. Catal. B Environ. 338 (2023), 122962.

[137] A. Devadas, S. Vasudevan, F. Epron, Nitrate reduction in water: INFLuence of the addition of a second metal on the performances of the Pd/CeO$_2$ catalyst, J. Hazard. Mater. 185 (2011) 1412–1417.

[138] F. Epron, F. Gauthard, J. Barbier, Catalytic reduction of nitrate in water on a monometallic Pd/CeO$_2$ catalyst, J. Catal. 206 (2002) 363–367.

[139] M.S. Kim, D.W. Lee, S.H. Chung, J.T. Kim, I.H. Cho, K.Y. Lee, Pd-Cu bimetallic catalysts supported on TiO$_2$-CeO$_2$ mixed oxides for aqueous nitrate reduction by hydrogen, J. Mol. Catal. A Chem. 392 (2014) 308–314.

[140] Z.S. Ni, H.B. Bi, C.L. Jiang, H. Sun, W.L. Zhou, J.J. Tian, Q.Z. Lin, Investigation of co-combustion of sewage sludge and coffee industry residue by TG-FTIR and machine learning methods, Fuel 309 (2022), 122082.

[141] B. Ball, P. Das, P. Sarkar, Molybdenum atom-mediated salphen-based covalent organic framework as a promising electrocatalyst for the nitrogen reduction reaction: A first-principles study, J. Phys. Chem. C. 125 (2021) 26061–26072.

[142] P. Roy, A. Pramanik, P. Sarkar, Graphitic carbon nitride sheet supported single-atom metal-free photocatalyst for oxygen reduction reaction: A first-principles analysis, J. Phys. Chem. Lett. 12 (2021) 2788–2795.

[143] P. Roy, A. Pramanik, P. Sarkar, Dual-silicon-doped graphitic carbon nitride sheet: an efficient metal-free electrocatalyst for urea synthesis, J. Phys. Chem. Lett. 12 (2021) 10837–10844.

[144] C. Chen, N.H. He, S.Y. Wang, Electrocatalytic C-N coupling for urea synthesis, Small Sci. 1 (2021) 2100070.

[145] X.X. Wei, Y.Y. Liu, X.R. Zhu, S.W. Bo, L. Xiao, C. Chen, T.T.T. Nga, Y.Q. He, M. Y. Qiu, C. Xie, D.D. Wang, Q.H. Liu, F. Dong, C.L. Dong, X.Z. Fu, S.Y. Wang, Dynamic reconstitution between copper single atoms and clusters for electrocatalytic urea synthesis, Adv. Mater. 35 (2023), e2300020.

[146] C.F. Du, L. Yang, K.W. Tang, W. Fang, X.Y. Zhao, Q.H. Liang, X.H. Liu, H. Yu, W. H. Qi, Q.Y. Yan, Ni nanoparticles/V$_4$C$_3$T$_x$ MXene heterostructures for electrocatalytic nitrogen fixation, Mater. Chem. Front. 5 (2021) 2338–2346.

[147] Y. Kong, H.B. Kong, C. Lv, G. Chen, Engineering reductive iron on a layered double hydroxide electrocatalyst for facilitating nitrogen reduction reaction, Adv. Mater. Interfaces 9 (2022) 2102242.

[148] H.Y. Tang, Z.Y. Bian, L. Zhang, H. Wang, Reuse solution of hardness industrial circulating cooling water: Targeted ion-selective electro-adsorption by functionalized electrode, Chemosphere 280 (2021), 130748.

[149] A. Mohammadpour, E. Gharehchahi, A. Badeenezhad, I. Parseh, R. Khaksefidi, M. Golaki, R. Dehbandi, A. Azhdarpoor, Z. Derakhshan, J. Rodriguez Chueca, Nitrate in groundwater resources of hormozgan province, Southern Iran: concentration fstimation, distribution and probabilistic health risk assessment using monte carlo simulation, Water 14 (2022) 564.

[150] X.Z. Song, D. Huang, L. Zhang, H. Wang, L.Y. Wang, Z.Y. Bian, Electrochemical degradation of the antibiotic chloramphenicol via the combined reduction-oxidation process with Cu-Ni/graphene cathode, Electrochim. Acta 330 (2020), 135187.

[151] L.K. Munishi, W. Blake, S. Comber, T.H. Hutchinson, P.A. Ndakidemi, Towards sustainability: Threat of water quality degradation and eutrophication in usangu agro-ecosystem tanzania, Mar. Pollut. Bull. 181 (2022), 113909.

[152] K. Upreti, V.H. Rivera Monroy, K.C. Maiti, A.E. Giblin, E. Castañeda Moya, Dissimilatory nitrate reduction to ammonium (DNRA) is marginal relative to denitrification in emerging-eroding wetlands in a subtropical oligohaline and eutrophic coastal delta, Sci. Total Environ. 819 (2022), 152942.

[153] Z.J. Liu, X.B. Sun, J. Fu, W. Liu, Z.Q. Cai, Elevated nitrate promoted photodegradation of PAHs in aqueous phase: Implications for the increased nutrient discharge, J. Hazard. Mater. 443 (2023), 130143.

[154] T.T. Huang, L. Deng, T. Wang, X.Y. Liao, J. Hu, C.Q. Tan, R.P. Singh, Effects of bromide ion on the formation and toxicity alteration of halonitromethanes from nitrate containing humic acid water during UV/chlor (am) ine disinfection, Water Res 225 (2022) 119175.

[155] E.Q. Liu, C.Z. Fan, M. Zhao, S.F. Jiang, Z.Q. Wang, Z. Jin, K. Bei, X.Y. Zheng, S. Q. Wu, Q.Y. Zeng, Effects of heavy metals on denitrification processes in water treatment: a review, Sep. Purif. Technol. (2022), 121793.

[156] Z.L. Hao, A. Ali, Y. Ren, J.F. Su, Z. Wang, A mechanistic review on aerobic denitrification for nitrogen removal in water treatment, Sci. Total Environ. (2022), 157452.

[157] K. Zimmermann, J. Wright, P. Bérubé, B. Barbeau, M. Mohseni, Biological ion exchange capable of sulphate-based secondary ion exchange during long-term DOC removal, Water Res 196 (2021), 117036.

[158] S. He, P.Y. Li, F.M. Su, D. Wang, X.F. Ren, Identification and apportionment of shallow groundwater nitrate pollution in Weining Plain, northwest China, using hydrochemical indices, nitrate stable isotopes, and the new Bayesian stable isotope mixing model (MixSIAR), Environ. Pollut. 298 (2022), 118852.

[159] H.T. Du, H.R. Guo, K.K. Wang, X.N. Du, B.A. Beshiwork, S.J. Sun, Y.S. Luo, Q. Liu, T.S. Li, X.P. Sun, Durable electrocatalytic reduction of nitrate to ammonia over defective pseudobrookite Fe$_2$TiO$_5$ nanofibers with abundant oxygen vacancies, Angew. Chem. Int. Ed. (2022) e202215782.

[160] L. Su, D.D. Han, G.J. Zhu, H. Xu, W. Luo, L.J. Wang, W. Jiang, A.G. Dong, J. P. Yang, Tailoring the assembly of iron nanoparticles in carbon microspheres toward high-performance electrocatalytic denitrification, Nano Lett. 19 (2019) 5423–5430.

[161] Z.X. Wang, D. Richards, N. Singh, Recent discoveries in the reaction mechanism of heterogeneous electrocatalytic nitrate reduction, Catal. Sci. Technol. 11 (2021) 705–725.

[162] (a) J.X. Liu, D. Richards, N. Singh, B. Goldsmith, ACS Catal. 9 (2019) 7052–7064;
(b) L. Wei, D.J. Liu, B.A. Rosales, J.W. Evans, J. Vela, ACS Catal. 10 (2020) 3618–3628.

[163] J. Li, G.M. Zhan, J.H. Yang, F.J. Quan, C.L. Mao, Y. Liu, B. Wang, F.C. Lei, L.J. Li, A.W. Chan, Efficient ammonia electrosynthesis from nitrate on strained ruthenium nanoclusters, J. Am. Chem. Soc. 142 (2020) 7036–7046.

[164] Y. Fu, K.K. Li, M. Batmunkh, H. Yu, S. Donne, B.H. Jia, T.Y. Ma, Unsaturated p-metal-based metal-organic frameworks for selective nitrogen reduction under ambient conditions, ACS Appl. Mater. Interfaces 12 (2020) 44830–44839.

[165] Q. Liu, X. Zhang, J.H. Wang, Y.L. Zhang, S. Bian, Z.Q. Cheng, N. Kang, H. Huang, S. Gu, Y. Wang, D.N. Liu, Paul K. Chu, X.F. Yu, Crystalline red phosphorus nanoribbons: large-scale synthesis and electrochemical nitrogen fixation, Angew. Chem. Int. Ed. 132 (2020) 14489–14493.

[166] X.X. Zhang, T.W. Wu, H.B. Wang, R.B. Zhao, H.Y. Chen, T. Wang, P.P. Wei, Y. L. Luo, Y.N. Zhang, X.P. Sun, Boron nanosheet: an elemental two-dimensional (2D) material for ambient electrocatalytic N$_2$-to-NH$_3$ fixation in neutral media, ACS Catal. 9 (2019) 4609–4615.

[167] H. Wang, Z.Y. Bian, X. Liu, Conversion of CO$_2$ to fuels using carbon-based cathodes in aqueous electrochemical reduction system, Rev. Adv. Sci. Eng. 3 (2014) 121–132.

[168] Y.J. Yan, Y.Y. Peng, Y.C. Song, R.Y. Wang, H. Wang, Z.Y. Bian, Polyethyleneimine-reinforced Sn/Cu foam dendritic self-supporting catalytic cathode for CO$_2$ reduction to HCOOH, Chemosphere 301 (2022), 134704.

[169] G. Lu, H. Wang, Z.Y. Bian, X. Liu, Electrochemical reduction of CO$_2$ to organic acids by a Pd-MWNTs gas-diffusion electrode in aqueous medium, Sci. World J. 424617 (2013) 1–8.

[170] G. Lu, H. Wang, Z.Y. Bian, X. Liu, Electrocatalytic reduction of CO$_2$ to formic acid on palladium–graphene nanocomposites gas-diffusion electrode, J. Nanosci. Nanotechnol. 14 (2014) 7097–7103.

[171] Y.F. Ling, Q.L. Ma, Y.F. Yu, B. Zhang, Optimization strategies for selective CO$_2$ electroreduction to fuels, Trans. Tianjin Univ. 27 (2021) 180–200.

[172] F. Wang, N. Ma, L. Zheng, L. Zhang, Z.Y. Bian, H. Wang, Interface engineering of pp Z-scheme BiOBr/Bi$_{12}$O$_{17}$Br$_2$ for sulfamethoxazole photocatalytic degradation, Chemosphere 307 (2022), 135666.

[173] X.J. Liu, X.L. Xu, F.X. Li, J.Y. Xu, H.M. Ma, X. Sun, D. Wu, C.W. Zhang, X. Ren, Q. Wei, Heterostructured Bi$_2$S$_3$/MoS$_2$ nanoarrays for efficient electrocatalytic nitrate reduction to ammonia under ambient conditions, ACS Appl. Mater. Interfaces 14 (2022) 38835–38843.

[174] L. Zhang, W. Wang, H. Wang, X. Ma, Z.Y. Bian, Molecular manganese catalyst anchored on Bi$_2$MoO$_6$ with enhanced photogenerated charges separation for efficient visible-light photoreduction of CO$_2$, J. Mater. Sci. Mater. Electron. 30 (2019) 5808–5819.

[175] W.X. Chen, H.L. Xing, S.T. Gao, P. Yang, X.L. Ji, Bi-semiconductor heterojunction Cu$_9$S$_5$@VO$_2$ microspheres with morphology regulation as broadband high-performance electromagnetic wave absorber, Appl. Surf. Sci. 610 (2023), 155539.

[176] Q. Shi, X.Z. Song, Z.Y. Bian, Enriched photoelectrochemical performance of phosphate doped BiVO$_4$ photoelectrode by coupling FeOOH and rGO, J. Electrochem. Soc. 165 (2017) H3018–H3027.

[177] T. Chouki, M. Machreki, I.A. Rutkowska, B. Rytelewska, P.J. Kulesza, G. Tyuliev, M. Harb, L.M. Azofra, S. Emin, Highly active iron phosphide catalysts for selective electrochemical nitrate reduction to ammonia, J. Environ. Chem. Eng. 11 (2023), 109275.

[178] N. Sathishkumar, H.T. Chen, Mechanistic understanding of the electrocatalytic nitrate reduction activity of double-atom catalysts, J. Phys. Chem. C 127 (2023) 994–1005.

[179] A.Y. Abir, S.N. Uddin, M. Hasan, M.A. Aziz, S. Shah, J. Ahmed, M.A. Hasnat, Cu-electrodeposited gold electrode for the sensitive electrokinetic investigations of nitrate reduction and detection of the nitrate ion in acidic medium, Results Chem. 5 (2023), 100702.